

Stress and Fracture Mechanics Analyses of Boiling Water Reactor and Pressurized Water Reactor Pressure Vessel Nozzles – Revision 1

Prepared by

Shengjun (Sean) Yin and B. Richard Bass

Oak Ridge National Laboratory

Gary L. Stevens

U.S. Nuclear Regulatory Commission

Prepared for

U.S. Nuclear Regulatory Commission

Prepared by

OAK RIDGE NATIONAL LABORATORY

Oak Ridge, Tennessee 37831-6285

managed by

UT-BATTELLE, LLC

for the

U.S. DEPARTMENT OF ENERGY

under contract DE-AC05-00OR22725

This report was prepared as an account of work sponsored by an agency of the United States government. Neither the United States government nor any agency thereof, nor any of their employees, makes any warranty, express or implied, or assumes any legal liability or responsibility for the accuracy, completeness, or usefulness of any information, apparatus, product, or process disclosed, or represents that its use would not infringe privately owned rights. Reference herein to any specific commercial product, process, or service by trade name, trademark, manufacturer, or otherwise, does not necessarily constitute or imply its endorsement, recommendation, or favoring by the United States government or any agency thereof. The views and opinions of authors expressed herein do not necessarily state or reflect those of the United States government or any agency thereof.

Stress and Fracture Mechanics Analyses of Boiling Water Reactor and Pressurized Water Reactor Pressure Vessel Nozzles – Revision 1

Manuscript Completed: December 2010

Manuscript Revised: June 2012

Date Published: June 2012

Prepared by

Shengjun (Sean) Yin and B. Richard Bass

Oak Ridge National Laboratory
Managed by UT-Battelle, LLC
Oak Ridge National Laboratory
Oak Ridge, TN 37831-6085

Gary L. Stevens

NRC/RES/DE/CIB

Prepared for
Division of Engineering
Office of Nuclear Regulatory Research
U.S. Nuclear Regulatory Commission
Washington, DC 20555-0001
NRC Job Code N6438

Revision Control Log

Revision	Date	Affected Sections	Description
0	12/09/2010	All	Initial issue.
1	06/22/2012	All	Additions made to incorporate results of internal review and additional analyses: editorial corrections and enhancements made throughout; added Sections 3.6.2 and 3.6.3; added associated text to Abstract and Sections 1.0 and 8.0.

Stress and Fracture Mechanics Analyses of Boiling Water Reactor and Pressurized Water Reactor Pressure Vessel Nozzles – Revision 1

S. Yin, B. R. Bass and G. L. Stevens

ABSTRACT

This work was performed to support an investigation of Title 10 to the U.S. Code of Federal Regulations (CFR), Part 50, Appendix G, “Fracture Toughness Requirements.” This report describes stress analyses and fracture mechanics work performed to assess boiling water reactor (BWR) and pressurized water reactor (PWR) nozzles located in the reactor pressure vessel (RPV) adjacent to the active core. The primary motivation for this work was to gain a more thorough understanding of nozzle stress and fracture mechanics solutions so that they can be integrated into pressure-temperature (P-T) limit evaluations, especially for those nozzle configurations adjacent to the active core where radiation effects are significant. Various RPV nozzle geometries were evaluated:

1. BWR recirculation outlet nozzle;
2. BWR core spray nozzle;
3. PWR inlet nozzle;
4. PWR outlet nozzle; and
5. BWR drill-hole style instrument nozzle.

These nozzle configurations were selected because they lie close enough to the active core region such that they may receive sufficient fluence prior to end-of-license (EOL), in which case they may become limiting with respect to P-T limits developed in accordance with 10 CFR 50 Appendix G as part of the RPV material surveillance program. The selection includes five nozzle configurations in the U.S. light water reactor (LWR) fleet that are close to the active core region and will therefore experience the most significant fluence effects of most RPV nozzles.

The purpose of these analyses was as follows:

- To model and understand differences in the pressure and thermal stress results using a two-dimensional (2-D) axisymmetric finite element model (FEM) vs. a three-dimensional (3-D) FEM for all nozzle configurations. In particular, the ovalization (stress concentration) effect of two intersecting cylinders, which is typical of RPV nozzle configurations, was investigated;
- To verify the accuracy of linear elastic fracture mechanics (LEFM) closed-form solutions for stress intensity factor for a postulated nozzle corner circular crack for both thermal and pressure loading for all nozzle configurations;
- To assess the significance of attached piping loads on the stresses in the nozzle corner region;
- To assess the significance of applying pressure on the crack face with respect to the stress intensity factor for a postulated nozzle corner crack;
- To verify a scaling approximation used for the 3-D FEM K_I solutions for a $1/4t$ circular corner crack to estimate the stress intensity factors for a shallower $0.1t$ corner crack;
- To compare the 3-D FEM stress intensity factor solutions for a circular nozzle corner crack and a semi-elliptical nozzle corner crack and evaluate the flaw geometry effects on K_I along the crack front.

The results of this work support the following two conclusions:

- The simplified closed-form LEM solutions presented in Chapter 2 of this report for postulated circular nozzle corner cracks may be considered as part of future revisions of Paragraph G-2223, Nonmandatory Appendix G of ASME Code Section XI along with the use of a $1/4t$ postulated flaw size for establishing RPV P-T limits.
- A bounding stress concentration factor (SCF) value of 3.1, which agrees well with the stress index for hoop stress of 3.1 in Section III, Table NB-3338.2(c)-1 of the ASME Code, is appropriate for use in lieu of 3-D finite element analysis to account for corner effects on pressure stress for all nozzles with traditional forgings with rounded inside corners, such as the BWR recirculation outlet nozzle, the BWR core spray nozzle, and the PWR inlet nozzle. A bounding SCF value of 3.5 is more appropriate for use for nozzles with special discontinuities or sharp inside corners, such as the PWR outlet nozzle and the BWR instrument nozzle.

CONTENTS

	Page
Abstract.....	2
CONTENTS.....	4
LIST OF TABLES	5
LIST OF FIGURES	6
1. Introduction	9
2. Magnification Factor Method for Calculating Stress Intensity Factor for Postulated Corner Cracks in Nozzles.....	11
3. BWR Recirculation Outlet Nozzle	13
3.1 Uncracked BWR RO Nozzle 2-D Models	13
3.2 Uncracked BWR RO Nozzle 3-D Model.....	15
3.3 Assessment of Pressure Stresses	15
3.4 Assessment of Attached Piping Loads	15
3.5 Assessment of Thermal Stresses	16
3.6 BWR RO Nozzle 3-D Model with a Postulated Circular Corner Crack	17
3.6.1 Internal Pressure Loading for Cracked 3-D Model	18
3.6.2 Evaluation of a 0.1t Circular Flaw to Verify the Scaling Approximation	19
3.6.3 Evaluation of a 0.1t Semi-Elliptical Nozzle Corner Flaw.....	20
3.6.4 Cooldown Thermal Loading for Cracked 3-D Model.....	21
3.7 Assessment of Crack Face Pressure Effects	22
4. BWR Core Spray Nozzle	23
4.1 Uncracked BWR CS Nozzle Model.....	23
4.2 BWR CS Nozzle Model with a 3-D Simulated Circular Corner Crack	24
4.2.1 Internal Pressure Loading for Cracked 3-D Model	24
4.2.2 Thermal Shock Loading for Cracked 3-D Model.....	24
5. PWR Inlet Nozzle	27
5.1 Uncracked PWR Inlet Nozzle Model	27
5.2 PWR Inlet Nozzle Model with a 3-D Simulated Circular Corner Crack	27
6. PWR Outlet Nozzle	29
6.1 Uncracked PWR Outlet Nozzle Model	29
6.2 PWR Outlet Nozzle Model with a 3-D Simulated Circular Corner Crack.....	29
7. BWR Drill-Hole Style Instrument Nozzle	31
7.1 Uncracked BWR Instrument Nozzle Model.....	31
7.2 BWR Instrument Nozzle Model with a 3-D Simulated Circular Corner Crack.....	32
8. Summary and Conclusions.....	33
9. References	109

LIST OF TABLES

Table	Page
Table 1. Piping Loads Applied to the RO Nozzle.....	16

LIST OF FIGURES

Figure	Page
Figure 1. Stress Intensity Magnification Factors Method.....	36
Figure 2. Postulated Circular Nozzle Corner Crack for a Nozzle with a Rounded Corner..	37
Figure 3. Postulated Circular Nozzle Corner Crack for a Nozzle with Sharp 90° Corner..	38
Figure 4. BWR RO Nozzle and Safe End Geometry (from Figure 3 of Reference [6])	39
Figure 5. BWR RO Nozzle and Safe End Geometry (from Reference 5 of Reference [6]) ..	40
Figure 6. BWR RO Nozzle Geometry Used in the RO Nozzle FEM	41
Figure 7. 2-D and 3-D FEMs for the BWR RO Nozzle.....	42
Figure 8. Boundary and Loading Conditions for the 2-D BWR RO Nozzle FEMs	43
Figure 9. Results for BWR RO Nozzle 2-D (RPV Radius = 2R) FEM (Maximum SINT for P = 1,000 psig pressure loading = 32,880 psi).....	44
Figure 10. Results for BWR RO Nozzle 2-D (RPV Radius = R) FEM (Maximum SINT for P = 1,000 psig pressure loading = 16,130 psi).....	45
Figure 11. Portions Included in 3-D BWR RO Nozzle FEM.....	46
Figure 12. Boundary and Loading Conditions Applied in 3-D BWR RO Nozzle FEM	47
Figure 13. Results for BWR RO Nozzle 3-D FEM Maximum SINT for P = 1,000 psig pressure loading = 49,570 psi)	48
Figure 14. Piping Interface Loads Applied to the BWR RO Nozzle 3-D FEM	49
Figure 15. Maximum Principal Stress in BWR RO Nozzle Due to Pressure Load Only (left) and Pressure Plus Attached Piping Loads (right)	50
Figure 16. Comparison of Hoop Stress in BWR RO Nozzle Due to Pressure Load only and Pressure Plus Piping Loads.....	51
Figure 17. Maximum Principal Stress for the BWR RO Nozzle 3-D FEM Subjected to a Cool-down Transient.....	52
Figure 18. Maximum Principal Stress for the BWR RO Nozzle 2-D FEM Subjected to a Cool-down Transient.....	53
Figure 19. Maximum Principal Stress for the BWR RO Nozzle During a Cool-down Thermal Transient (at the ¼ t location along a 45° path through the nozzle corner)	54
Figure 20. Maximum Principal Stress for the BWR RO Nozzle Around the Nozzle Circumference for a Cool-down Transient (t = 119.5 minutes)	55
Figure 21. 1/4t Corner Crack Location and Configuration for the BWR RO Nozzle	56
Figure 22. 3-D FEM for the BWR RO Nozzle with a Postulated ¼t Circular Corner Crack	57
Figure 23. 45° Path Selected Through the BWR RO Nozzle Corner at the Azimuth of Maximum Pressure Stress	58
Figure 24. Hoop Stress as a Function of Distance Along the Nozzle Corner Path for the BWR RO Nozzle	59
Figure 25. K_I as a Function of Internal Pressure Loading Using Different Stress Profiles for the BWR RO Nozzle.....	60
Figure 26. Stress Intensity Factors (K_I) Along the Crack Front Under Applied Pressure Loading for the BWR RO Nozzle	61
Figure 27. Finite-element Model for BWR Recirculation Outlet Nozzle with Postulated 0.1t Circular Surface Corner Crack.....	62
Figure 28. Stress Intensity Factors (K_I) Along the Crack Front Under Applied Pressure Loading for the BWR RO Nozzle with Postulated 1/4t and 0.1t Flaws.	63
Figure 29. Finite-element Model for BWR Recirculation Outlet Nozzle with Postulated 0.1t Semi- Elliptical Surface Corner Crack (Aspect Ratio of 6).	64

Figure 30. Comparison of Stress Intensity Factors Along the Crack Front for a Postulated 0.1t Semi-Elliptical Corner Flaw and a Postulated 1/4t Circular Corner Flaw in BWR RO Nozzle Subjected to Pressure Loading.....	65
Figure 31. Hoop Stress as a Function of BWR RO Nozzle Corner Thickness at the Blend Radius under Thermal Loading	66
Figure 32. Stress Intensity Factor (K_I) Along the Crack Front Under Thermal Loading for the BWR RO Nozzle.....	67
Figure 33. Geometry for the BWR CS Nozzle (from Reference [12])	68
Figure 34. 3-D FEM for the Uncracked BWR CS Nozzle	69
Figure 35. Stress Intensity (SINT) for the BWR CS Nozzle Subjected to 1,000 psi Internal Pressure	70
Figure 36. Hoop Stress Extraction Path Selected for the BWR CS Nozzle	71
Figure 37. Hoop Stress Along the Selected Stress Path for the BWR CS Nozzle Under 1,000 psi Internal Pressure.....	72
Figure 38. 3-D FEM for the BWR CS Nozzle with a Postulated 1/4t Circular Corner Crack.....	73
Figure 39. Stress Intensity Factor (K_I) Along the Crack Front for 1,000 psig Pressure Loading for the BWR CS Nozzle	74
Figure 40. BWR Thermal Shock Transient Applicable to BWR Feedwater Nozzles.....	75
Figure 41. BWR Thermal Shock Transient Applied to Three Regions of the Uncracked 3-D BWR CS Nozzle FEM	76
Figure 42. Mises Stress for the Uncracked BWR CS Nozzle 3-D FEM Subjected to a BWR Thermal Shock Transient.....	77
Figure 43. BWR Thermal Shock Transient Applied to Three Regions of the BWR CS Nozzle 3-D FEM with a 1/4t Flaw	78
Figure 44. K_I near the 1/4t Location (Deepest Point) as a Function of Transient Time for the BWR Thermal Shock Transient.....	79
Figure 45. Hoop Stress Along the Selected Stress Path for the BWR CS Nozzle for a BWR Thermal Shock Transient at 0.1 Minute.....	80
Figure 46. Stress Intensity Factor (K_I) Along the Crack Front of the BWR CS Nozzle for BWR Thermal Shock Loading at 0.1 Minute	81
Figure 47. Hoop Stress Along the Selected Stress Path for the BWR CS Nozzle for a BWR Thermal Shock Transient at 30.4 Minutes	82
Figure 48. Stress Intensity Factor (K_I) Along the Crack Front of the BWR CS Nozzle for BWR Thermal Shock Loading at 30.4 Minutes.....	83
Figure 49. Hoop Stress Along the Selected Stress Path for the BWR CS Nozzle for a Pressurized BWR Thermal Shock Transient at 0.1 Minute	84
Figure 50. Stress Intensity Factor (K_I) Along the Crack Front of the BWR CS Nozzle for Pressurized BWR Thermal Shock Loading at 0.1 Minute.....	85
Figure 51. Geometry for the PWR Inlet Nozzle (from Reference [13])	86
Figure 52. 3-D FEM for the Uncracked PWR Inlet Nozzle.....	87
Figure 53. Stress Intensity (SINT) for the PWR Inlet Nozzle Subjected to 1,000 psi Internal Pressure.....	88
Figure 54. Hoop Stress Extraction Path Selected for the PWR Inlet Nozzle.....	89
Figure 55. Hoop Stress Along the Nozzle Corner Stress Path for the PWR Inlet Nozzle for 1,000 psi Internal Pressure.....	90
Figure 56. 3-D FEM for the PWR Inlet Nozzle with a Postulated 1/4t Circular Corner Crack.....	91
Figure 57. Stress Intensity Factor (K_I) Along the Crack Front for 1,000 psig Pressure Loading for the PWR Inlet Nozzle.....	92
Figure 58. Geometry for the PWR Outlet Nozzle (from Reference [13]).....	93
Figure 59. 3-D FEM for the Uncracked PWR Outlet Nozzle.....	94
Figure 60. Stress Intensity (SINT) for the PWR Outlet Nozzle Subjected to 1,000 psi Internal Pressure.....	95
Figure 61. Hoop Stress Extraction Path for the PWR Outlet Nozzle.....	96

Figure 62. Hoop Stress Along the PWR Outlet Nozzle Corner Path for 1,000 psi Internal Pressure	97
Figure 63. 3-D FEM for the PWR Outlet Nozzle with a Postulated $\frac{1}{4}t$ Circular Corner Crack	98
Figure 64. Stress Intensity Factor (K_I) Along the Crack Front for 1,000 psig Pressure Loading for the PWR Outlet Nozzle	99
Figure 65. Geometry for the BWR Instrument Nozzle (from Reference [14])	100
Figure 66. 3-D FEM for the Uncracked BWR Instrument Nozzle	101
Figure 67. Close-up View of 3-D FEM for the Uncracked BWR Instrument Nozzle	102
Figure 68. Stress Intensity (SINT) for the BWR Instrument Nozzle Subjected to 1,000 psi Internal Pressure	103
Figure 69. Stress Intensity (SINT) for the BWR Instrument Nozzle (Nozzle Insert Portion Only)	104
Figure 70. Hoop Stress Extraction Path and $1/4t$ Crack Definition for the BWR Instrument Nozzle	105
Figure 71. Hoop Stress Along the BWR Instrument Nozzle Corner Path for 1,000 psi Internal Pressure Loading	106
Figure 72. 3-D FEM for the BWR Instrument Nozzle with a Postulated $\frac{1}{4}t$ Circular Corner Crack	107
Figure 73. Stress Intensity Factor (K_I) Along the Crack Front Under 1,000 psig Pressure Loading for the BWR Instrument Nozzle	108

1. Introduction

Nonmandatory Appendix G of Section XI of the American Society of Mechanical Engineers (ASME) Code [1] provides methods for establishing fracture toughness criteria to protect against brittle fracture in ferritic pressure-retaining materials in components. The fracture toughness requirement for reactor pressure vessel (RPV) nozzles is specified in Paragraph G-2223 of Appendix G of ASME Code Section XI, which states that, “*A quantitative evaluation of the fracture toughness requirements for nozzles is not feasible at this time, but preliminary data indicate that the design defect size for nozzles, considering the combined effects of internal pressure, external loading and thermal stresses, may be a fraction of that postulated for the vessel shell.*” The technical basis for current Appendix G of ASME Code Section XI is mainly based on Welding Research Council (WRC) Bulletin WRC-175 [2], which contains an approximate method for analyzing postulated surface breaking defects located at the inside corner of nozzles. Since the publication of WRC-175, considerable progress has been made in fracture mechanics and finite element techniques, which makes it feasible to conduct detailed quantitative stress evaluations of RPV nozzles subjected to pressure and thermal gradient loadings during various operating events. Mehta, et al. [3] reviewed available stress intensity factor, K_I , calculation methods for a nozzle corner crack, and evaluated closed-form solutions that should be considered for incorporation into Appendix G of ASME Code Section XI.

This report describes stress analyses and fracture mechanics work performed to assess boiling water reactor (BWR) and pressurized water reactor (PWR) nozzles located in the reactor pressure vessel (RPV) adjacent to the active core. The primary motivation for this work was to gain a more thorough understanding of nozzle stress and fracture mechanics solutions so that they can be integrated into pressure-temperature (P-T) limits evaluations, especially for those nozzle configurations adjacent to the active core where radiation effects may be significant. Various RPV nozzle configurations were evaluated:

1. BWR recirculation outlet nozzle;
2. BWR core spray nozzle;
3. PWR inlet nozzle;
4. PWR outlet nozzle; and
5. BWR drill-hole style instrument nozzle.

These nozzle configurations were selected because they lie close enough to the active core region such that they may receive sufficient fluence prior to end-of-license (EOL), in which case they may become limiting with respect to P-T limits developed in accordance with Title 10 to the U.S. Code of Federal

Regulations (CFR), Part 50, Appendix G, “Fracture Toughness Requirements” [4] as part of the RPV material surveillance program. The BWR core spray nozzle, which is not typically close enough to the core region to experience significant fluence exposure, was selected to represent the BWR recirculation inlet nozzle because it is very similar in shape and size, but sufficient information for a recirculation inlet nozzle for detailed stress analysis modeling was not readily available in the NRC documentation system. These nozzles include the five configurations in the U.S. light water reactor (LWR) fleet that are close to the active core region and may experience the most significant fluence effects of most RPV nozzles.

Detailed stress and fracture mechanics analyses were conducted for these RPV nozzles. Closed-form expressions for RPV nozzle corner circular cracks were evaluated by comparing their predicted stress intensity factor results with stress intensity factor solutions from three-dimensional (3-D) finite-element models with postulated circular nozzle corner cracks. The purpose of these analyses was as follows:

- To model and understand differences in the pressure and thermal stress results using a two-dimensional (2-D) axisymmetric finite element model (FEM) vs. a 3-D FEM for all nozzle configurations. In particular, the ovalization (stress concentration) effect of two intersecting cylinders, which is typical of RPV nozzle configurations, was investigated;
- To verify the accuracy of linear elastic fracture mechanics (LEFM) closed-form solutions for stress intensity factor for a postulated nozzle circular corner crack for both thermal and pressure loading for all nozzle configurations;
- To assess the significance of attached piping loads on the stresses in the nozzle corner region;
- To assess the significance of applying pressure on the crack face with respect to the stress intensity factor for a postulated nozzle corner crack;
- To verify a scaling approximation used for the 3-D FEM K_I solutions for a $1/4t$ circular corner crack to estimate the stress intensity factors for a shallower $0.1t$ corner crack;
- To compare the 3-D FEM stress intensity factor solutions for a circular nozzle corner crack and a semi-elliptical nozzle corner crack and evaluate the flaw geometry effects on K_I along the crack front.

Chapter 2 provides a summary of the magnification factor method for computing the stress intensity factor for a nozzle corner crack. Chapters 3 through 7 provide the details of the analyses for each of the five nozzles in the order listed above. Chapter 8 provides a summary of this investigation, and presents conclusions. Chapter 9 provides a list of the references used for this work.

2. Magnification Factor Method for Calculating Stress Intensity Factor for Postulated Corner Cracks in Nozzles

A general purpose, linear superposition technique was proposed in Reference [5] to calculate the linear elastic stress intensity factor, K_I , for a postulated circular crack located in a nozzle corner. This technique provides a solution for K_I only at the deepest point of the postulated crack. This solution has been used in a variety of nozzle applications since it was proposed in 1978, and its adequacy was also discussed in Reference [3]. The adequacy of this solution is further assessed in this report for each of the selected nozzle configurations.

The K_I value for a postulated circular crack can be estimated using “magnification factors” obtained from the boundary integral equation (BIE) and influence function (IF) derivation [3]. Magnification factors, as used in this report and described in Reference [5], are constants that relate the calculated stress intensity factor for a given geometry to constant, linear, quadratic and cubic stress distributions. In the magnification factor method, an arbitrary stress distribution from an uncracked 3-D FEM (or 2-D FEM, with appropriate corrections) can be approximated by a third-order polynomial of the form:

$$\sigma = A_0 + A_1x + A_2x^2 + A_3x^3 \quad (1)$$

The curve-fitted stress distribution is a function of the distance, x , into the cross section of the nozzle corner, as shown in Figure 1. For a postulated circular nozzle corner crack on a nozzle with a rounded inner radius corner (Figure 2), the crack tip K_I can be superimposed from each term of the polynomial (FUN11 in Figure 4 of Reference [5]) as follows:

$$K_I = \sqrt{\pi a} \left[0.706A_0 + 0.537\left(\frac{2a}{\pi}\right)A_1 + 0.448\left(\frac{a^2}{2}\right)A_2 + 0.393\left(\frac{4a^3}{3\pi}\right)A_3 \right] \quad (2)$$

In Equation (2), the constants 0.706, 0.537, 0.448 and 0.393 are the magnification factors. For a postulated circular nozzle corner crack on a nozzle with a sharp inner radius corner (Figure 3), the superposition equation is as follows (FUN10 in Figure 4 of Reference [5]):

$$K_I = \sqrt{\pi a} \left[0.723A_0 + 0.551\left(\frac{2a}{\pi}\right)A_1 + 0.462\left(\frac{a^2}{2}\right)A_2 + 0.408\left(\frac{4a^3}{3\pi}\right)A_3 \right] \quad (3)$$

Since the method is based upon linear superposition, the stress distribution can be from any loading condition, such as internal pressure or thermal-induced stresses, and multiple stress distributions can be superimposed (added) together to estimate the total K_I . However, all loading on the crack face must be Mode I type loading, and the stress profile must be well described by the polynomial fit.

3. BWR Recirculation Outlet Nozzle

The first nozzle that was analyzed is a 26-inch diameter BWR recirculation outlet (RO) nozzle. There are usually two RO nozzles in most BWRs; they direct reactor coolant flow out of the RPV into each recirculation piping loop (i.e., the recirculation pump suction side of the piping) for subsequent return to the RPV. The dimensions of RO nozzles for the BWR-4 Vermont Yankee Nuclear Power Station RPV are shown in Figures 4 and 5 [6]. This RO nozzle configuration represents a BWR-4 design for a 206-inch diameter RPV manufactured by the Chicago Bridge and Iron Nuclear Company for the General Electric Company. Since there were some dimensional differences identified in the source documents, the dimensions used in the FEM shown in Figure 6 represent what is considered to be a reasonable compromise of those differences.

3.1 Uncracked BWR RO Nozzle 2-D Models

Axisymmetric 2-D FEMs are often utilized as a modeling approximation for 3-D cylindrical nozzles that penetrate cylindrical pressure vessels. However, a shortcoming with 2-D axisymmetric FEMs is that the vessel is modeled as a spherical shell instead of a cylindrical shell, as shown in Figure 7. The spherical approximation associated with the 2-D model will therefore under-estimate pressure hoop stress by as much as a factor of two, depending on the nozzle circumferential position, because pressure hoop stress in a sphere is one-half of that in a cylinder. Various techniques have been used to compensate for the stress differences resulting from this modeling approximation. One method is to represent the cylindrical shell as a spherical shell with an increased radius compared to that of the cylindrical shell [7]. This method compensates for the spherical model by increasing the vessel radius, and thus the stress in the spherical shell, which is proportional to radius. Another method is to use a scaling factor, or multiplier (also referred to as a stress correction factor (SCF)) applied to the RPV nominal hoop stress to account for the approximation [7]. These corrections are normally applied to pressure stresses, whereas thermal stresses do not require correction due to the relatively large diameter of the RPV (thereby approximating a flat plate with respect to the thermal solution so curvature effects are small). To investigate these effects, two 2-D FEMs were constructed for the BWR RO nozzle:

1. A 2-D axisymmetric FEM with a RPV (spherical) inside radius equal to the actual nominal radius, i.e., $R = 103.0$ in;
2. A 2-D axisymmetric FEM with a RPV (spherical) inside radius equal to twice the actual nominal radius, i.e., $R' = 2R = 206.0$ in;

Four portions of the reactor nozzle assembly were included in the two FEMs: (1) a portion of the RPV shell, (2) the nozzle forging, (3) the safe end, and (4) a portion of the attached pipe. The stainless steel cladding, with a thickness of 0.19 inch and residing along the inside surface of the RPV and nozzle forging, was also included in both of the FEMs to model the thermal stresses in the different materials. The 2-D uncracked FEMs were subjected to the internal pressure loading. The structural boundary and pressure loading conditions for the 2-D FEMs are shown in Figure 8. Symmetry boundary conditions were applied to the far end of the RPV wall; an internal pressure of 1,000 psig was applied to all internal surfaces of the RPV wall, nozzle forging, safe end, and pipe; and, a membrane cap, or blow-off, load was applied to the end of the pipe (representing the axial stress due to pressure in a closed-end piping system). The blow-off loads for the 2-D FEMs (and also the 3-D models, described later) were calculated as follows:

$$P_{blow-off} = \frac{PD_i^2}{D_o^2 - D_i^2} \quad (4)$$

where D_i (inches) and D_o (inches) are the inner and outer diameters of the RPV wall or pipe, as appropriate, and P is the applied pressure (psig). All analyses performed in this study utilized the ABAQUS Version 6.9-EF finite element software [8]. Eight (8) node axisymmetric elements were used in the 2-D FEMs.

Figure 9 displays the stress results of the 2-D model with a RPV shell internal radius of $2R = 206.0$ inches. The stress intensity (SINT), a variable available in the ANSYS software [9], as used in Reference [6], is shown in Figure 9. The stress intensity is defined as:

$$SINT = \text{Max} (|\sigma_1 - \sigma_2|, |\sigma_2 - \sigma_3|, |\sigma_3 - \sigma_1|) \quad (5)$$

where σ_1 , σ_2 , σ_3 are the three principal stresses. The peak value of the stress intensity is 32,880 psi for the 2-D model with an RPV shell internal radius of $2R = 206.0$ inches, which is very close to the value reported as 31,272 psi in Reference [6]. The analyses in Reference [6] were conducted with ANSYS and there is a slight geometry difference between the FEM in this study and that in Reference [6] due to the dimensional differences previously described. Nevertheless, despite these differences, the agreement in stress results between Figure 9 and Reference [6] is very good (within 5%). Figure 10 depicts the stress intensity results of the 2-D model with an RPV shell internal radius of $R = 103.0$ in., and the peak value is 16,130 psi (i.e., approximately one-half of the $2R$ results, as expected).

3.2 Uncracked BWR RO Nozzle 3-D Model

A 3-D FEM for the RO nozzle was constructed with 20-node brick elements using ABAQUS/CAE Version 6.9-EF. The actual RPV inside radius ($R = 103$ inches) was modeled. Figure 11 displays the detailed components in the 3-D FEM including the RPV wall, nozzle, safe end, and pipe. Figure 12 illustrates the boundary and loading conditions applied to the 3-D model: symmetry boundary conditions were applied on both axial cut planes and the lower circumferential cut plane; blow-off pressure was applied to the far ends of the RPV wall and pipe; 1,000 psig internal pressure was applied to all of the inner surfaces of the model.

3.3 Assessment of Pressure Stresses

Figure 13 displays the stress intensity profile for the uncracked RO nozzle 3-D FEM. The maximum stress occurs in the nozzle corner in the axial cut plane at the top of the nozzle, and the stress varies significantly around the circumference of the nozzle. In the 3-D model, the peak value of the stress intensity due to pressure is 49,570 psi for an applied internal pressure of 1,000 psig. Therefore, the hoop stress correction factor between the 3-D and 2-D FEMs is 3.1 (calculated as $49,570/16,130$ for the same RPV internal diameter). This factor is slightly larger than the bounding factor of 3.0 suggested for use in Reference [7], which is most likely caused by the skewed shape of this nozzle configuration, which is a factor that was not investigated in Reference [7]. This value corresponds well with the nozzle stress index value of 3.1 for normal (circumferential) stress contained in Table NB-3338.2(c)-1 of Section III of the ASME Code [10].

3.4 Assessment of Attached Piping Loads

The 3-D RO nozzle FEM was also subjected to the piping interface loads, as defined in Table 4 of Reference [6]. The objective was to determine if these loads cause significant stresses and, therefore, should be factored into establishing pressure-temperature (P-T) limits for nozzles. The applied piping interface loads include forces F_x , F_y , F_z and moments M_x , M_y and M_z , with directions as shown in Figure 14. The values of the piping loads are listed in Table 1.

Table 1. Piping Loads Applied to the RO Nozzle

Piping Load	Value
F_x (kip)	20.0
F_y (kip)	20.0
F_z (kip)	30.0
M_x (kip-in)	2,004.0
M_y (kip-in)	3,000.0
M_z (kip-in)	2,004.0

Figure 15 compares the maximum principal stress around the nozzle corner subjected to 1,000 psig internal pressure loading (left side of figure) and the same pressure loading combined with the piping interface loads (right side of figure). The stress profiles in the nozzle corner are very similar for these two loading conditions and the incremental stress caused by the attached piping loads is insignificant compared to the stress due to the applied pressure loading. Figure 16 compares the hoop stress along a 45° path through the nozzle corner at the azimuth of maximum pressure stress both with and without attached piping loads. The 3-D FEM results indicate that the incremental stress at the internal surface of the nozzle corner is about 2,100 psi due to the attached piping loads, which is small (4%) compared to the pressure stress of ~50,000 psi. In addition, it is noteworthy that the stress due to the attached piping loads were calculated by hand in Reference [6] and found to be less than 500 psi at the nozzle corner (identified as “Blend Radius” in Reference [6]), which is lower by more than a factor of four compared to the stresses predicted by the 3-D FEM solution. Therefore, the methodology of the hand calculation used for evaluating the attached piping loads in Reference [6] underestimates stresses in the thick nozzle corner region.

The results obtained for the RO nozzle are considered to be typical with respect to nozzle attachment load behavior. Therefore, nozzle attachment loads were not evaluated in the assessments for the other nozzles.

3.5 Assessment of Thermal Stresses

The 2-D FEM ($R = 103$ inches) and the 3-D FEM for the RO nozzle were subjected to a cooldown thermal transient to estimate thermal stresses. The cooldown transient was selected for evaluation as it is typically evaluated for P-T limits. The internal surfaces of the models were subjected to a forced convection cooldown at a rate of 100 °F/hr (except for a 10-minute period during the middle of the event), as defined in Reference [6] for the Shutdown event (Transient No. 10). Temperature-dependent material properties for the RPV wall, nozzle, clad, safe end, and pipe were used, as obtained from Section II, Part D of the ASME Code [11], and are listed in Reference [6].

The uncracked 2-D and 3-D FEMs were subjected to the Shutdown transient. The maximum principal stress plots for the 3-D and 2-D models are depicted in Figures 17 and 18, respectively, at a transient time of 119.5 minutes, which is when the maximum thermal stress was determined to occur. The locations of the maximum thermal stress (the grey area in Figures 17 and 18) are different in the 2-D and 3-D models. In the 3-D FEM, the maximum stress is located in the nozzle cladding near the axial cut plane (Figure 17), while the maximum stress is located in the nozzle cladding near the circumferential cut plane in the 2-D FEM (because it is an axisymmetric model, Figure 18). Figure 19 shows the temperature and maximum principal stress at the one quarter thickness ($1/4t$) location along a 45° path through the nozzle corner as a function of transient time for both the 2-D and 3-D FEMs. The plot shows that the value of the maximum principal thermal stress occurs at 119.5 minutes, and the results from the 2-D FEM closely approximate the results of the 3-D FEM.

Figure 20 shows the variation of maximum principal stress (MPS) around the circumference of the nozzle at the time during the transient when the peak value of thermal stress was reached (119.5 minutes). The stress path around the circumference of the nozzle is illustrated by the red line on the FEM mesh in Figure 20. Stresses at two locations (clad material and base material) were compared. As noted by this comparison, the stresses along the clad path are significantly higher than those along the base material path. However, the stresses do not vary significantly around the circumference of the nozzle for either material. These results demonstrate that, for thermal stresses, the 2-D FEM predicts values that are slightly higher than a 3-D FEM because there is no significant variation in the stress around the nozzle circumference. This is different than the circumferential stress variation around the nozzle subjected to the pressure loading, where the circumferential variation in stress is very significant. Therefore, the use of the thermal stresses along the same path selected for maximum pressure stress is appropriate.

The results obtained for the RO nozzle are considered to be typical with respect to thermal stress behavior. Therefore, except for thermal shock loading unique to the BWR feedwater nozzle during startup conditions, ramped thermal cooldown loading was not evaluated in the assessments for the other four nozzle configurations.

3.6 BWR RO Nozzle 3-D Model with a Postulated Circular Corner Crack

A 3-D FEM of the RO nozzle including a circular corner crack was constructed using ABAQUS/CAE Version 6.9-EF to determine the Mode I stress intensity factor along the crack front. A $1/4t$ circular flaw was postulated at the inside corner using finite element techniques for comparison to the magnification factor method solution. The mesh for the cracked model includes the same portions of the nozzle assembly as the uncracked 3-D FEM. The postulated $1/4t$ circular crack was included in the FEM, as shown in Figures 21 and 22. Collapsed prism elements were employed at the postulated crack tip, and the

midside nodes of these elements were moved to the $1/4t$ point location to produce an appropriate singularity for LEFM analyses. A highly-refined, focused mesh was utilized along the crack front to achieve solution convergence and obtain path-independent stress intensity factors. The 3-D cracked BWR RO nozzle FEM has 68,169 nodes and 14,874 elements, in which 5,631 solid brick elements were used in the crack region.

Further demonstration of the adequacy of the magnification factor method for calculating stress intensity factor for a nozzle corner crack is demonstrated in this section for the BWR RO nozzle. The hoop stresses from the uncracked RO nozzle 2-D and 3-D FEMs were extracted as a function of section thickness along a 45° path in the nozzle corner at the azimuth of maximum pressure stress. The extraction path for the RO nozzle is shown in Figure 23. Figure 24 shows the extracted pressure hoop stresses for the 2-D axisymmetric and 3-D FEMs subjected to 1,000 psig internal pressure. For both FEMs, the peak pressure hoop stress occurs at the internal surface of the nozzle corner, and the peak value of the 3-D FEM is about 1.5 times higher than that of the 2-D axisymmetric FEM (for the $2R = 206$ -inch model). The extracted hoop stress from the uncracked 3-D FEM was curve-fit with a third-order polynomial using Equation (1), and the K_I value was then estimated using Equation (2) (since the RO nozzle has a rounded inner radius corner). To provide a bounding estimate of stress intensity factor, it is important for the curve fit to either accurately estimate, or over-estimate, the stress over the range of crack depths considered (i.e., for this study, at one-quarter of the wall thickness).

3.6.1 Internal Pressure Loading for Cracked 3-D Model

The 3-D FEM for the RO nozzle with a postulated $1/4t$ circular corner crack was subjected to 1,000 psig internal pressure applied to all inner surfaces using the same boundary conditions as those for the uncracked 3-D FEM. Figure 25 shows the stress intensity factor, K_I , as a function of pressure loading using different integral contours. The calculated K_I values using different contours are essentially the same. Therefore, path-independent K_I values are achieved, which also confirms the validity of the FEM.

Figure 26¹ shows the K_I values along the crack front from the RPV wall side of the crack ($\approx 0^\circ$ angle) to the nozzle inside surface side of the crack ($\approx 100^\circ$ angle) (the K_I values for the cladding layer are not included). The lowest value of K_I occurs at the deepest point of the circular crack front. The 3-D solution is compared with the magnification factor method solution in Figure 26. The magnification factor method solution result (the square point in Figure 26) over-estimates the 3-D finite element stress prediction at the deepest point of the crack. However, the magnification factor method solution is non-conservative compared to the maximum K_I at the ends of the crack. The 3-D finite element solution for a $1/4t$ circular corner crack was scaled to estimate the K_I solution for a $0.1t$ circular corner crack, which is a

¹ “CFP” in Figure 26 refers to “crack face pressure.” Refer to Section 3.7 for discussion of CFP.

more reasonably-sized flaw that can be detected by volumetric examination. The scaling of the K_I solution from a $1/4t$ circular corner crack to a $0.1t$ circular corner crack was conducted as follows:

1. Calculate the K_I values for $1/4t$ circular corner crack ($K_{I-1/4t}$) and $0.1t$ circular corner crack ($K_{I-0.1t}$) using the magnification factor method;
2. Calculate the ratio of $K_{I-0.1t}/K_{I-1/4t}$;
3. Scale the 3-D finite element solution for a $1/4t$ circular corner crack front using the ratio calculated in Step 2 to estimate the K_I solution for a $0.1t$ circular corner crack.

Figure 26 shows that the K_I calculated at the deepest point of the $1/4t$ flaw by the magnification factor method solution exceeds the K_I for the entire crack front solution for a $0.1t$ flaw. The conservatism of assuming a large ($1/4t$) flaw bounds the potential non-conservatism of evaluating only the deepest point of the crack using the magnification factor method solution. Therefore, as part of using the simplified magnification factor method solution, it is important to use at least a $1/4t$ postulated flaw size to maintain a conservative stress intensity factor estimate; any use of reduced flaw sizes need to be justified by appropriately considering the variation in K_I along the face of the crack.

3.6.2 Evaluation of a 0.1t Circular Flaw to Verify the Scaling Approximation

Additional analysis was conducted to verify the methodology that was used in Section 3.6.1 to scale the $1/4t$ circular corner crack stress intensity factor results to estimate the stress intensity factor profile for a $0.1t$ circular corner crack. The BWR RO nozzle was evaluated for this assessment since this nozzle has the highest K values due to pressure (based on comparison of Figures 26, 39, 57, 64, and 73).

An additional 3-D finite-element analysis was conducted for the cracked RO nozzle to determine the Mode I stress intensity factor along the crack front for a $0.1t$ circular corner flaw using finite element techniques for comparison to the magnification factor method solution and the results scaled from the $1/4t$ flaw solution. To perform this assessment, a postulated $0.1t$ circular corner crack was included in the 3-D FEM instead of the $1/4t$ circular corner crack previously considered. Similar to that shown in Figure 21 for the $1/4t$ circular corner crack, the $0.1t$ flaw depth was defined as the 10% of the through-wall path thickness from the inner surface to the outer surface along the direction normal to the tangent of the middle point of the nozzle inner corner. The 3-D FEM including the $0.1t$ circular corner crack is shown in Figure 27, and was constructed using ABAQUS/CAE Version 6.11. As with the $1/4t$ crack model, a highly-refined, focused mesh was utilized along the $0.1t$ crack front to achieve solution convergence and obtain path-independent stress intensity factors.

The 3-D FEM for the RO nozzle with a postulated $0.1t$ circular corner crack was subjected to 1,000 psig internal pressure applied to all modeled inner surfaces. Figure 28 shows the K_I values along the crack front from the RPV wall side of the crack ($\approx 0^\circ$ angle) to the nozzle inside surface side of the crack ($\approx 100^\circ$ angle) (the K_I values for the cladding layer are not included). The 3-D FEM results for the $0.1t$ circular corner crack agree with the scaled results obtained using the $1/4t$ circular corner crack solution. Therefore, the scaling factor approach for estimating the $0.1t$ circular corner crack solution is adequate, and the solution using the magnification factor method (the green point in Figure 28) over-estimates the 3-D FEM stress intensity factor result at the deepest point of the $0.1t$ crack.

3.6.3 Evaluation of a $0.1t$ Semi-Elliptical Nozzle Corner Flaw

A third cracked FEM for BWR RO nozzle was constructed that included a postulated $0.1t$ semi-elliptical corner crack. The semi-elliptical crack was assumed to have an aspect ratio of 6:1 (length-to-depth), consistent with the aspect ratio postulated in Appendix G of ASME Code Section XI. As indicated in Figure 21, the postulated elliptical crack was assumed to lie on the same centerlines as the circular corner crack. The crack length of $0.6t$ was defined along elliptical centerline such that the ellipse has a 6-to-1 aspect ratio. This crack orientation assumption leads to a relatively flat crack profile in the nozzle corner with an actual crack length in the nozzle corner that is less than $0.6t$, as illustrated in Figure 21. The completed 3-D FEM for the $0.1t$ elliptical corner crack is shown in Figure 29.

The 3-D FEM for the RO nozzle with a postulated $10\%t$ semi-elliptical corner crack was subjected to 1,000 psig internal pressure applied to all inner surfaces. Figure 30 shows the K_I values along the crack front from the RPV wall side of the crack ($\approx 0^\circ$ angle) to the nozzle inside surface side of the crack ($\approx 100^\circ$ angle) (the K_I values for the cladding layer are not included). The maximum value of K_I occurs near the center of the $0.1t$ semi-elliptical crack front. The K_I profile shape is an inflection of the profile shape for the $1/4t$ circular crack, and the magnification factor method (the green point in Figure 30) significantly under-estimates the 3-D FEM stress intensity factor result at the deepest point of the crack. However, comparing the results in Figure 30 to those shown in Figure 28, the result of the magnification factor method for a postulated $1/4t$ circular corner crack bounds all FEM results for the smaller $0.1t$ flaws. Therefore, it is evident from these results that the $1/4t$ circular corner crack solution may be used to provide bounding fracture mechanics results for nozzle P-T limits evaluations, but that flaw geometry significantly affects K_I values along the crack front and should therefore be considered for smaller flaw size assumptions.

3.6.4 Cooldown Thermal Loading for Cracked 3-D Model

The thermal hoop stresses from the uncracked 3-D RO nozzle FEM subjected to the cooldown thermal transient loading were extracted as a function of section thickness along the 45° path in the nozzle corner, as shown in Figure 31. The peak thermal hoop stress occurs at the internal surface of the nozzle corner, and there is a large stress gradient between the cladding and nozzle forging caused by the differential thermal expansion of these two materials. As a result, a third-order polynomial does not fit the thermal hoop stress well across the total section thickness. To investigate the effects of this, the thermal hoop stress was curve fit in three ways: (1) the thermal hoop stress along the entire path thickness was used; (2) the thermal hoop stress in the nozzle forging near the 1/4t depth only was used (noted as “partial” in Figure 31); and (3) the thermal hoop stress through the thickness of nozzle forging material (i.e., neglecting the stress in the cladding) was used. The polynomial coefficients from these three curve fits were used to estimate stress intensity factors for the 1/4t corner circular crack using the simplified magnification factor method solution.

The 3-D FEM for the cracked RO nozzle with the 1/4t circular corner crack was also subjected to the cooldown thermal transient loading described previously. Figure 32 shows the K_I values along the 1/4t circular crack front in the nozzle forging material. Similar to the pressure loading evaluation for the 1/4t circular corner crack, the lowest value of K_I due to thermal loading occurs at the deepest point of the circular crack front. The 3-D FEM solution is also compared with the magnification factor method solution (for the deepest point) in Figure 32. The magnification factor method solution result using the Option (1) curve fit (the square point in Figure 32) bounds the value from the cracked 3-D FEM solution, and the magnification factor method solution results using the Option (2) or (3) curve fit are slightly lower than the cracked 3-D finite element solution. Therefore, the selection of the appropriate curve fit has a significant influence on the calculated results. In this example, the overall stress distribution (including the higher cladding stresses) for the magnification factor method solution provides a bounding result at the deepest point of the crack for thermal stresses. However, this result may not remain true for other thermal transients. Care needs to be taken that the polynomial fits for any stress distributions are a good approximation for the through-thickness stress distribution. A plot showing the polynomial fit to the stress distribution and sensitivity studies should be provided for a part of the technical justification provided for the fitting assumptions used. If a reasonable fit is not obtained, polynomial weight function solutions should not be used.

It is also noteworthy that the K_I values for all points along the crack front for thermal loading for smaller (i.e., 0.1t) flaws may not necessarily be bounded by the 1/4t solution for the deepest point of the crack. However, the K_I for thermal loading is significantly lower than the K_I for pressure loading (on the order of

10-30 ksi $\sqrt{\text{inch}}$ for thermal loading from Figure 32 vs. 80-100 ksi $\sqrt{\text{inch}}$ for pressure loading from Figure 28). Therefore, it is judged that the conservatism of the K_I magnification factor method solution for a $1/4t$ flaw under combined pressure and thermal loading remains an adequate and bounding simplification for $1/4t$ flaws. Again, it should be emphasized that any use of reduced flaw sizes need to be justified by appropriately considering the variation in K_I along the face of the crack as well as differences in flaw shape.

3.7 Assessment of Crack Face Pressure Effects

An additional FEM run was made adding pressure to the postulated crack faces for the cracked 3-D FEM of the RO nozzle with the $1/4t$ corner circular crack subjected to 1,000 psig internal pressure. As indicated in figure 26, the crack face pressure (CFP) slightly increases the K_I along the crack front (the red line shown in Figure 26); however, the magnification factor method solution result, which does not include crack-face pressure, still remains bounding. The effect of crack face pressure is therefore considered to be small and its absence from the magnification factor method solution is compensated for by the use of a large postulated flaw size ($1/4t$). Consideration of reduced flaw size should also account for the effects of pressure loading on the face of the postulated crack.

4. BWR Core Spray Nozzle

Similar to the RO nozzle, stress and fracture mechanics analyses were conducted for a BWR core spray (CS) nozzle to evaluate its unique size and shape characteristics. As mentioned previously, the core spray nozzle was selected to represent the BWR recirculation inlet nozzle, which is very similar in shape and size, but detailed information on a recirculation inlet nozzle sufficient to perform this assessment was not readily available in the NRC documentation system. The dimensions of the CS nozzle for the Vermont Yankee Nuclear Power Station, which is a BWR-4 with a 206-inch diameter RPV, are defined in Reference [12], and are shown in Figure 33. The assessment for the CS nozzle was limited to 3-D FEM studies only, as discussed in Section 3 for the RO nozzle. In addition to pressure loading, thermal shock loading applicable to similar BWR nozzle configurations was also investigated for the BWR CS nozzle. The conclusions made with respect to the other loadings evaluated for the RO nozzle (i.e., ramped thermal transient cooldown loading, attached piping loads, and crack face pressure loading) are considered to be applicable for the CS nozzle.

4.1 Uncracked BWR CS Nozzle Model

The 3-D FEM for the uncracked CS nozzle is shown in Figure 34; it was constructed with 20-node brick elements using ABAQUS/CAE Version 6.9-EF. The CS nozzle FEM consists of portions of the RPV shell, the nozzle forging, cladding, the safe end, and a weld overlay that had been applied to the nozzle-to-safe end weld of this nozzle². Figure 35 displays the stress intensity profile for the uncracked 3-D FEM subjected to 1,000 psig internal pressure. The maximum pressure stress intensity occurs in the nozzle corner in the vessel axial plane, and the stress varies significantly in the circumferential direction around the circumference of the nozzle. The peak pressure hoop stress from the uncracked 3-D FEM is 49,790 psi (calculated as the peak SINT of 50,790 psi from Figure 35 minus the radial pressure stress of 1,000 psi). The nominal pressure hoop stress in the RPV wall is $PR/t = 18,310$ psi. Therefore, the estimated SCF for the BWR CS nozzle is 2.7 (calculated as $49,790/18,310$).

The pressure hoop stress was extracted from the uncracked CS nozzle FEM along a path defined normal to the tangent at the midpoint to the internal nozzle corner at the location of peak pressure hoop stress, as shown in Figure 36. Figure 37 shows the extracted pressure hoop stress through the section thickness of the nozzle corner, and the pressure stress distribution approximated by a third-order polynomial.

² Stress analyses of the nozzle showed that the effect of the weld overlay is insignificant to stresses in the nozzle corner.

4.2 BWR CS Nozzle Model with a 3-D Simulated Circular Corner Crack

A 3-D FEM for the CS nozzle with a postulated $1/4t$ circular corner crack was constructed using ABAQUS/CAE Version 6.9-EF. The mesh includes the same portions of the nozzle assembly as the uncracked 3-D FEM described in Section 4.1. The postulated $1/4t$ circular corner crack included in the FEM is shown in Figure 38. Collapsed prism elements were employed at the crack tip, and the mid-side nodes of these elements were moved to the $1/4t$ point location to produce an appropriate singularity for LEFM analyses. A highly refined, focused mesh was used along the crack front to achieve solution convergence and obtain path-independent stress intensity factors.

4.2.1 Internal Pressure Loading for Cracked 3-D Model

The 3-D FEM for the CS nozzle with a postulated $1/4t$ circular corner crack was subjected to 1,000 psig internal pressure loading along all internal model surfaces. Figure 39 displays K_I values along the crack front from the RPV wall side of the crack ($\approx 0^\circ$ angle) to the nozzle inner surface side of the crack ($\approx 90^\circ$ angle). Consistent with the RO nozzle results, the lowest value of K_I occurs at the deepest point of the circular crack front.

The 3-D FEM fracture mechanics solution is compared with the K_I calculated by the magnification factor method solution in Figure 39. Similar to the results for the BWR RO nozzle, the magnification factor method solution result (the square point in Figure 39) is bounding compared with the 3-D FEM solution at the deepest point of the crack. However, the magnification factor method solution does not bound the maximum K_I at the ends of the crack. The 3-D FEM solution for a $1/4t$ circular corner crack was scaled to estimate the K_I solution for a $0.1t$ flaw, which is a more reasonable flaw size that can still be reliably detected by volumetric examination. The magnification factor method solution for a $1/4t$ flaw at its deepest point bounds the entire crack front solution for a $0.1t$ flaw. Therefore, the conservatism of assuming a $1/4t$ flaw bounds the potential non-conservatism of evaluating only the deepest point of the crack if the magnification factor method is used. Consistent with the RO nozzle results, as part of utilizing the simplified magnification factor method solution, it is important to maintain the use of a large postulated flaw size; any use of reduced flaw sizes need to be justified by appropriately considering the variation in K_I along the face of the crack as well as differences in flaw shape.

4.2.2 Thermal Shock Loading for Cracked 3-D Model

The uncracked 3-D FEM for the CS nozzle was subjected to a thermal shock transient loading, which is illustrated in Figure 40. This transient was selected because it represents the Turbine Roll (Feedwater Initiation) event associated with the BWR Startup transient. Since this event is an unavoidable part of the BWR startup process, it is typically evaluated for the feedwater nozzle (non-beltline) P-T limits associated with 100°F/hr heatup/cooldown conditions. The intent of this evaluation was to determine if

the magnification factor method solution properly estimates K_I values for thermal shock loading for the CS nozzle (which approximates the BWR feedwater nozzle size and shape), as compared to the ability of the magnification factor method solution to estimate K_I for the slow ramp loading evaluated for the RO nozzle.

The nozzle, safe end, and RPV inner surfaces of the CS nozzle FEM were divided into three thermal regions for application of the thermal boundary conditions for the shock loading, as shown in Figure 41: (1) the nozzle flow path region (blue); (2) the RPV inside surface region (red); and (3) the nozzle inner corner region (green). The initial fluid temperature was assumed to be 550 °F in all three regions. A constant fluid temperature of 550 °F was assumed for the RPV region during the entire transient. Consistent with the design basis transient definition, the coolant temperature was assumed to decrease instantaneously from 550 °F to 100 °F at the beginning of the transient (time = 0) in the nozzle flow path region. After 30 minutes, the temperature was instantaneously increased to 250 °F, followed by a ramp to 420 °F over 30 minutes. The average temperature between the RPV inside surface region and the nozzle flow path region was applied to the nozzle corner region. Figure 42 shows the Mises stress of the uncracked CS nozzle 3-D FEM subjected to the thermal shock transient. There is no significant variation in stress around the nozzle circumference, similar to that observed for the RO nozzle subjected to the cooldown transient, as described in Section 3.5.

The 3-D FEM for the BWR CS nozzle with a postulated $1/4t$ circular corner crack was subjected to the same thermal shock transient, as shown in Figure 43. Figure 44 displays the K_I values at the $1/4t$ location (the deepest point along the crack front) as a function of transient time. In this case, there are two peak K_I values: one is at the beginning of the transient (at a time of ≈ 0.1 minute) when the initial temperature shock occurs, and the second peak K_I value occurs when the upward temperature shock occurs (at a time of ≈ 30.4 minutes).

At the transient time of 0.1 minute, thermal hoop stresses were extracted from the uncracked FEM subjected to the thermal shock transient along a path defined normal to the tangent at the midpoint to the internal nozzle corner, as shown in Figure 36. Figure 45 shows the extracted thermal hoop stresses through the thickness of the nozzle corner, and the stress distribution as approximated by a third-order polynomial. There is a large hoop stress through-wall gradient at the beginning of the thermal shock (i.e., a “skin” stress effect). As a result, the third-order polynomial does not adequately approximate the complete through-wall thermal hoop stress profile. Figure 46 shows the K_I values along the crack front from the RPV wall side of the crack ($\approx 0^\circ$ angle) to the nozzle inner surface side of the crack ($\approx 90^\circ$ angle). The shape of the K_I profile is different from that of the RO nozzle ramp thermal loading; it inflects downward as opposed to upward. In the previous cooldown transient for the RO nozzle, as described in Section 3.5, the RO nozzle experienced a uniform through-wall temperature gradient due to the relatively

slow ramped thermal loading. For the thermal shock transient applied to the CS nozzle, the through-wall temperature gradient is highly non-linear because of the rapid thermal shock assumed for this transient. In addition, as shown in Figure 43, the crack front crosses three different thermal regions, which causes different temperature gradients along the crack front. The FEM K_I values at the deepest point of the crack front are compared with the estimation by the magnification factor method in Figure 46. As shown in Figure 46, the magnification factor method solution does not produce a bounding estimate of stress intensity factor for thermal shock loading. If a partial thickness hoop stress curve fit is used (for example, the portion of the hoop stress from ≈ 1 inch from the inner surface up to the outer surface in Figure 45), the K_I value becomes negative since the hoop stress is compressive over this entire region.

Figure 47 displays the extracted thermal hoop stresses from the uncracked FEM at a transient time of 30.4 minutes (when the second peak K_I value occurs in Figure 44). Figure 48 depicts the K_I values along the crack front at a transient time of 30.4 minutes, and compares these values with the estimation of K_I by the magnification factor method at the deepest point of the crack. In this case, the magnification factor method provides bounding stress intensity factor results.

The uncracked and cracked FEMs for CS nozzle were also subjected to the thermal shock combined with 1,000 psig internal pressure loading. Figure 49 displays the extracted total hoop stress from the uncracked FEM subjected to the pressurized thermal shock at the transient time of 0.1 minute, and the stress is approximated by a third-order polynomial fit across the entire section thickness. Figure 50 depicts the K_I values along the crack front at 0.1 minute, and these results are compared with the K_I estimated by magnification factor method solution at the deepest point of the crack front. These results indicate that, although the thermal K_I is under-predicted, the combined K_I due to both pressure and thermal loading is still estimated reasonably well by the magnification factor method solution because the internal pressure loading (which is over-predicted at the deepest point by the magnification factor method solution) dominates the loading compared with the thermal shock loading. Therefore, the magnification factor method solution is considered to be a valid approximation for thermal shock loading when pressure effects are also considered, as is the case with P-T limits evaluations for nozzles of this configuration.

5. PWR Inlet Nozzle

Similar stress and fracture mechanics analyses were conducted for a 28-inch diameter PWR inlet nozzle. The geometry was obtained from drawings of the Oak Ridge National Laboratory (ORNL) Pressure Vessel Research Users Facility (PVRUF) RPV [13], as shown in Figure 51. The PVRUF vessel was manufactured by Combustion Engineering (CE) for the Westinghouse Electric Company, but never entered service after fabrication was completed in December 1981. The vessel was later transported to ORNL and was used for research programs related to the structural integrity of RPVs.

5.1 Uncracked PWR Inlet Nozzle Model

A 3-D FEM was constructed for the uncracked PWR inlet nozzle using 20-node brick elements, and is shown in Figure 52. The FEM consists of portions of the RPV shell, the nozzle forging, cladding, and the safe end. Figure 53 shows the pressure stress intensity profile for the uncracked 3-D FEM subjected to 1,000 psig internal pressure loading. The maximum pressure stress occurs in the nozzle corner in the vessel axial plane, and the stress varies around the nozzle circumference. The peak pressure hoop stress from the uncracked 3-D FEM is 28,940 psi (calculated as the peak SINT of 29,940 psi from Figure 53 minus the radial pressure stress of 1,000 psi). The nominal pressure hoop stress in the RPV wall is $PR/t = 10,023$ psi. Therefore, the SCF for the PWR inlet nozzle is 2.9 (calculated as 28,940/10,023).

The pressure hoop stresses were extracted from the uncracked nozzle 3-D FEM along a path normal to the tangent defined at the midpoint to the internal nozzle corner at the location of peak pressure hoop stress, as shown in Figure 54. Figure 55 shows the extracted pressure hoop stress profile and the pressure stress distribution approximated by a third-order polynomial.

5.2 PWR Inlet Nozzle Model with a 3-D Simulated Circular Corner Crack

A 3-D FEM was constructed using ABAQUS/CAE Version 6.9-EF for the cracked PWR inlet nozzle. The mesh included the same portions of the nozzle assembly as the uncracked 3-D FEM. A postulated 1/4t circular corner crack was included in the FEM, as shown in Figure 56.

The 3-D FEM for the PWR inlet nozzle with a postulated 1/4t circular corner crack was subjected to 1,000 psig internal pressure loading. Figure 57 displays K_I along the crack front from the RPV wall side of the crack ($\approx 0^\circ$ angle) to the nozzle inner surface side of the crack ($\approx 90^\circ$ angle). Similar results as those obtained for the BWR RO and CS nozzles were observed: the lowest value of K_I occurs at the deepest point of the circular crack front; the magnification factor method solution results (the two points in Figure 57) are bounding compared with the actual and estimated 3-D finite element solutions at the deepest point

of the $1/4t$ and $0.1t$ cracks, respectively; the magnification factor method solutions do not bound the maximum K_I values at the ends of the cracks; the deepest point magnification factor method solution for $1/4t$ flaw bounds the entire estimated crack front solution for a $0.1t$ flaw. Therefore, similar to the conclusions made for the BWR RO and CS nozzles, the conservatism of assuming a $1/4t$ flaw bounds the potential non-conservatism of evaluating the K_I at the deepest point of the crack, and, as part of using the simplified magnification factor method solution, it is important to maintain the use of a large postulated flaw size. Any use of reduced flaw sizes need to be justified by appropriately considering the variation in K_I along the face of the crack as well as differences in flaw shape.

6. PWR Outlet Nozzle

Similar stress and fracture mechanics analyses were conducted for a 30-inch diameter PWR outlet nozzle. As with the PWR inlet nozzle, the geometry was obtained for the PVRUF RPV [13], and is shown in Figure 58. The PWR outlet nozzle is different from the previous three nozzles in that the PWR outlet nozzle has a lip due to the nozzle forging penetrating past the RPV shell, which results in significantly different stress distributions compared with the previous nozzles. As a result of the presence of the nozzle lip, the placement of a nozzle corner flaw may not be obvious. In this investigation, the corner flaw was located at the inside corner of the nozzle consistent with the placement of flaws for the other nozzles evaluated in this report.

6.1 Uncracked PWR Outlet Nozzle Model

A 3-D FEM was constructed for the uncracked PWR outlet nozzle using 20-node brick elements, and is shown in Figure 59. The FEM consists of portions of the RPV shell, the nozzle forging, cladding, and the safe end. The PWR outlet nozzle is unique from other nozzle designs in that the nozzle penetrates beyond the inner surface of the RPV wall, as shown in Figure 59. Figure 60 displays the pressure stress intensity profile of the uncracked 3-D FEM subjected to 1,000 psig internal pressure loading. The maximum pressure stress occurs at the inner fillet between the nozzle forging and RPV wall (instead of the nozzle inner corner in the previous nozzles) in the vessel axial plane. Similar to the other nozzles, the pressure stress varies around the nozzle circumference. The peak pressure hoop stress from the uncracked 3-D FEM is 33,770 psi (calculated as the peak SINT of 34,770 psi from Figure 60 minus the radial pressure stress of 1,000 psi). The nominal pressure hoop stress in the RPV wall is $PR/t = 10,023$ psi. Therefore, the SCF for the PWR outlet nozzle is 3.4 (calculated as $33,770/10,023$).

The pressure hoop stresses were extracted from the uncracked nozzle 3-D FEM along a path normal to the tangent defined at the midpoint in the internal nozzle corner, as shown in Figure 61. This location was selected consistent with the approach used to locate cracks in the other nozzle configurations. Figure 62 shows the extracted pressure hoop stresses and the pressure stress distribution approximated by a third-order polynomial.

6.2 PWR Outlet Nozzle Model with a 3-D Simulated Circular Corner Crack

A 3-D FEM was constructed using ABAQUS/CAE Version 6.9-EF for the cracked PWR outlet nozzle. The mesh included the same portions of the nozzle assembly as the uncracked 3-D FEM. A postulated $1/4t$ circular corner crack was included in the FEM, as shown in Figure 63.

The 3-D FEM for the PWR outlet nozzle with a postulated $1/4t$ circular corner crack was subjected to 1,000 psig internal pressure loading. Figure 64 displays K_I along the crack front from the RPV wall side of the crack ($\approx 0^\circ$ angle) to the nozzle inner surface side of the crack ($\approx 90^\circ$ angle). Similar results as those obtained for the other nozzles were observed for the PWR outlet nozzle: the lowest value of K_I occurs near the middle of the circular crack front; the magnification factor method solution results (the two points in Figure 64) are bounding compared with the actual and estimated 3-D FEM solutions at the deepest point of the $1/4t$ and $0.1t$ cracks, respectively; the magnification factor method solutions do not bound the maximum K_I values at the ends of the cracks; and, the deepest point magnification factor method solution for $1/4t$ flaw bounds the entire estimated crack front solution for a $0.1t$ flaw. Therefore, similar to the conclusions made for the nozzles, the conservatism of assuming a $1/4t$ flaw bounds the potential non-conservatism of evaluating the deepest point of the crack, and, as part of using the simplified magnification factor method solution, it is important to maintain the use of a large postulated flaw size. Any use of reduced flaw sizes need to be justified by appropriately considering the variation in K_I along the face of the crack as well as differences in flaw shape.

7. BWR Drill-Hole Style Instrument Nozzle

Similar stress and fracture mechanics analyses were conducted for a 2-inch diameter BWR drill-hole style instrument nozzle. The FEM was based on the RPV water level instrumentation nozzle for the James A. Fitzpatrick Nuclear Power Plant, which is a BWR-4 RPV with an internal diameter of 220 inches manufactured by CE for the General Electric Company. The geometry was taken from available drawings [14] with some corrections made to resolve some discrepancies in the specified dimensions, and is shown in Figure 65. An internal pressure loading case was analyzed with a detailed 3-D FEM of the instrument nozzle similar to the studies performed for the nozzles previously discussed in this report. Whereas the previously evaluated nozzles all used the rounded inner corner stress intensity factor solution defined by Equation (2), this nozzle configuration was evaluated using the sharp inner corner solution defined by Equation (3).

7.1 Uncracked BWR Instrument Nozzle Model

A 3-D FEM was constructed for the BWR instrument nozzle using 20-node brick elements. A symmetric one-quarter portion of the instrument nozzle was modeled, as shown in Figure 66. The FEM consists of portions of the RPV wall, the austenitic piping insert, the safe end, a portion of the attached pipe, the reinforcement on the outside surface of the RPV around the nozzle insert, cladding, and the J-groove weld material (shown in red in Figure 67) that connects the piping insert to the RPV wall. A radial clearance air gap of 0.005 inch was also included in the model between the RPV wall and the piping insert. Figure 67 illustrates the close-up view of the piping insert, safe end, reinforcement, cladding, and RPV wall. Appropriate boundary and loading conditions were applied to the 3-D FEM: symmetry boundary conditions were applied on both axial planes and the lower circumferential plane; a blow-off pressure membrane stress was applied to the far ends of the RPV wall and pipe; and 1,000 psig internal pressure was applied to all inner surfaces of the model. The material properties of the various components were obtained from Reference [14].

Figure 68 shows the pressure stress intensity profile for the uncracked 3-D FEM subjected to 1,000 psig internal pressure loading. The maximum stress in the entire FEM occurs in the air gap due to the presence of a singularity caused by the modeling of the air gap. After removal of this fictitious singularity, the maximum pressure stress in the model occurs in the nozzle corner vessel axial plane, and the pressure stress varies around the nozzle circumference, as shown in Figure 69. The peak pressure hoop stress in the nozzle material in the uncracked 3-D FEM is 63,800 psi (calculated the peak SINT of 64,800 psi from Figure 69 minus the radial pressure stress of 1,000 psi). The nominal pressure hoop

stress in the RPV wall is $PR/t = 18,734$ psi. Therefore, the SCF for the BWR instrument nozzle is 3.5 (calculated as $64,800/18,734$).

The pressure hoop stresses were extracted from the uncracked nozzle FEM along a path that starts from the inside corner of the nozzle along a 45° angle, passing through weld material, and ends at the outside surface of the RPV wall, as shown in Figure 70. Figure 71 shows the extracted pressure hoop stresses along the selected path, and the pressure stress distribution approximated by a third-order polynomial.

7.2 BWR Instrument Nozzle Model with a 3-D Simulated Circular Corner Crack

A 3-D FEM was constructed using ABAQUS/CAE Version 6.9-EF for the cracked BWR instrument nozzle. The mesh includes the same portions of the nozzle assembly as the uncracked 3-D FEM. A postulated $1/4t$ circular corner crack was included in the FEM, as shown in Figure 72.

The 3-D FEM for the BWR instrument nozzle with a postulated $1/4t$ circular corner crack was subjected to 1,000 psig internal pressure loading. Figure 73 displays K_I along the crack front from the RPV wall side of the crack ($\approx 0^\circ$ angle) to the air gap adjacent to the nozzle ($\approx 90^\circ$ angle). Equation (3) for the postulated circular nozzle corner crack with a 90° sharp corner was utilized for the magnification factor method solution. Similar results as those for the other nozzles were observed: the lowest value of K_I occurs near the deepest point of the circular crack front; the magnification factor method solution results (the two points in Figure 73) are bounding compared with the 3-D finite element solution at the corresponding location of the $1/4t$ and $0.1t$ cracks, respectively; the magnification factor method solutions do not bound the maximum K_I values at the ends of the cracks; the deepest point magnification factor method solution for $1/4t$ flaw bounds the entire estimated crack front solution for a $0.1t$ flaw. Therefore, similar to the conclusions made for the other nozzles evaluated in this report, the conservatism of assuming a $1/4t$ flaw bounds the potential non-conservatism of evaluating only the deepest point of the crack, and, as part of using the simplified magnification factor method solution, it is important to maintain the use of a large postulated flaw size. Any use of reduced flaw sizes need to be justified by appropriately considering the variation in K_I along the face of the crack as well as differences in flaw shape.

8. Summary and Conclusions

The analyses documented in this report were performed to support an investigation of 10CFR50 Appendix G [4]. The primary motivation for this work was to gain a more thorough understanding of nozzle stress and fracture mechanics solutions so that they can be integrated into pressure-temperature (P-T) limit evaluations, especially for those nozzle configurations adjacent to the active core where radiation effects are significant. This report provides a summary of detailed stress and fracture mechanics analyses performed on both BWR and PWR nozzles and the corresponding results of these investigations. Five nozzle configurations were selected for evaluation.

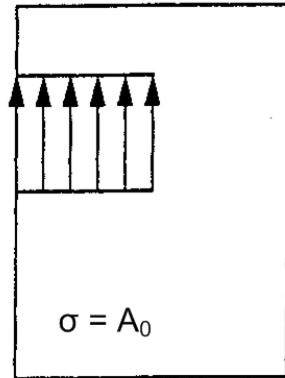
The following summarizes results of the nozzle stress and fracture mechanics evaluations:

- Using the BWR RO nozzle as an example, the capabilities of axisymmetric 2-D FEMs were investigated and compared with detailed 3-D FEMs for internal pressure loading with the following findings:
 - A peak stress correction factor of 3.1 (as applied to RPV hoop stress remote from discontinuities) was obtained for 1,000 psig internal loading, which compares well with the stress index for hoop stress of 3.1 in Section III of the ASME Code [10], and reasonably well with the bounding value of 3.0 suggested in Reference [7].
 - The 3-D FEM results indicate that the pressure stress varies significantly around the nozzle circumference as a result of the ovalization effect of the nozzle cylindrical geometry with the cylindrical RPV. Therefore, appropriate magnification of 2-D axisymmetric results is required to compensate for stress inaccuracies if 2-D FEMs are used for the analysis.
- Using the BWR RO and CS nozzles as examples, the capabilities of axisymmetric 2-D FEMs were investigated and compared with detailed 3-D FEMs for thermal loading (both ramped and shock loading). There is no significant variation between the 2-D and 3-D results with respect to thermal stresses in the nozzle corner region. In addition, thermal stresses do not vary significantly around the nozzle circumference. Generally, the use of a 2-D FEM provides bounding thermal stress results compared to 3-D FEMs. Therefore, 2-D FEMs are considered appropriate for use in estimating thermal stresses in nozzle corner regions without the need for correction.

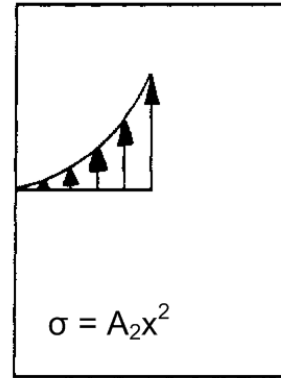
- Using the BWR RO nozzle as an example, the variation in stress intensity factors for varying flaw shapes was investigated. The stress intensity factors along the crack front for a $0.1t$ circular nozzle corner crack were compared to the stress intensity factors along the crack front for a $0.1t$ semi-elliptical nozzle corner crack with an aspect ratio of 6:1 (length-to-depth). The results indicate that the flaw geometry significantly affects the K_I profile along the crack front. The highest value of K_I occurs near the center of the crack front for the semi-elliptical corner crack, while the lowest K_I occurs near the center of the crack front for the circular corner crack. At the center of the crack front, the K_I for a $0.1t$ semi-elliptical corner crack is higher than the K_I for a $0.1t$ circular corner crack. These results indicate that the use of the circular corner crack model is conservative coupled with the assumption of a postulated $1/4t$ crack. Consideration of smaller flaw sizes should also address different flaw shapes. Using the BWR RO nozzle as an example, it was demonstrated that attached piping loads do not contribute significantly to the stresses in the nozzle corner region. Coupled with the use of a large ($1/4t$) postulated flaw size, these loads may be neglected from evaluations meant to establish RPV P-T limits. However, if flaw sizes smaller than $1/4t$ are used, these loads should be factored into the analysis.
- Using BWR RO nozzle as an example, it was demonstrated that applying pressure on the postulated crack face does not contribute significantly to the crack tip stress intensity factor in the nozzle corner region. Coupled with the use of a large ($1/4t$) postulated flaw size, this load may be neglected for evaluation when establishing RPV P-T limits. However, if flaw sizes smaller than $1/4t$ are used, these loads should be factored into the analysis.
- Stress intensity factors, K_I , were calculated from simplified magnification factor method solutions obtained from the literature [3, 5, 7] and compared to LEM solutions obtained from 3-D FEMs with postulated $1/4t$ circular corner cracks subjected to internal pressure loading, ramped cool-down thermal loading, and shock thermal loading. The magnification factor method solutions were verified to be reasonable and bounding with respect to estimating stress intensity factors if coupled with the use of a large ($1/4t$) postulated flaw size for combined pressure and thermal loading. If smaller flaw sizes are used, these solutions may not provide bounding estimates of stress intensity factors for circular cracks because they estimate K_I at the deepest point of the flaw instead of at the ends of the flaw where the analyses indicate that K_I is a maximum. Therefore, refined magnification factor method solutions or finite element analysis should be used if postulated flaw sizes smaller than $1/4t$ are considered, or if other flaw shapes are considered.

These results support the following two conclusions:

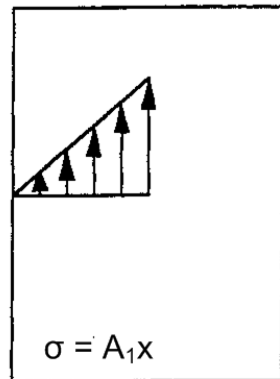
- The simplified closed-form LEM solutions presented in Chapter 2 of this report for postulated circular nozzle corner cracks may be considered as part of future revisions of Paragraph G-2223, Nonmandatory Appendix G of ASME Code Section XI along with the use of a $1/4t$ postulated flaw size for establishing RPV P-T limits.
- Peak stress correction factors of 2.7, 2.9, 3.4, and 3.5 (as applied to RPV pressure hoop stress remote from discontinuities) were obtained for 1,000 psig internal pressure loading for the BWR CS nozzle, the PWR inlet nozzle, the PWR outlet nozzle, and the BWR instrumentation nozzle, respectively. Coupled with the results for the RO nozzle, a bounding SCF value of 3.1, which agrees well with the stress index for hoop stress of 3.1 in Section III, Table NB-3338.2(c)-1 of the ASME Code, is appropriate for use in lieu of 3-D finite element analysis to account for corner effects on pressure stress for all nozzles with traditional forgings with rounded inside corners, such as the BWR RO nozzle, the BWR CS nozzle, and the PWR inlet nozzle. A bounding SCF value of 3.5 is more appropriate for use for nozzles with special discontinuities or sharp inside corners, such as the PWR outlet nozzle and the BWR instrument nozzle.



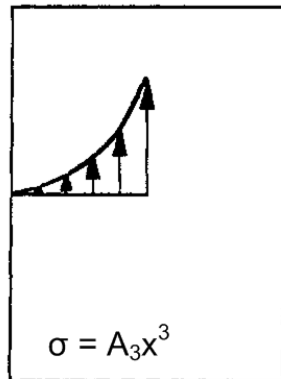
(a) $K_I = K_{I0}$



(c) $K_I = K_{I2}$



(b) $K_I = K_{I1}$



(d) $K_I = K_{I3}$

Figure 1. Stress Intensity Magnification Factors Method

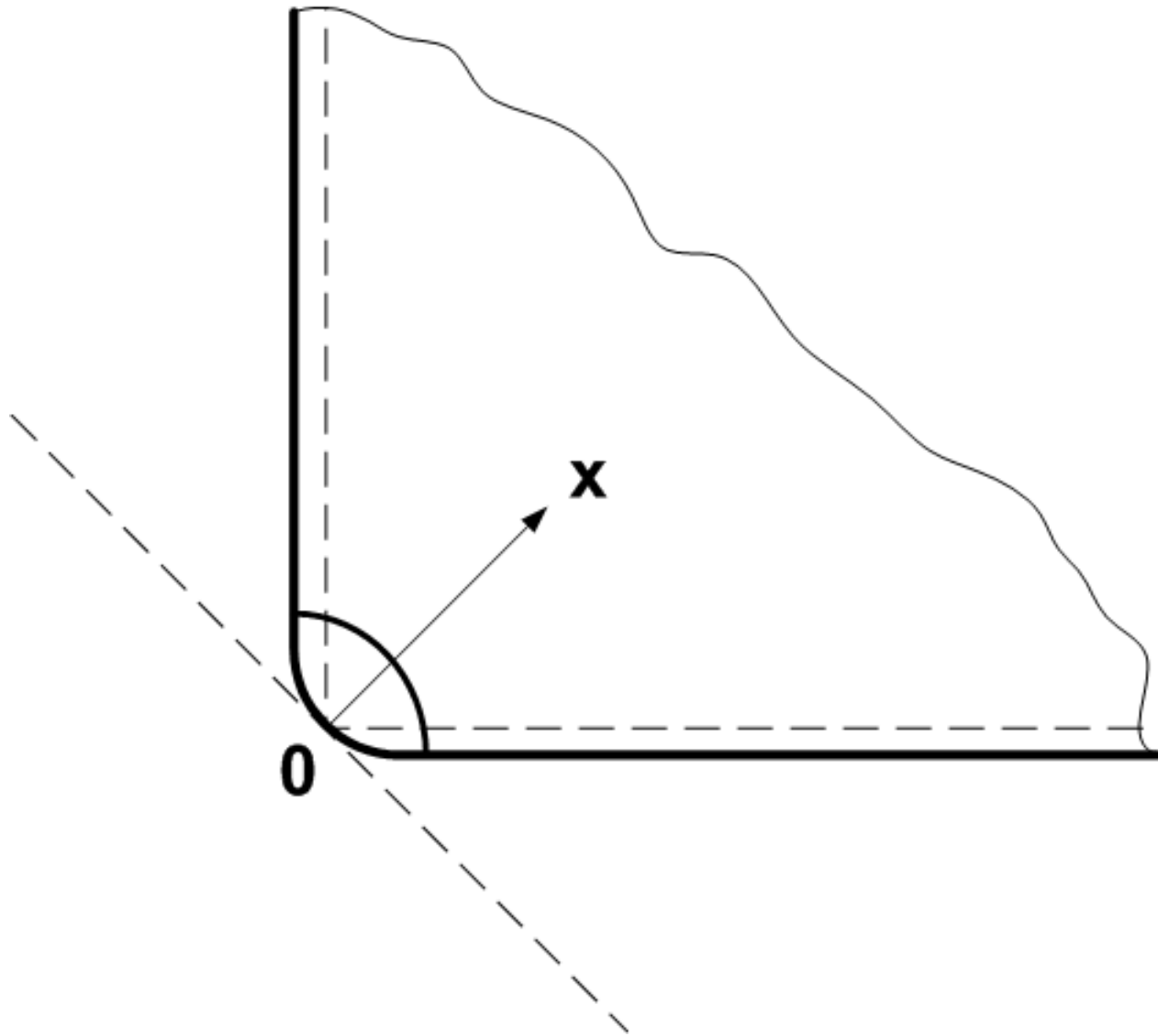


Figure 2. Postulated Circular Nozzle Corner Crack for a Nozzle with a Rounded Corner

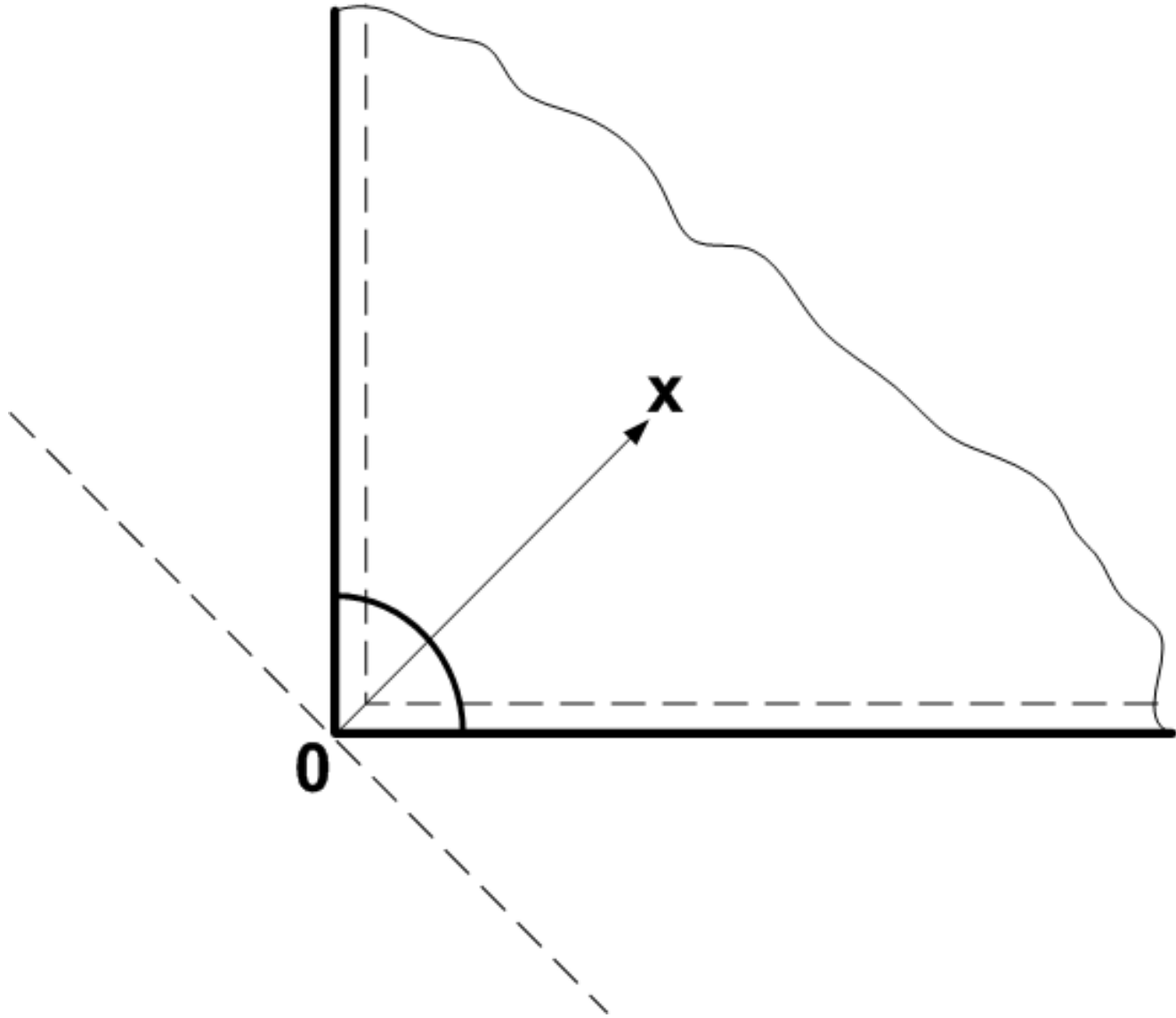


Figure 3. Postulated Circular Nozzle Corner Crack for a Nozzle with Sharp 90° Corner

Assume the center line is ZERO in Y-axis, and number 9.88 is correct, then the red point $Y = 28.88/2 + 7 * (1 - \cos(45^\circ)) + (9.88 - 7 * \sin(45^\circ)) / \cos(45^\circ) * \sin(45^\circ) = 21.420505$, While in the plot, $Y = 48.75/2 = 24.375$.

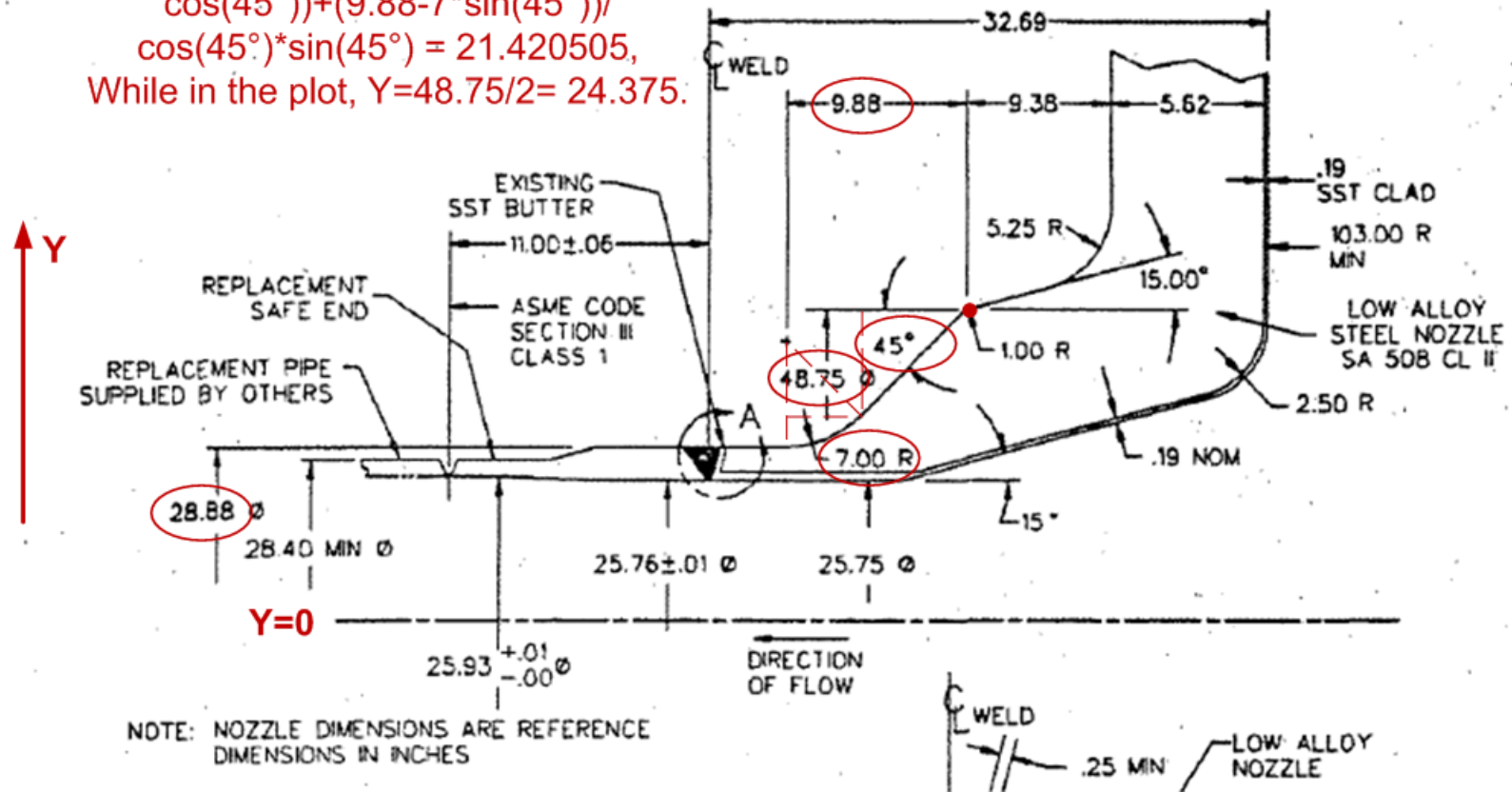


Figure 4. BWR RO Nozzle and Safe End Geometry (from Figure 3 of Reference [6])

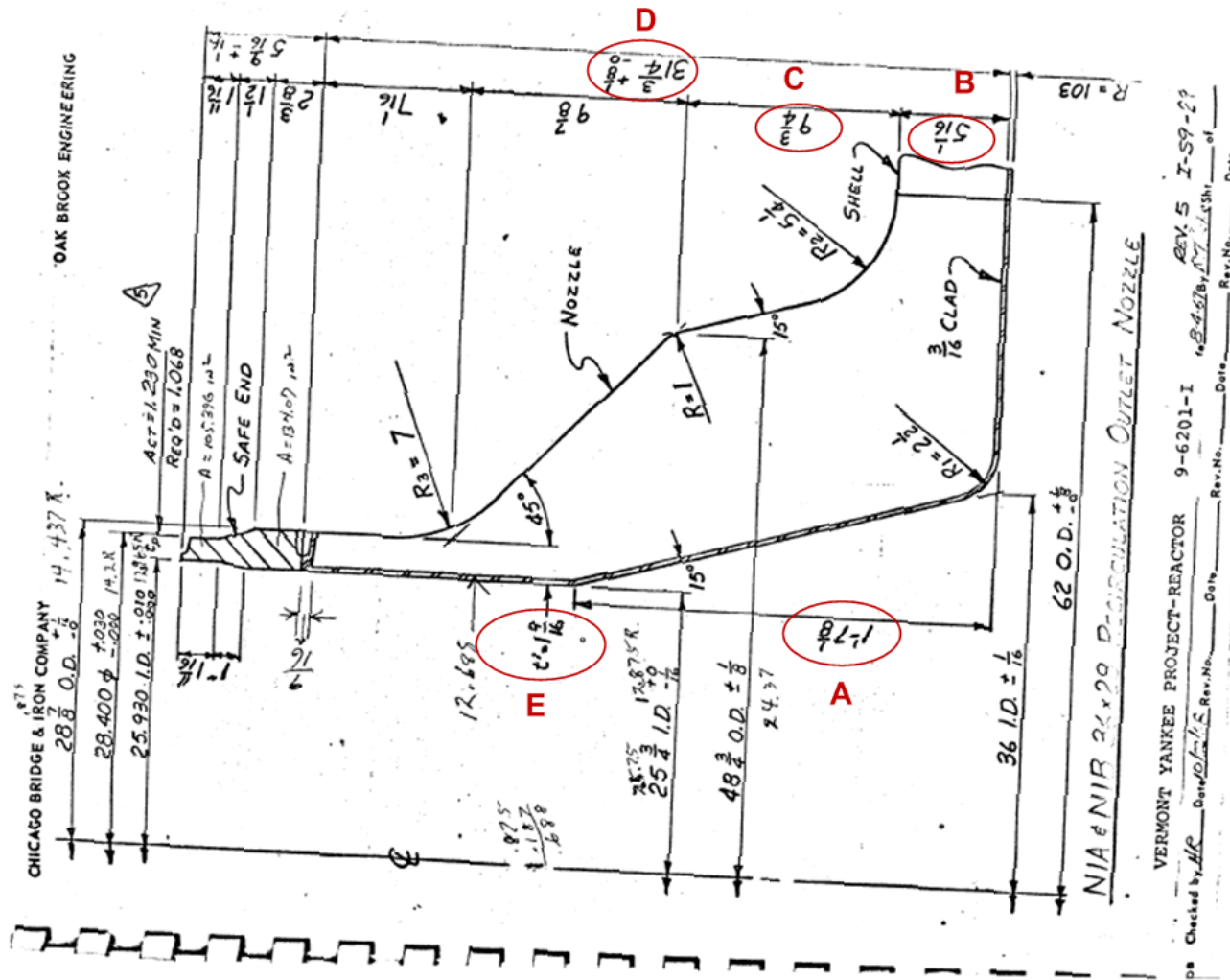


Figure 5. BWR RO Nozzle and Safe End Geometry (from Reference 5 of Reference [6])

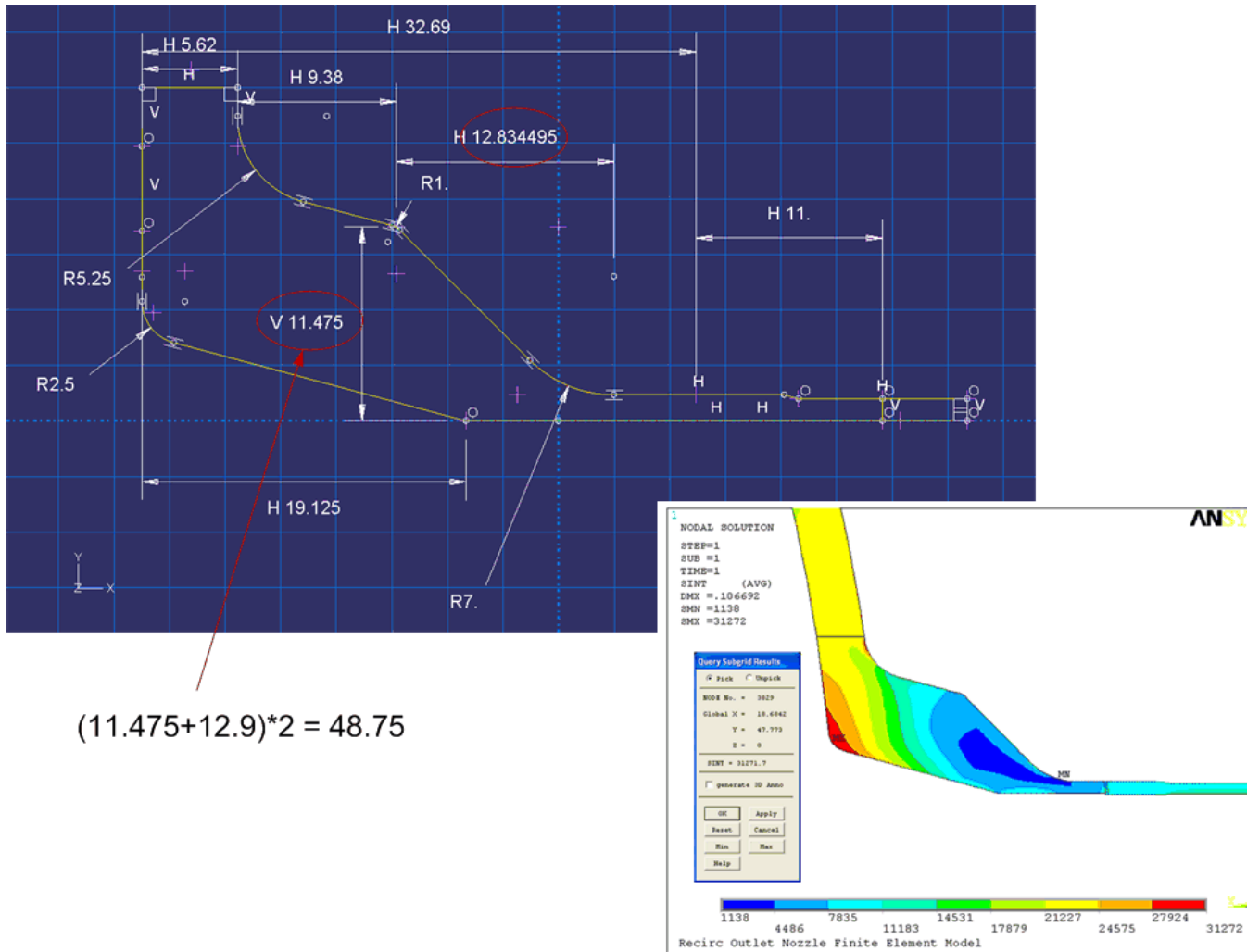


Figure 6. BWR RO Nozzle Geometry Used in the RO Nozzle FEM

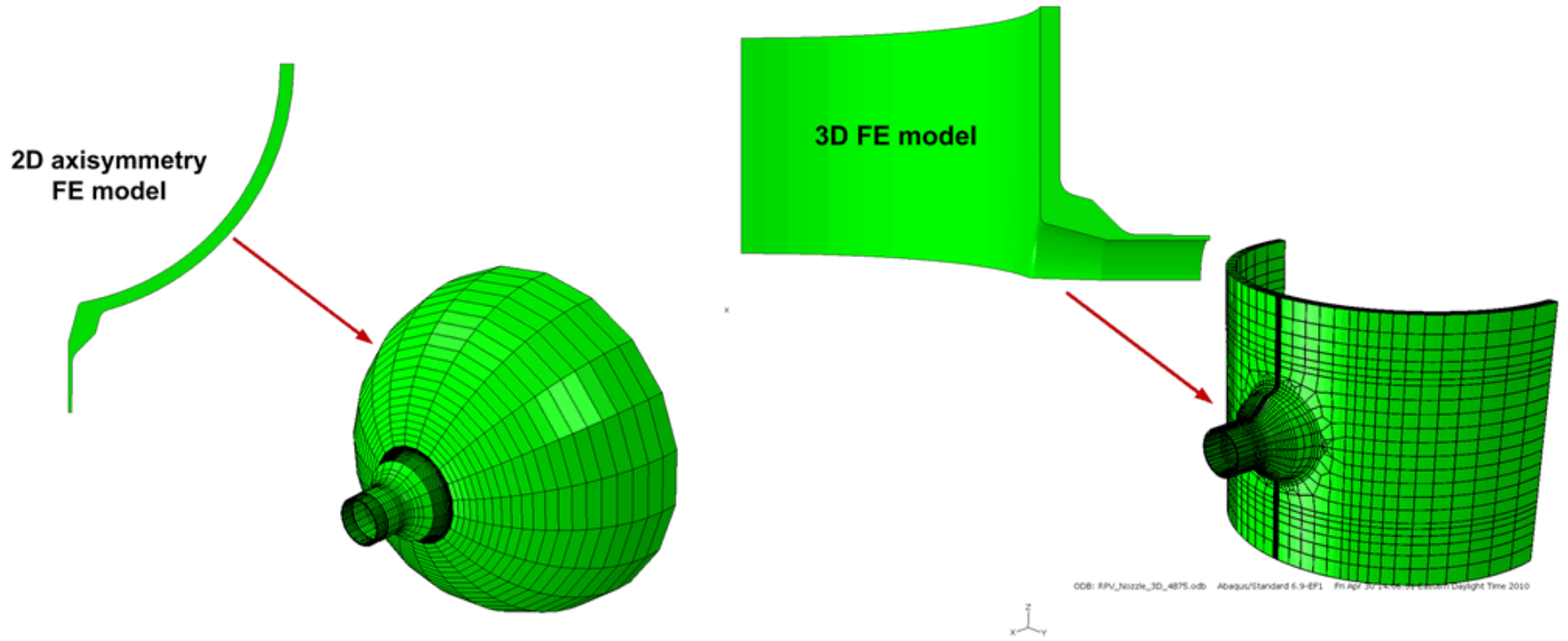


Figure 7. 2-D and 3-D FEMs for the BWR RO Nozzle

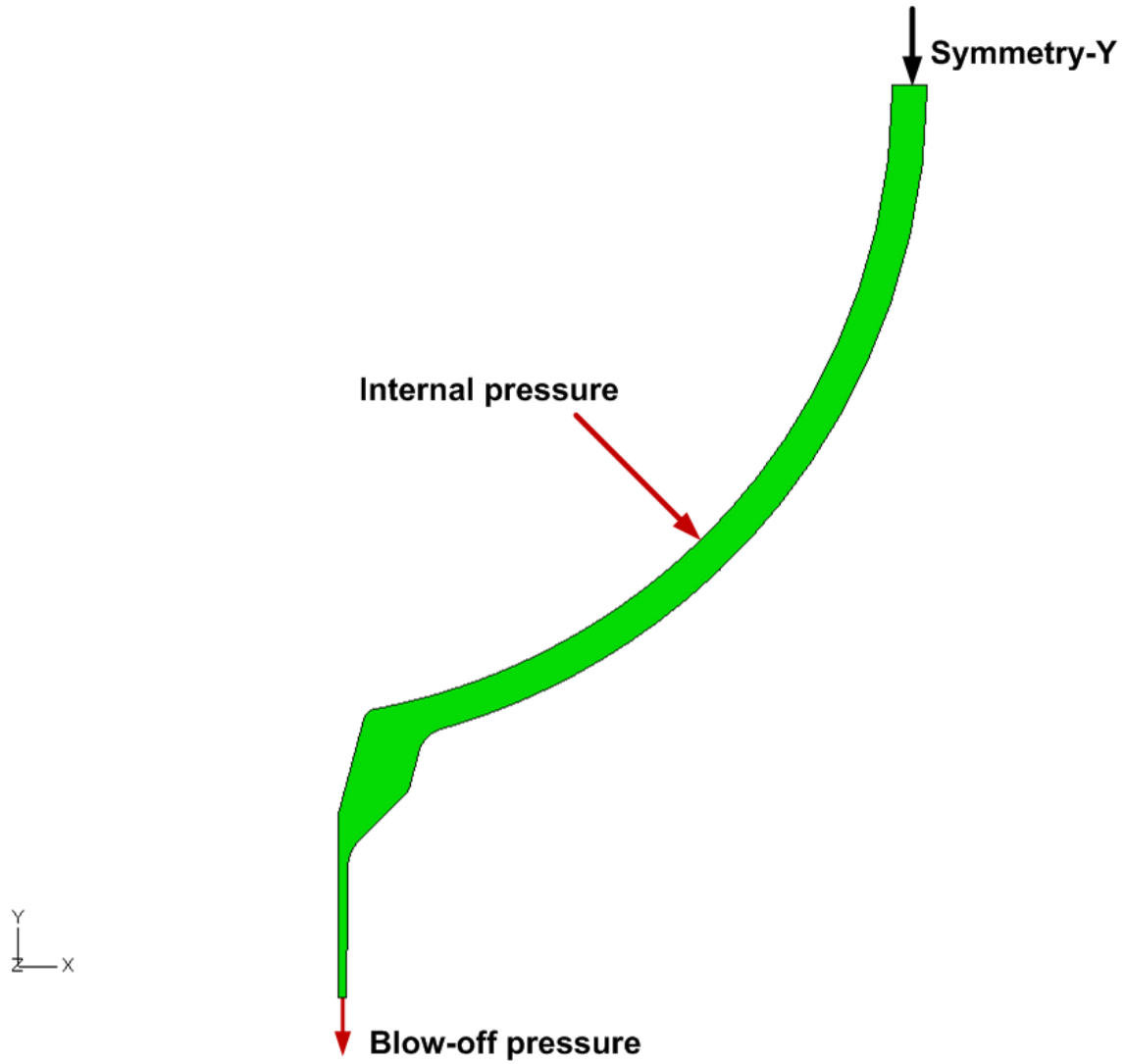
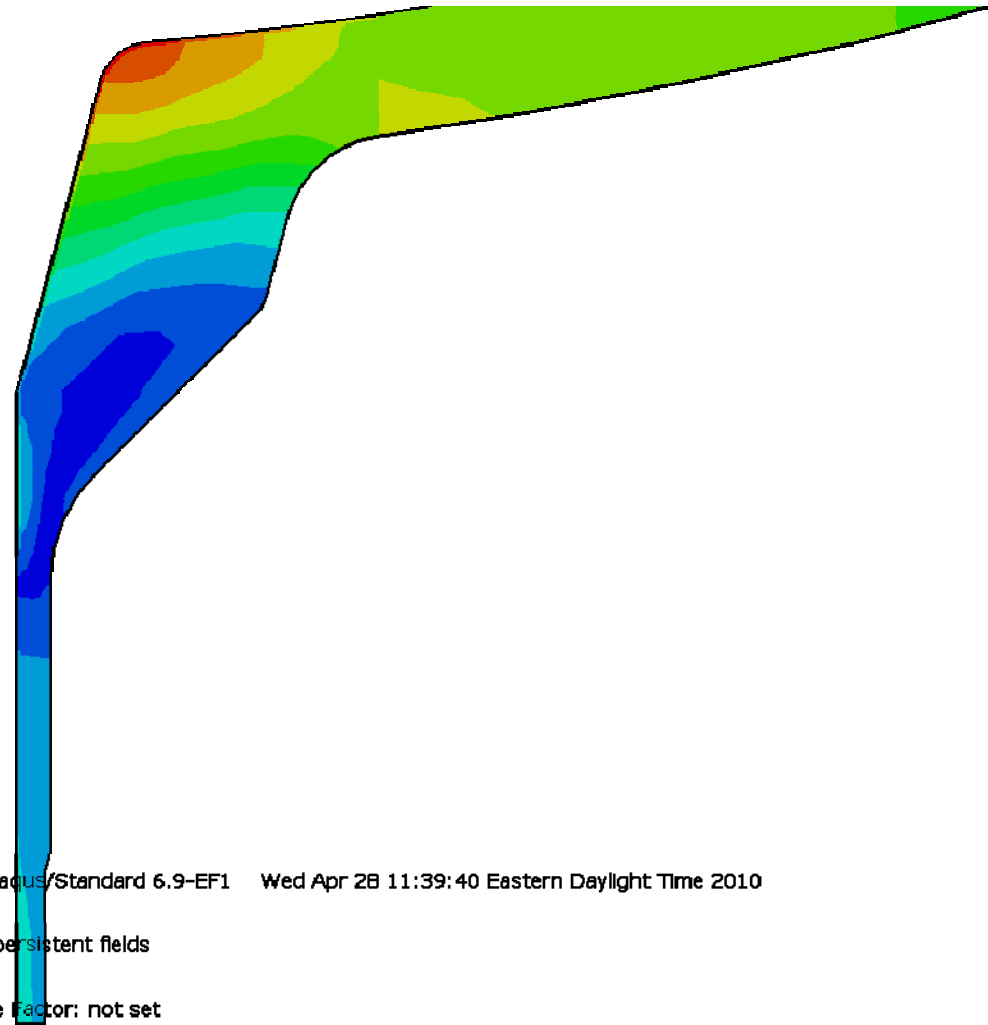
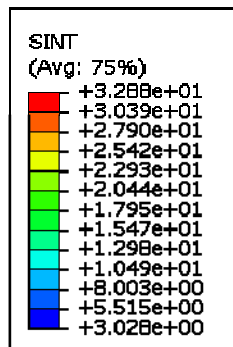


Figure 8. Boundary and Loading Conditions for the 2-D BWR RO Nozzle FEMs



ODB: RPV_Nozzle_2D_4875_2R.odb Abaqus/Standard 6.9-EF1 Wed Apr 28 11:39:40 Eastern Daylight Time 2010

Step: Session Step, Step for Viewer non-persistent fields
 Session Frame
 Primary Var: SINT
 Deformed Var: not set Deformation Scale Factor: not set

Figure 9. Results for BWR RO Nozzle 2-D (RPV Radius = 2R) FEM (Maximum SINT for P = 1,000 psig pressure loading = 32,880 psi)

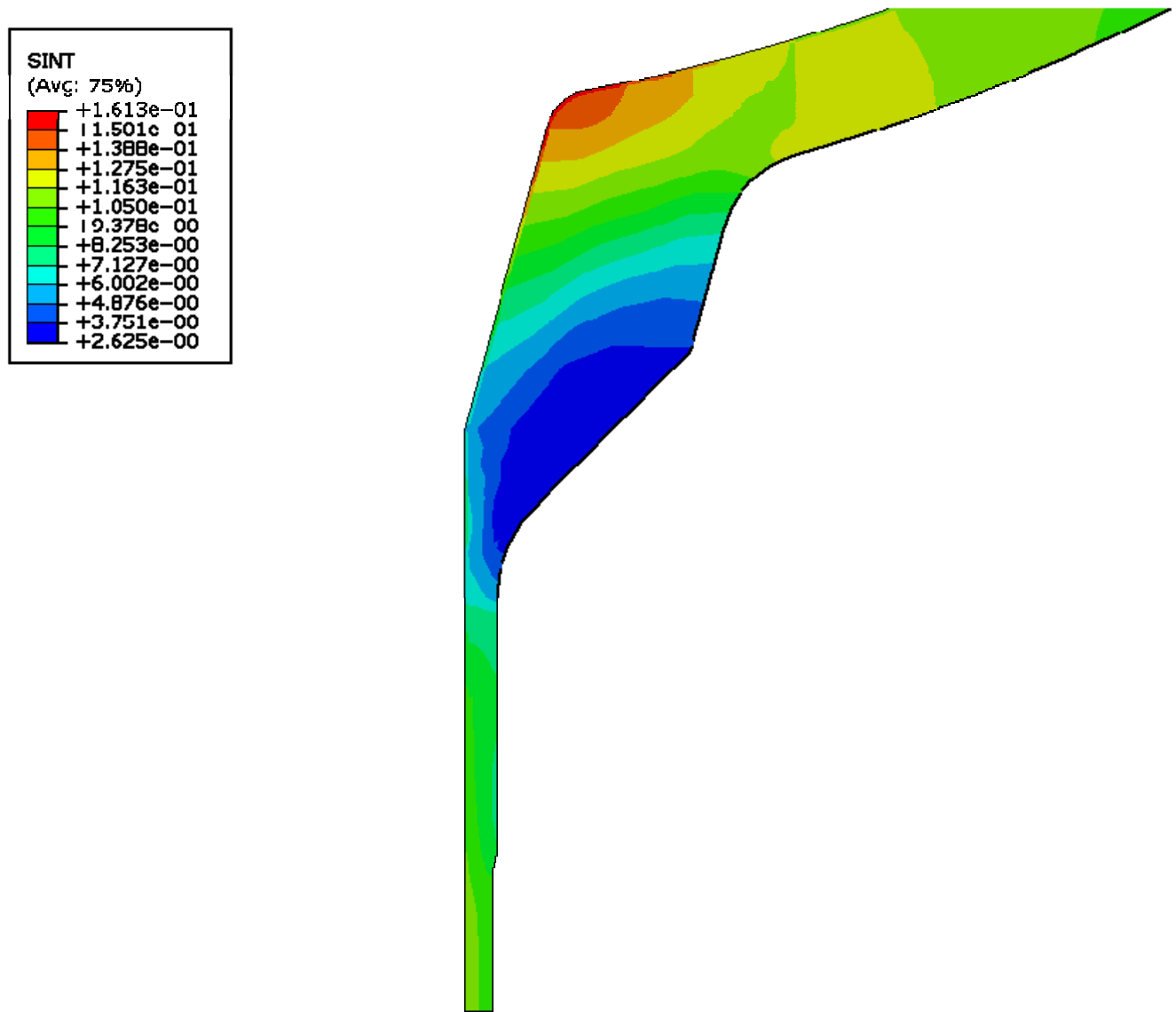


Figure 10. Results for BWR RO Nozzle 2-D (RPV Radius = R) FEM (Maximum SINT for P = 1,000 psig pressure loading = 16,130 psi)

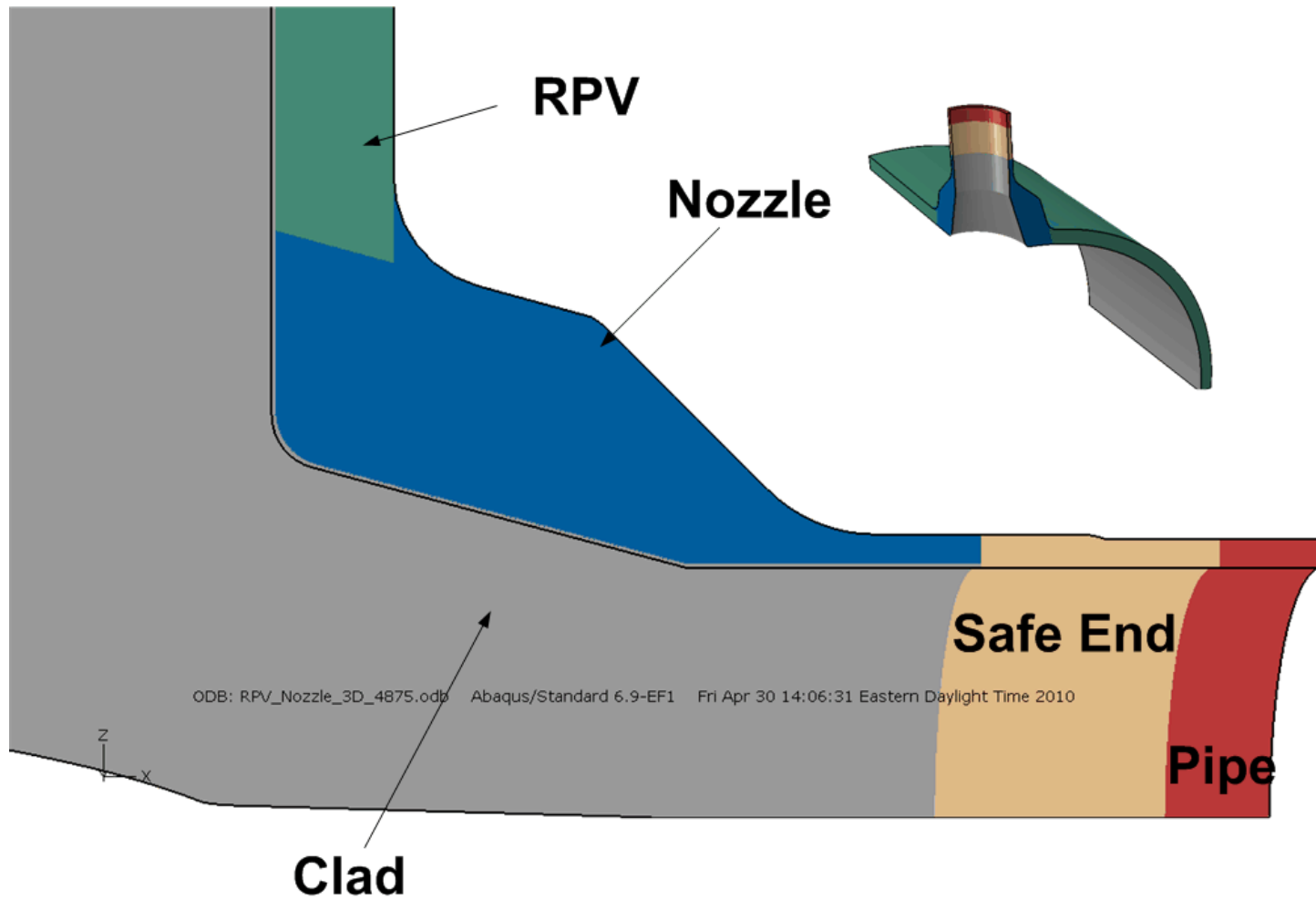


Figure 11. Portions Included in 3-D BWR RO Nozzle FEM

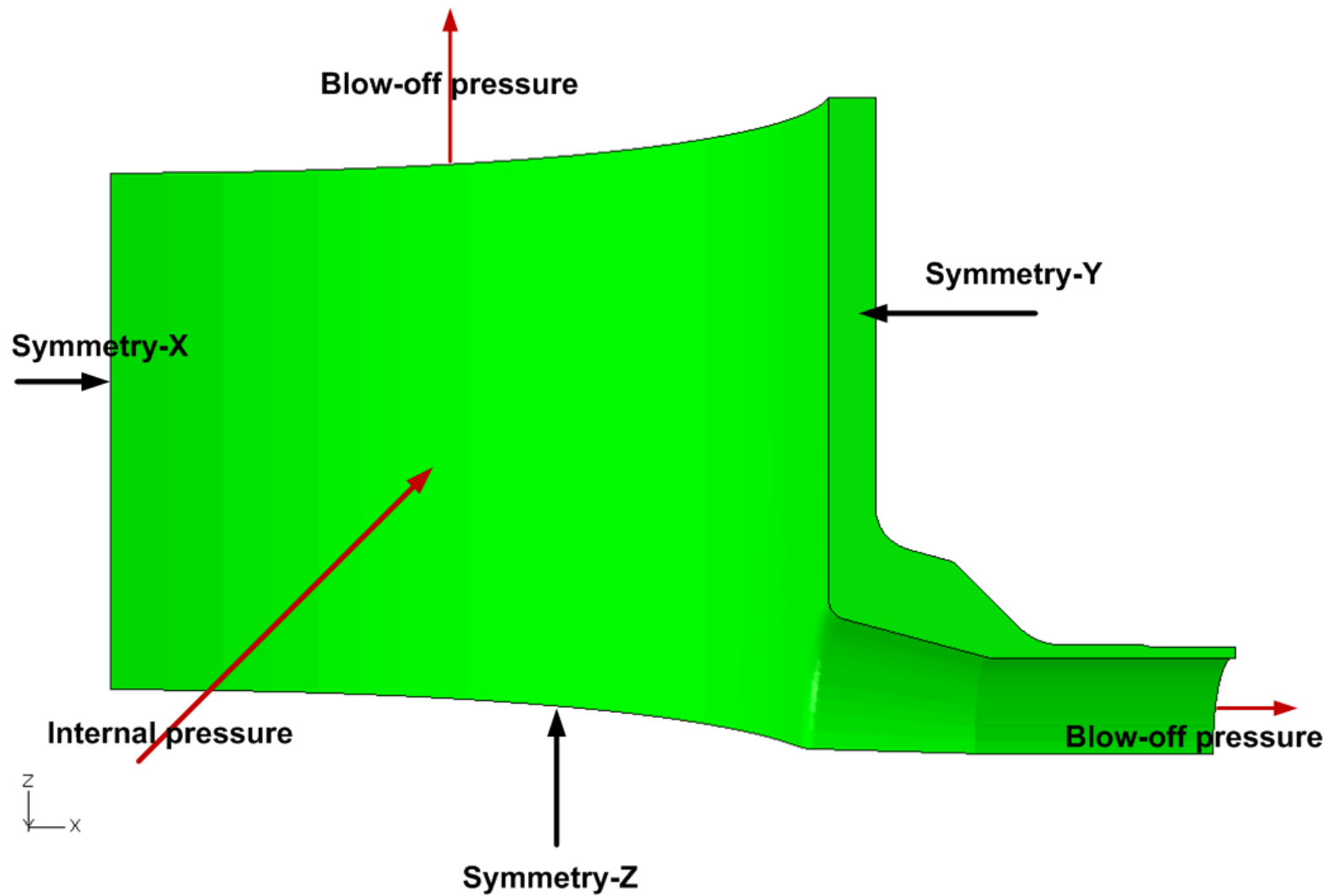


Figure 12. Boundary and Loading Conditions Applied in 3-D BWR RO Nozzle FEM

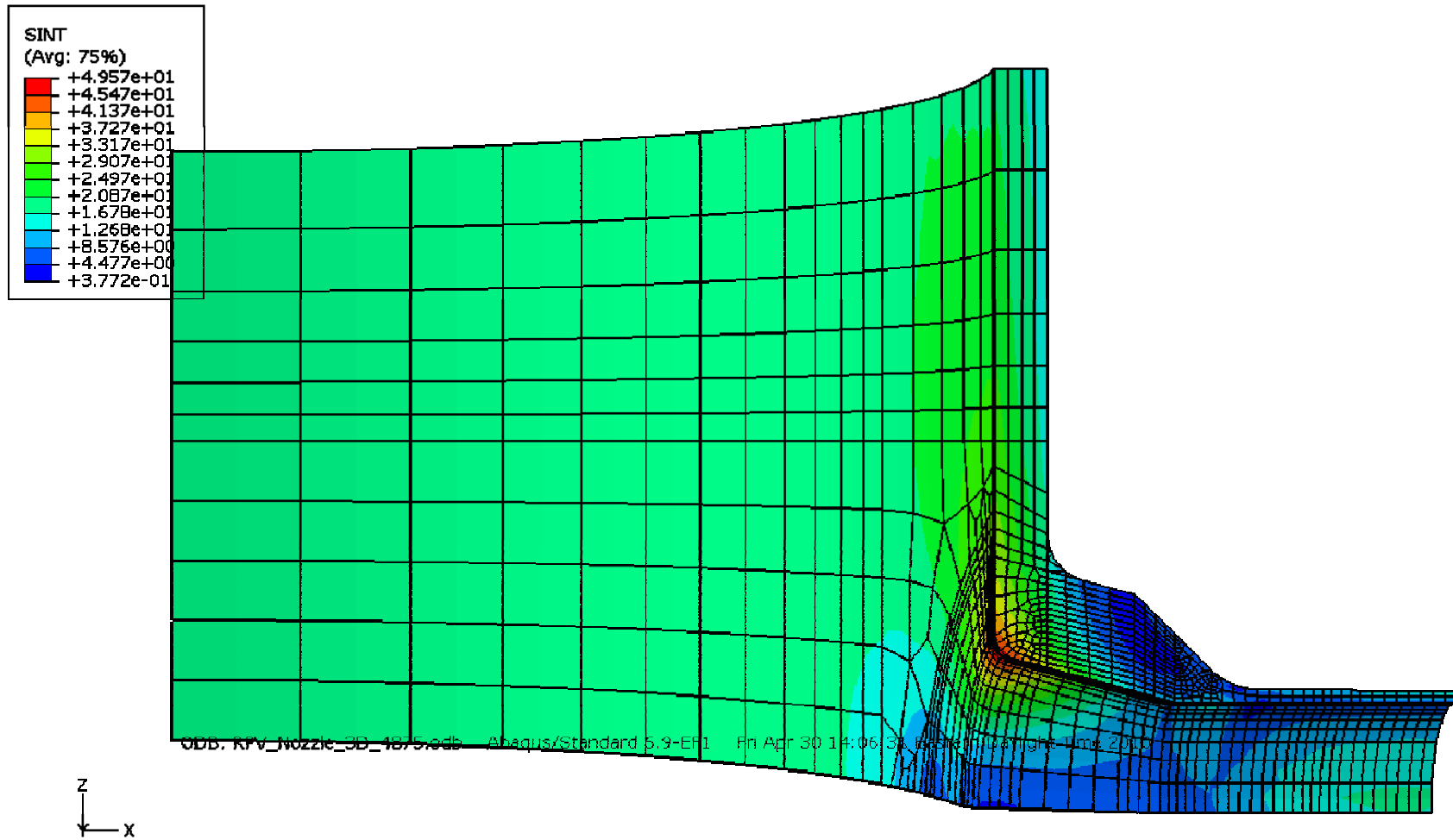


Figure 13. Results for BWR RO Nozzle 3-D FEM Maximum SINT for P = 1,000 psig pressure loading = 49,570 psi)

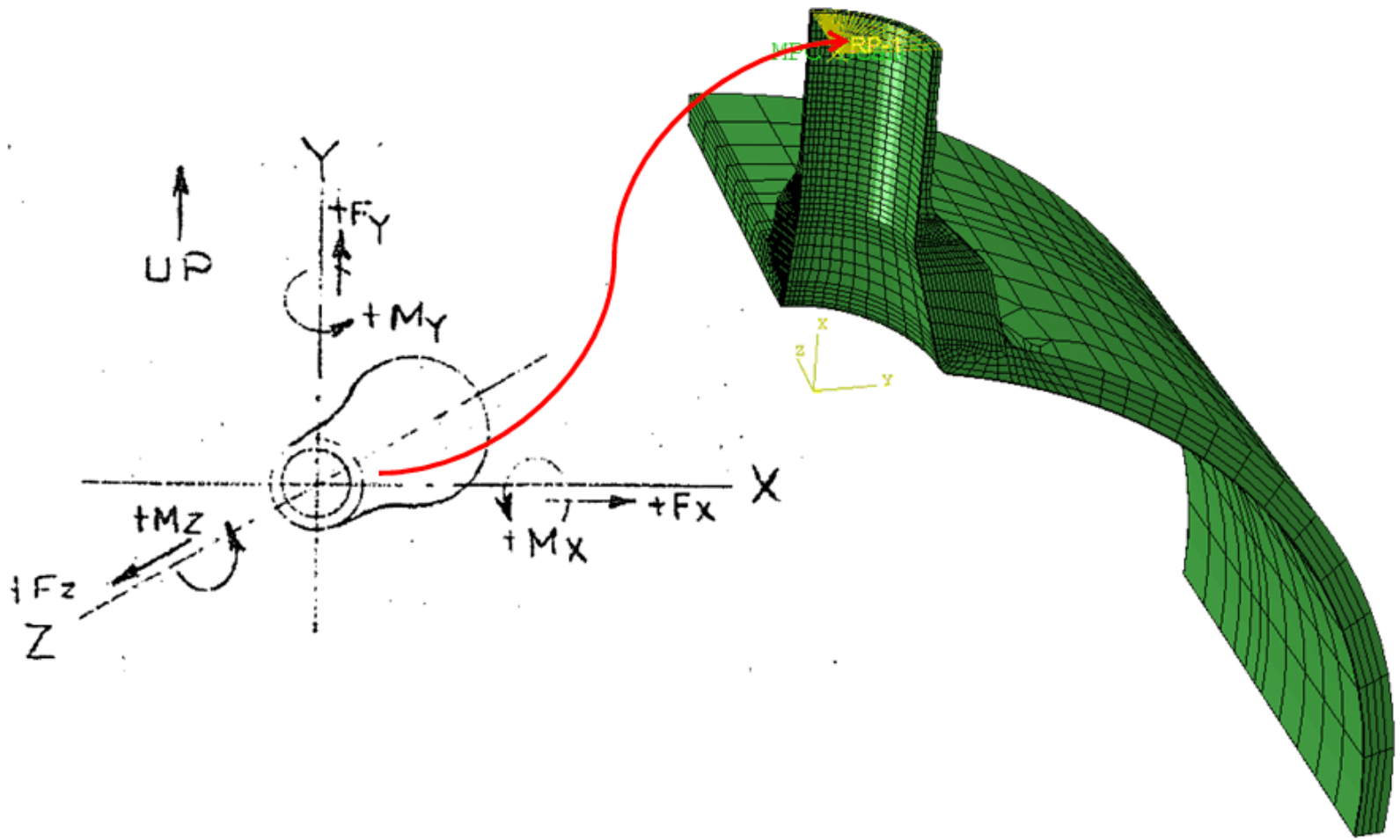


Figure 14. Piping Interface Loads Applied to the BWR RO Nozzle 3-D FEM

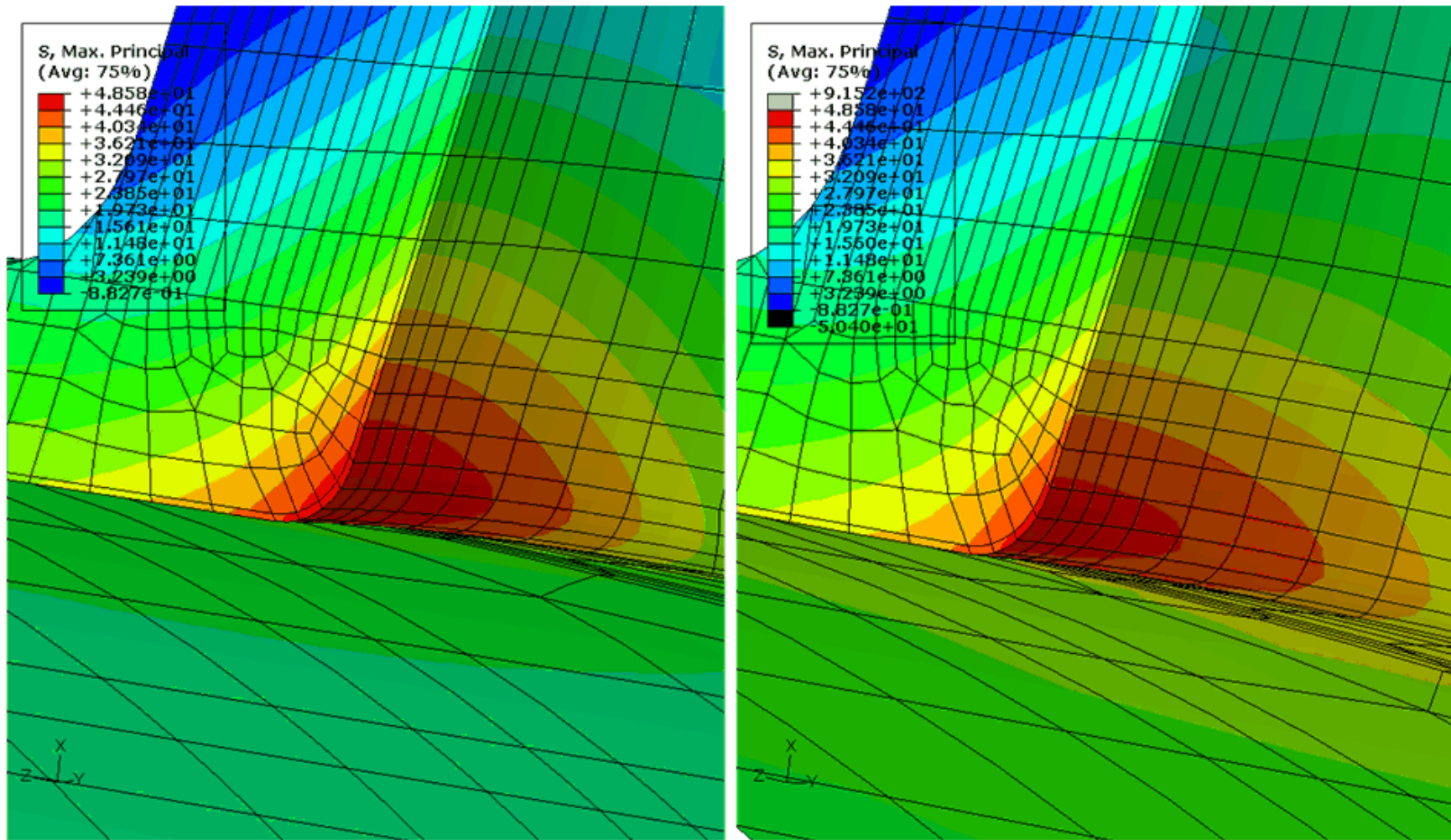


Figure 15. Maximum Principal Stress in BWR RO Nozzle Due to Pressure Load Only (left) and Pressure Plus Attached Piping Loads (right)

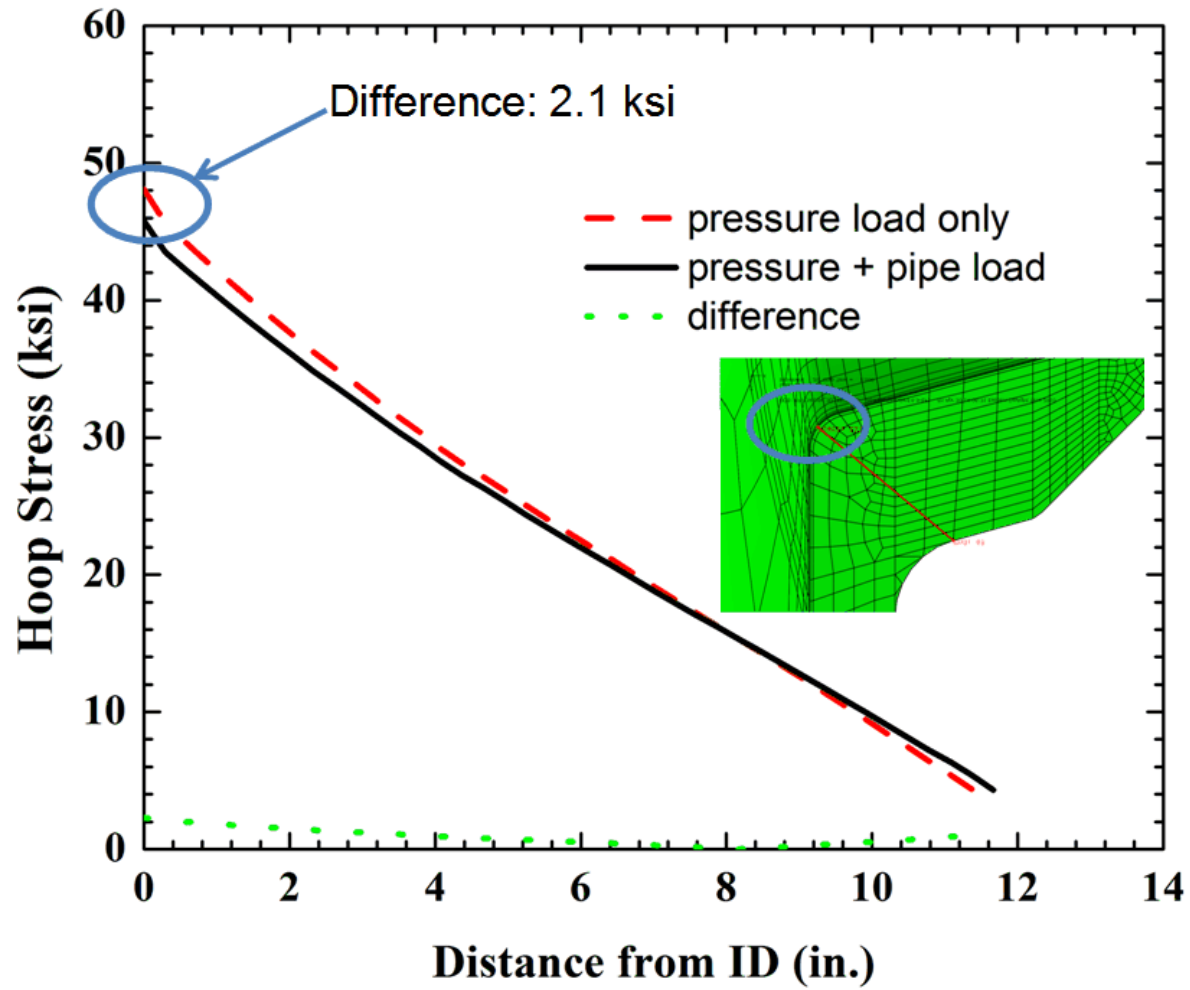


Figure 16. Comparison of Hoop Stress in BWR RO Nozzle Due to Pressure Load only and Pressure Plus Piping Loads

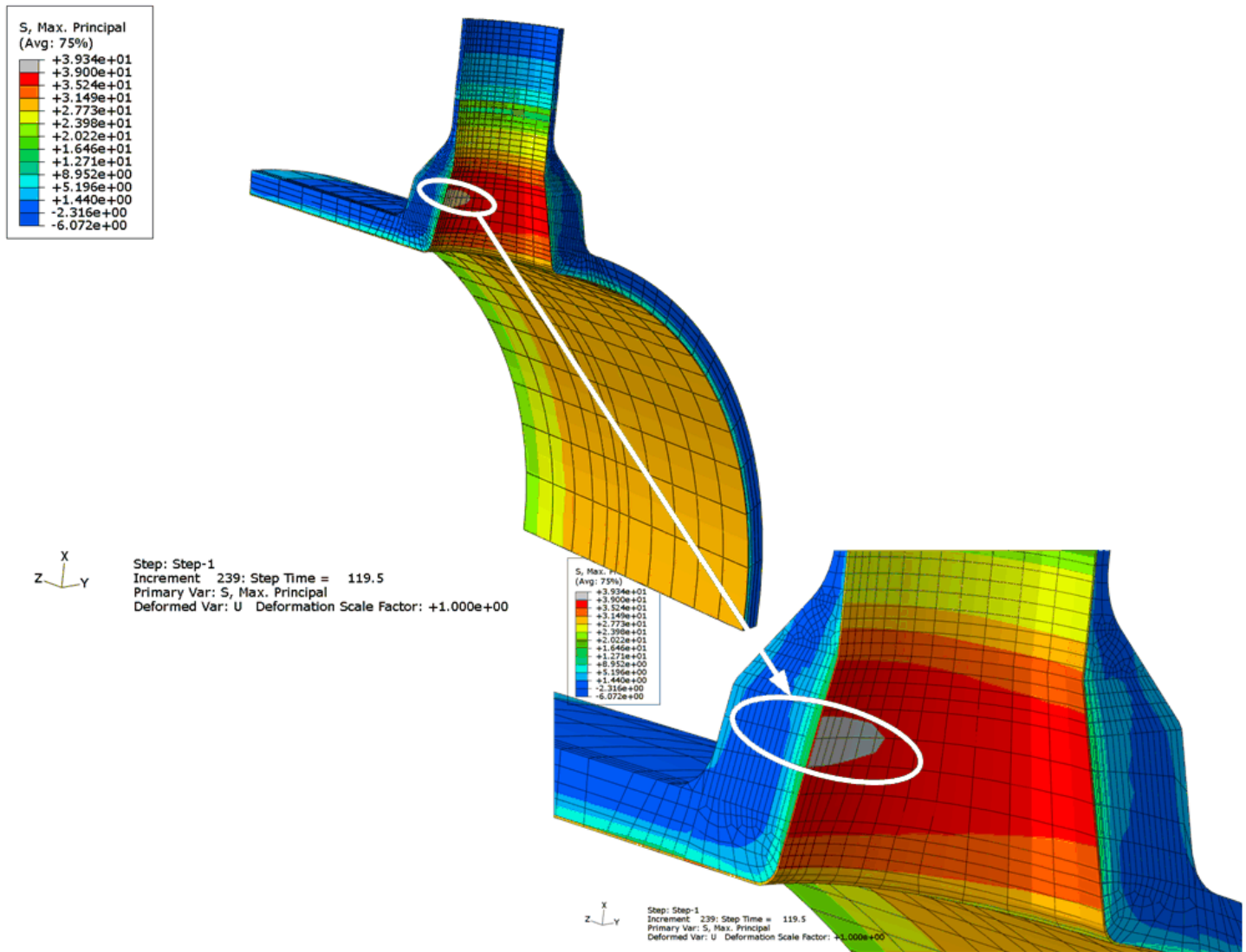


Figure 17. Maximum Principal Stress for the BWR RO Nozzle 3-D FEM Subjected to a Cool-down Transient

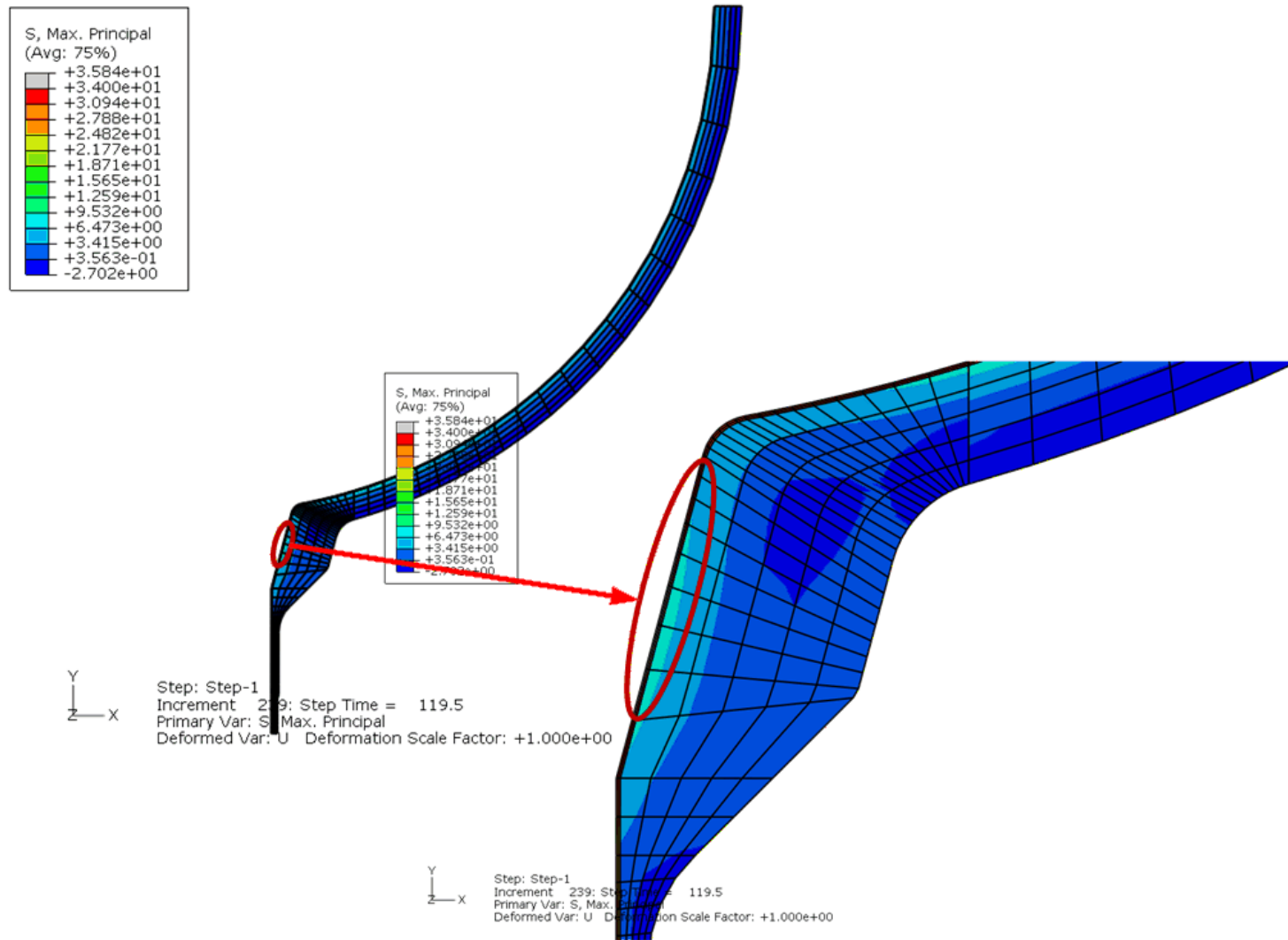


Figure 18. Maximum Principal Stress for the BWR RO Nozzle 2-D FEM Subjected to a Cool-down Transient

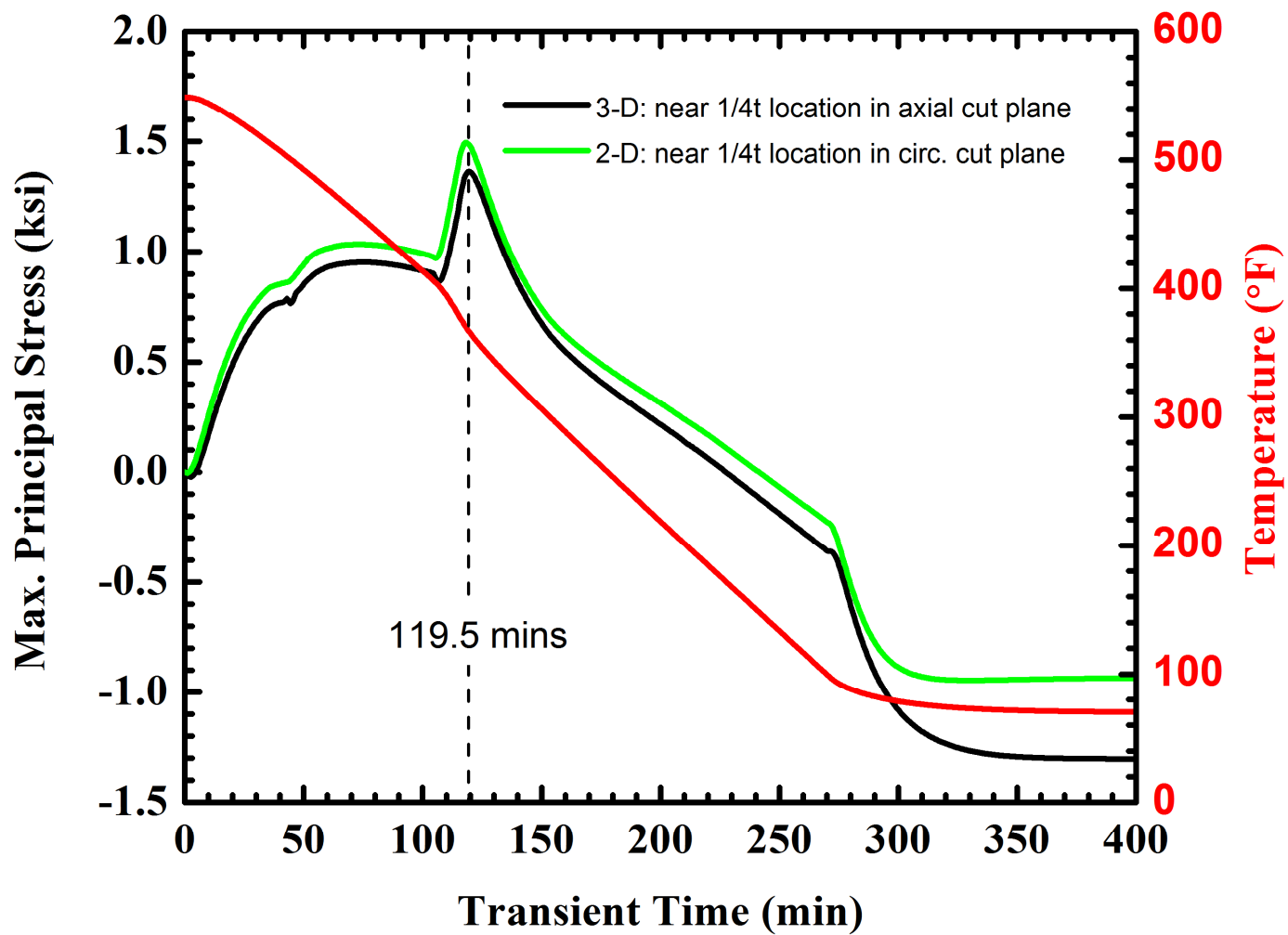


Figure 19. Maximum Principal Stress for the BWR RO Nozzle During a Cool-down Thermal Transient (at the $\frac{1}{4}t$ location along a 45° path through the nozzle corner)

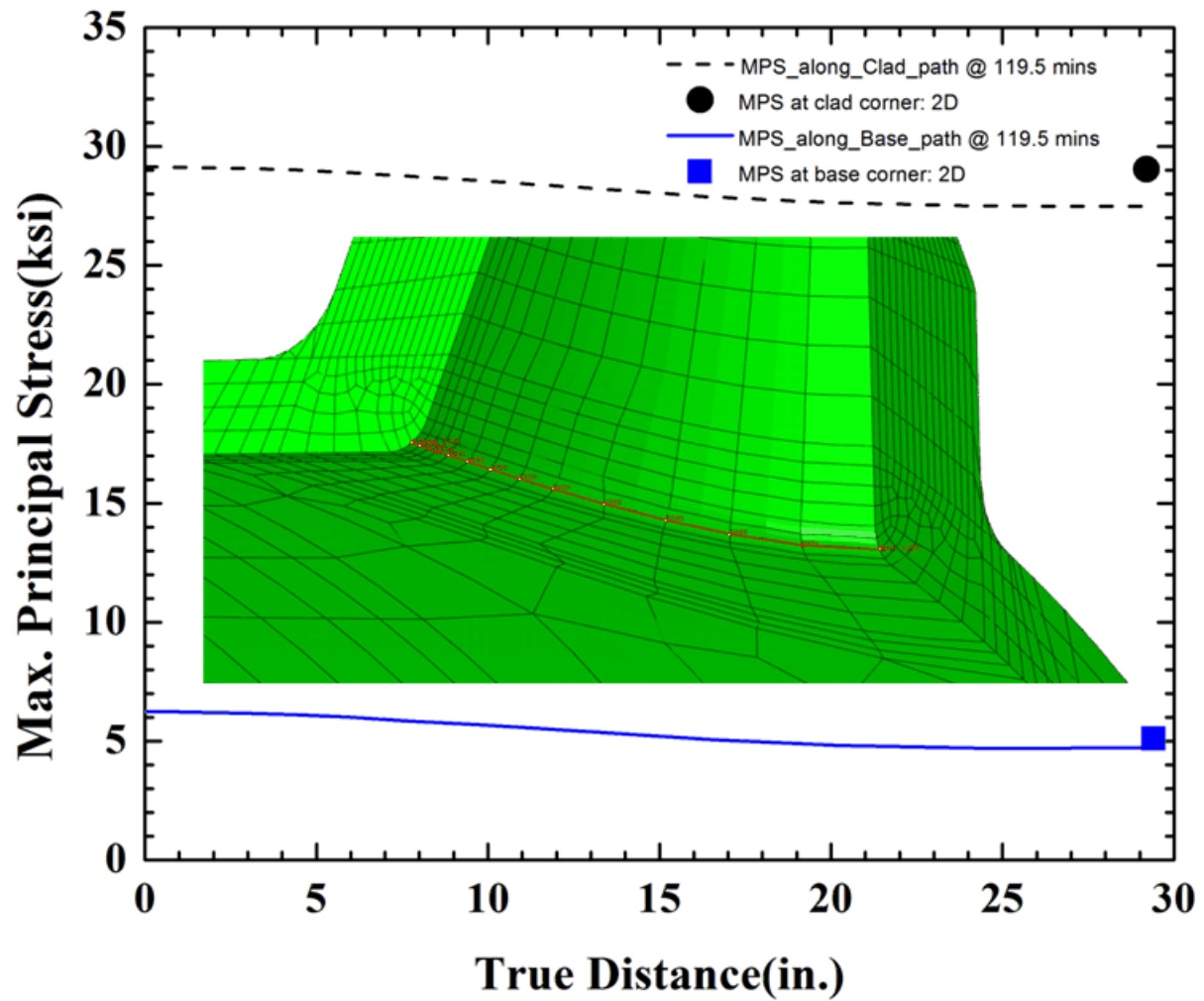


Figure 20. Maximum Principal Stress for the BWR RO Nozzle Around the Nozzle Circumference for a Cool-down Transient (t = 119.5 minutes)

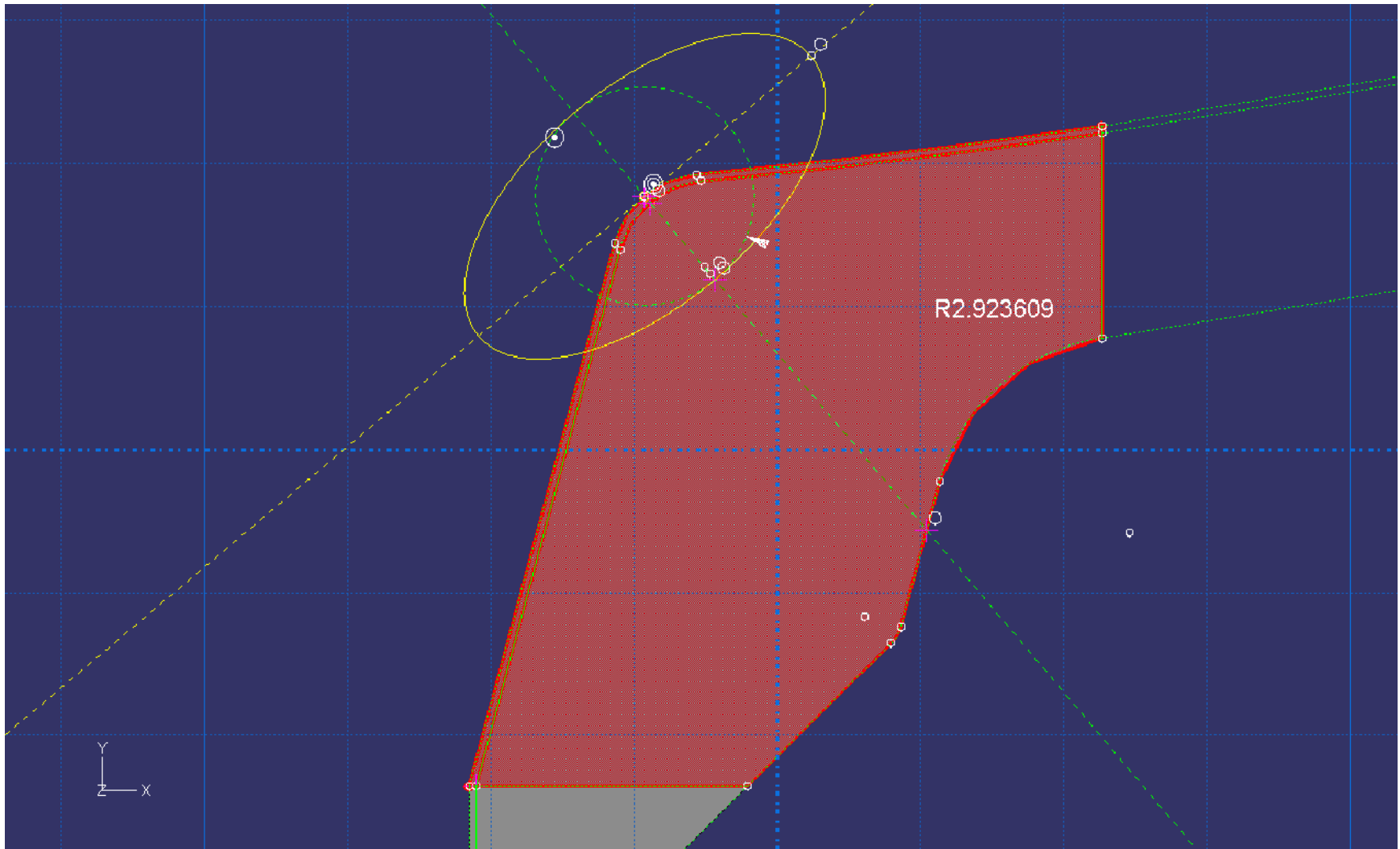


Figure 21. 1/4t Corner Crack Location and Configuration for the BWR RO Nozzle

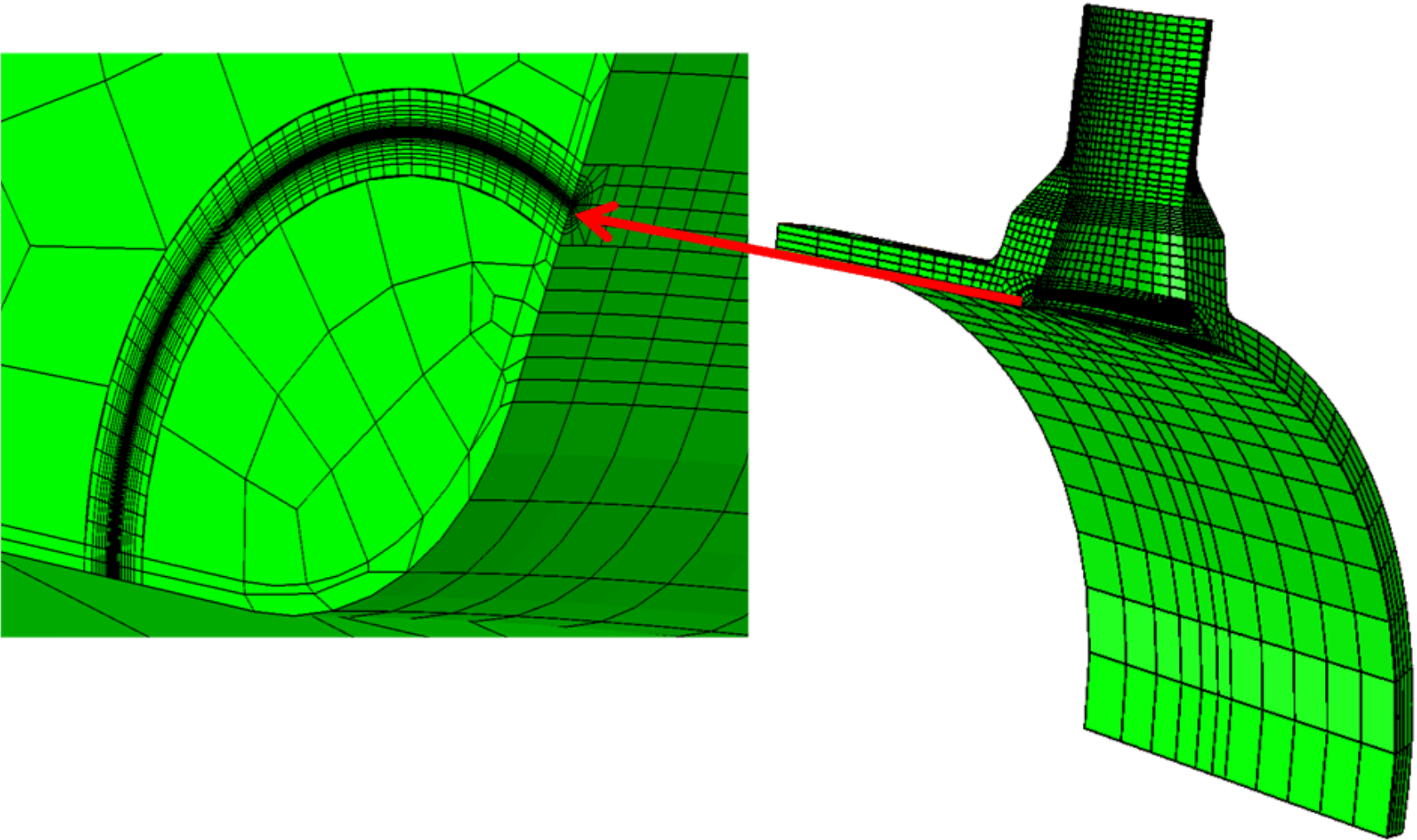


Figure 22. 3-D FEM for the BWR RO Nozzle with a Postulated $\frac{1}{4}t$ Circular Corner Crack

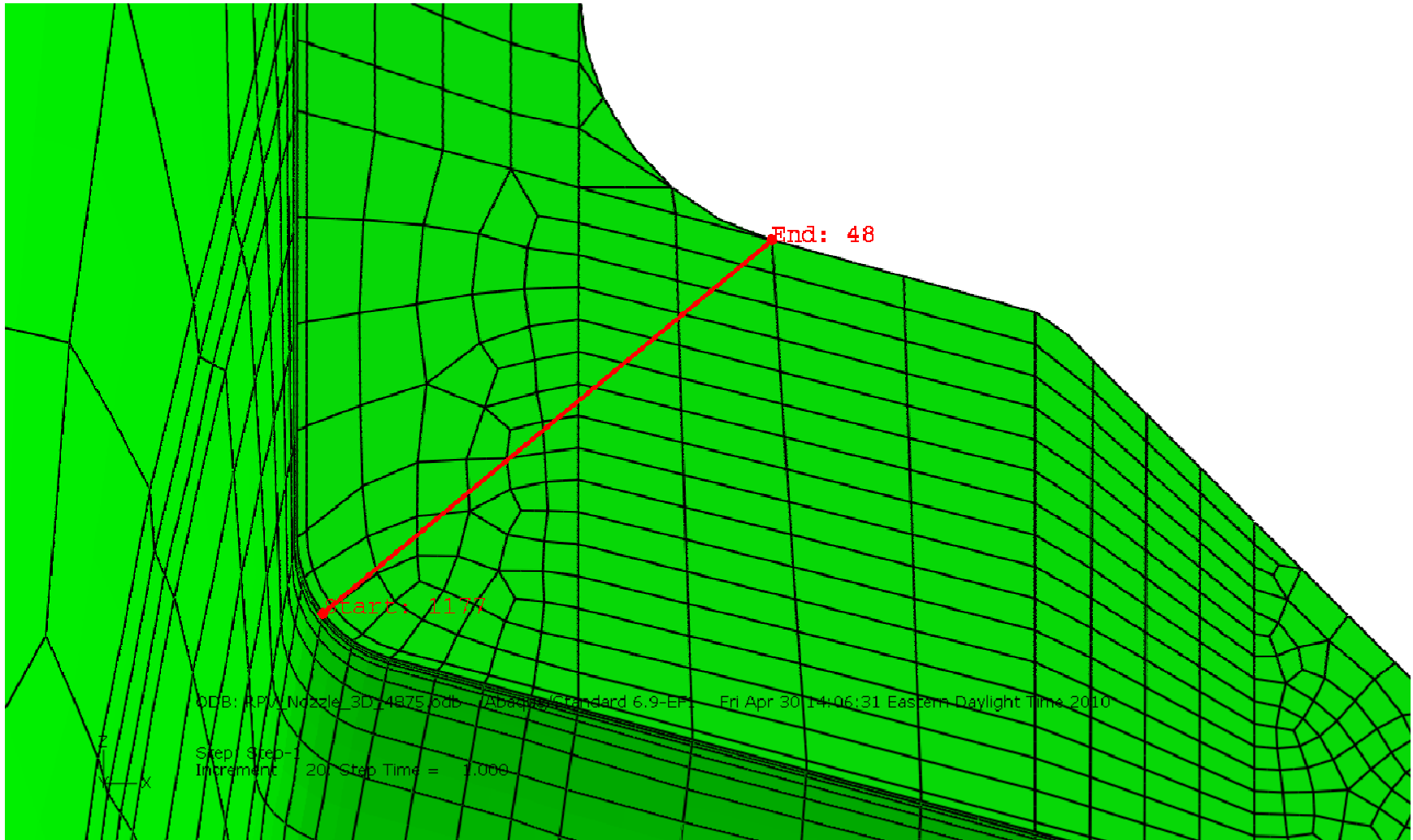


Figure 23. 45° Path Selected Through the BWR RO Nozzle Corner at the Azimuth of Maximum Pressure Stress

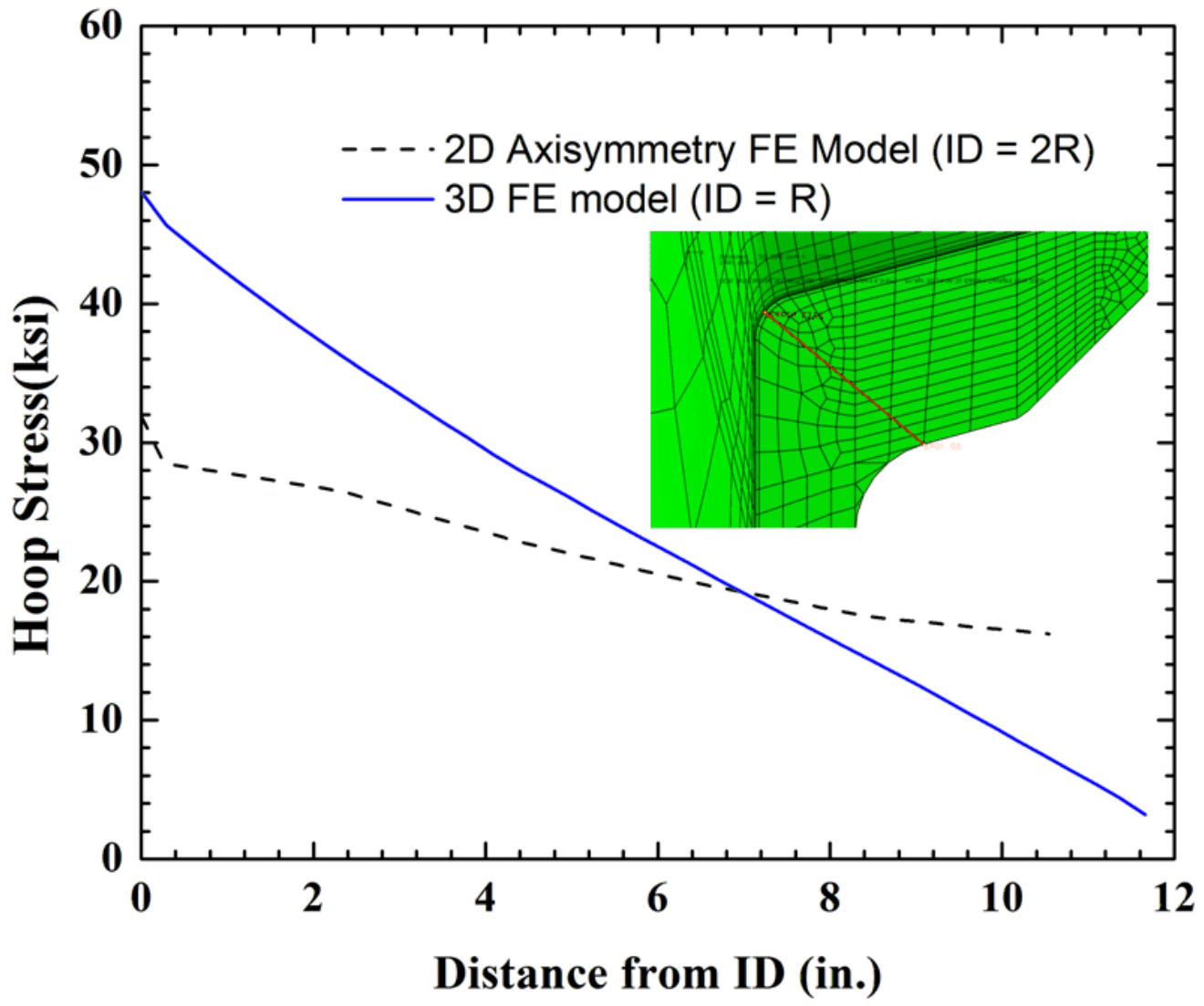


Figure 24. Hoop Stress as a Function of Distance Along the Nozzle Corner Path for the BWR RO Nozzle

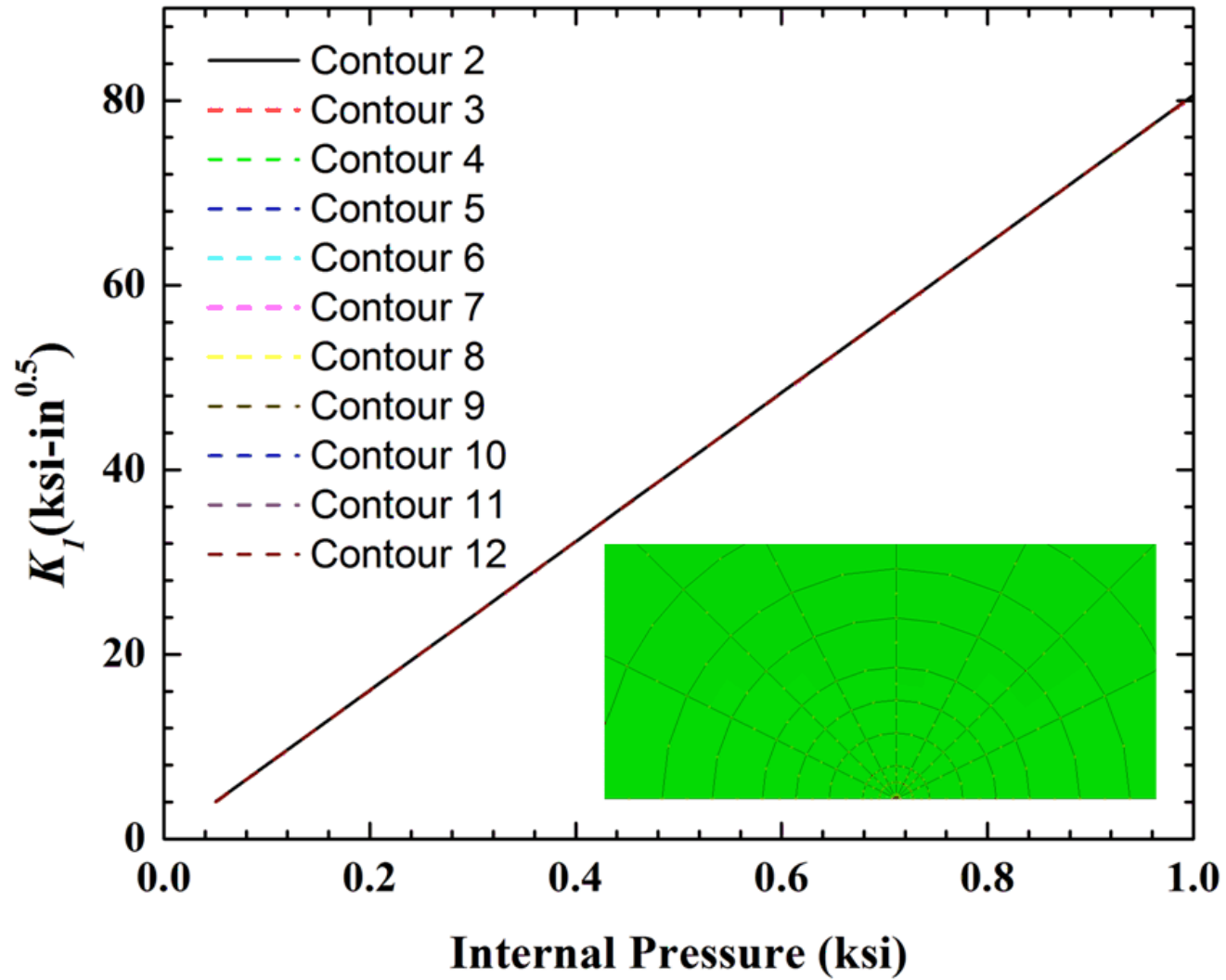


Figure 25. K_I as a Function of Internal Pressure Loading Using Different Stress Profiles for the BWR RO Nozzle

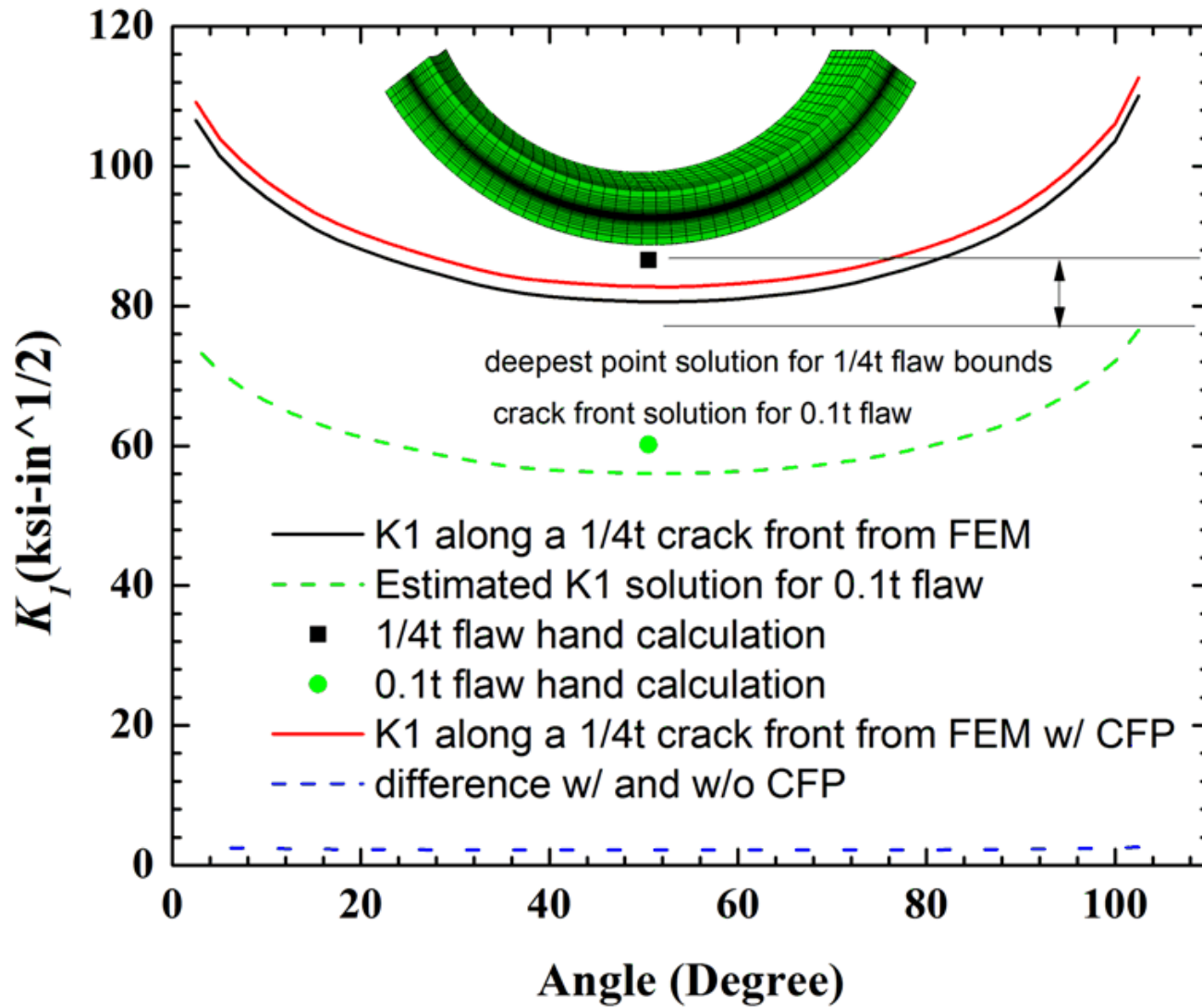


Figure 26. Stress Intensity Factors (K_I) Along the Crack Front Under Applied Pressure Loading for the BWR RO Nozzle

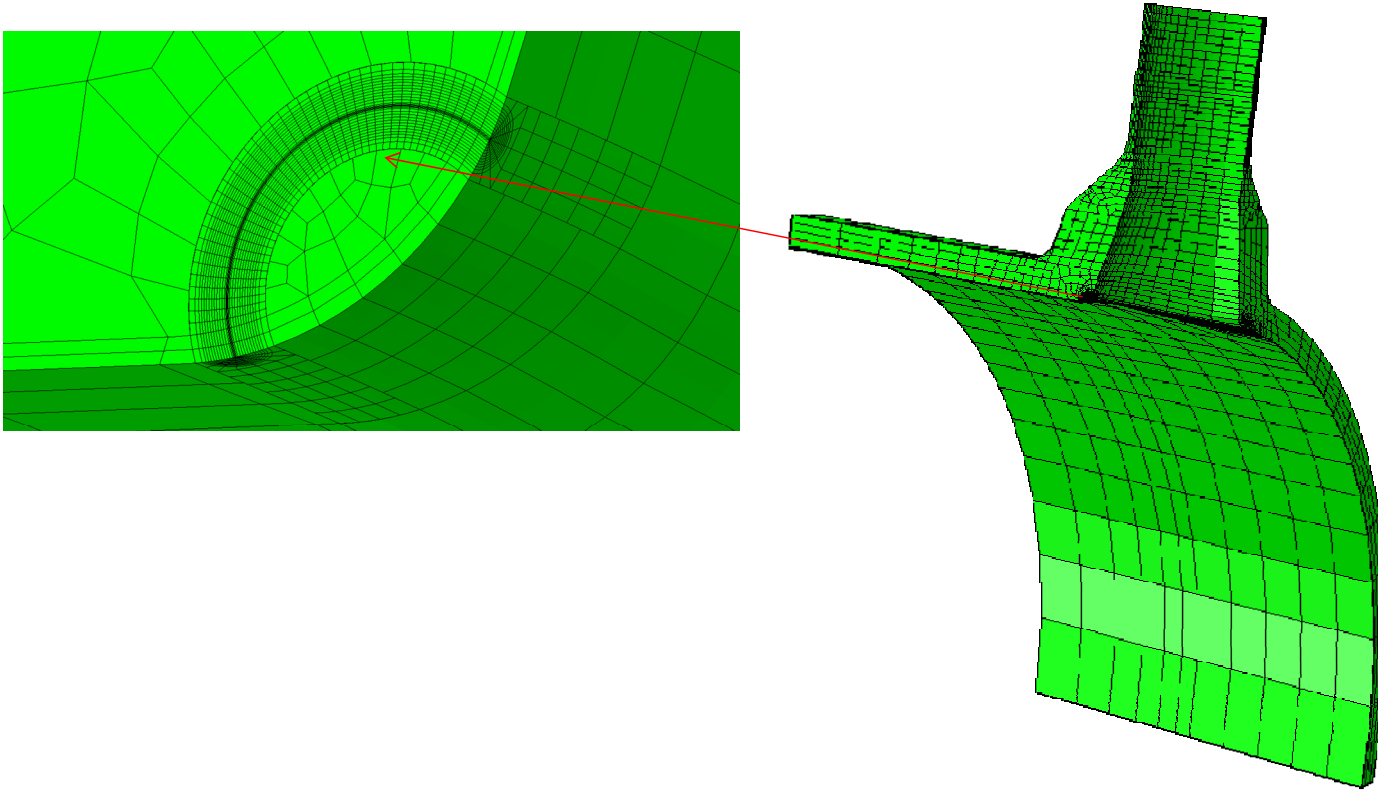


Figure 27. Finite-element Model for BWR Recirculation Outlet Nozzle with Postulated $0.1t$ Circular Surface Corner Crack.

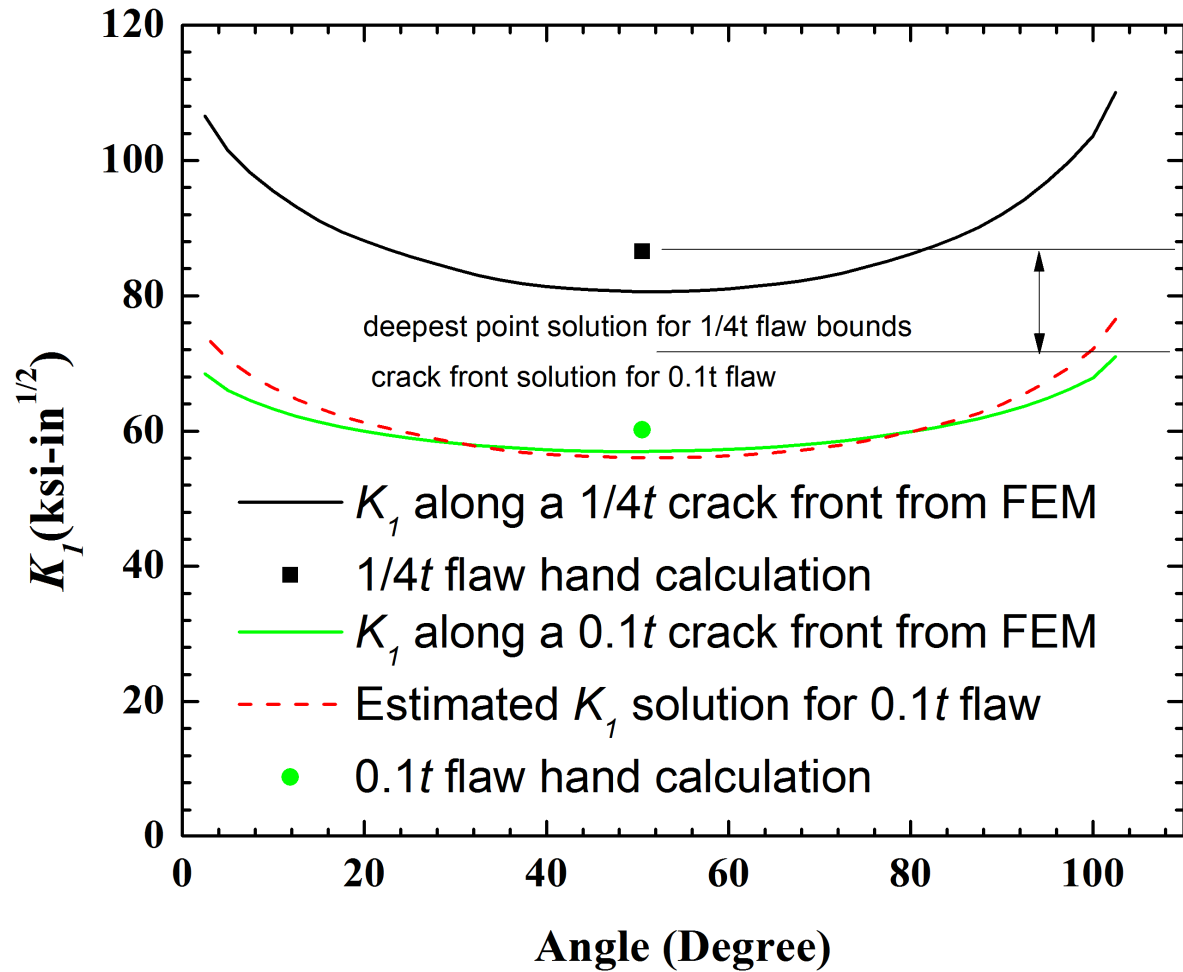


Figure 28. Stress Intensity Factors (K_I) Along the Crack Front Under Applied Pressure Loading for the BWR RO Nozzle with Postulated $1/4t$ and $0.1t$ Flaws.

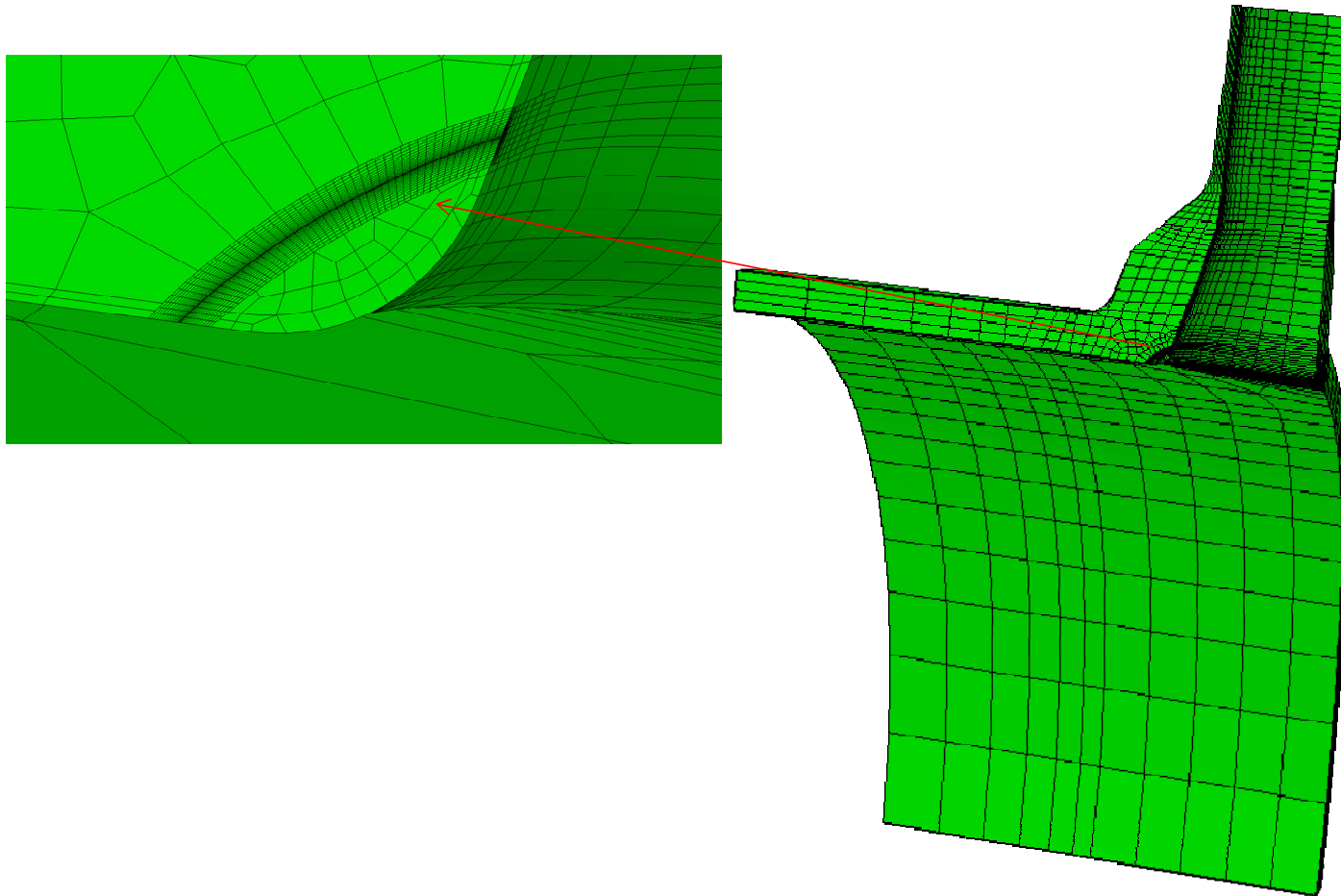


Figure 29. Finite-element Model for BWR Recirculation Outlet Nozzle with Postulated $0.1t$ Semi-Elliptical Surface Corner Crack (Aspect Ratio of 6).

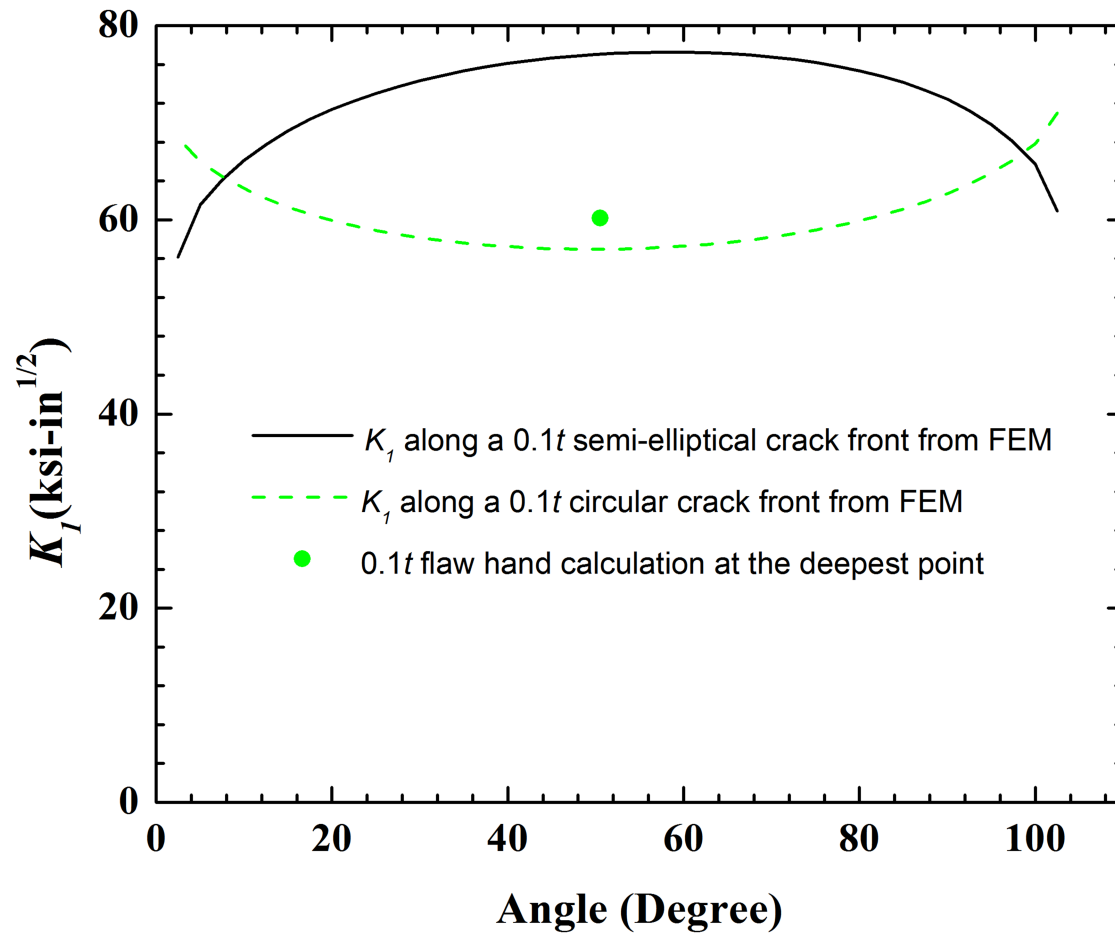


Figure 30. Comparison of Stress Intensity Factors Along the Crack Front for a Postulated $0.1t$ Semi-Elliptical Corner Flaw and a Postulated $1/4t$ Circular Corner Flaw in BWR RO Nozzle Subjected to Pressure Loading.

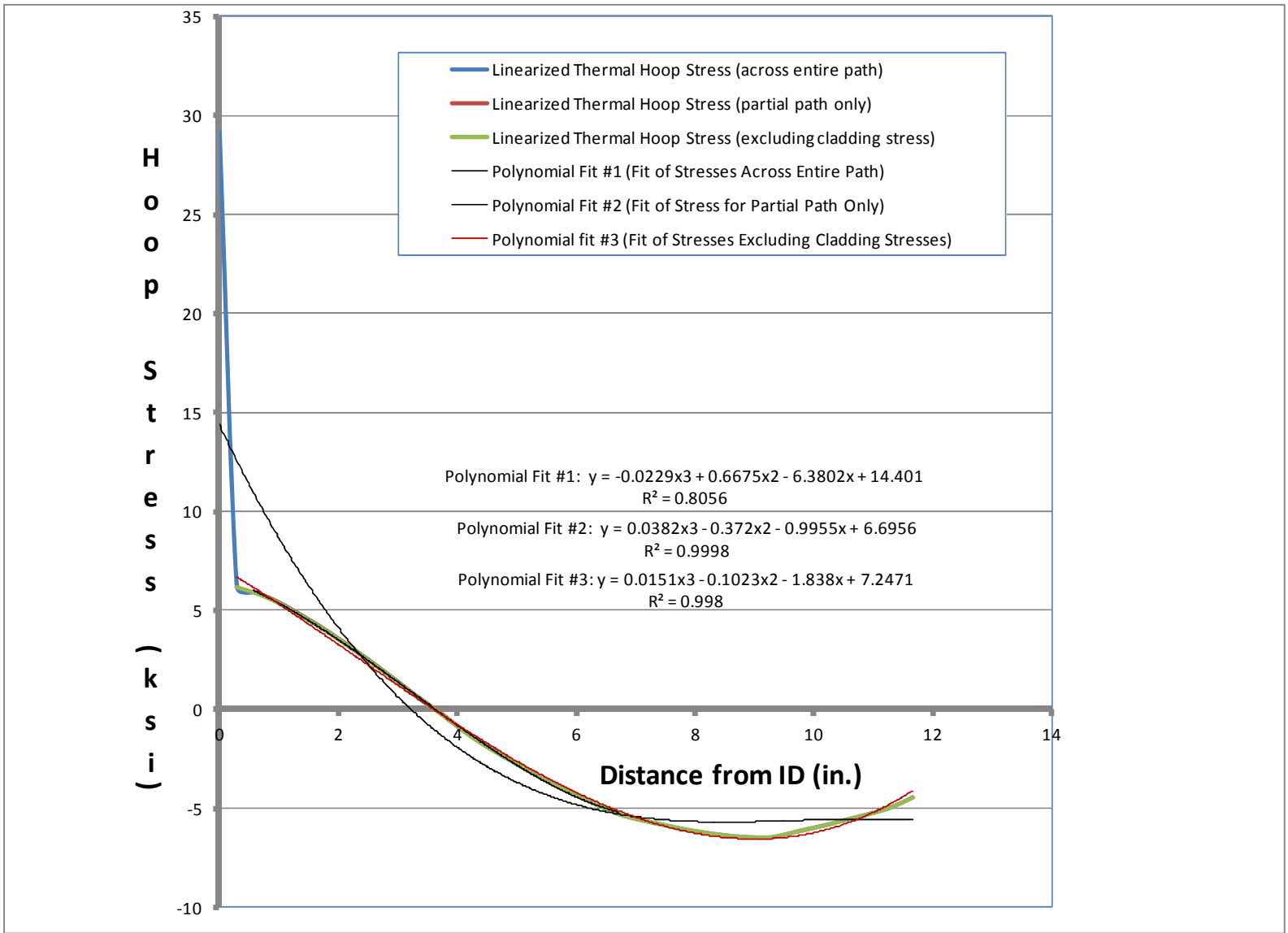


Figure 31. Hoop Stress as a Function of BWR RO Nozzle Corner Thickness at the Blend Radius under Thermal Loading

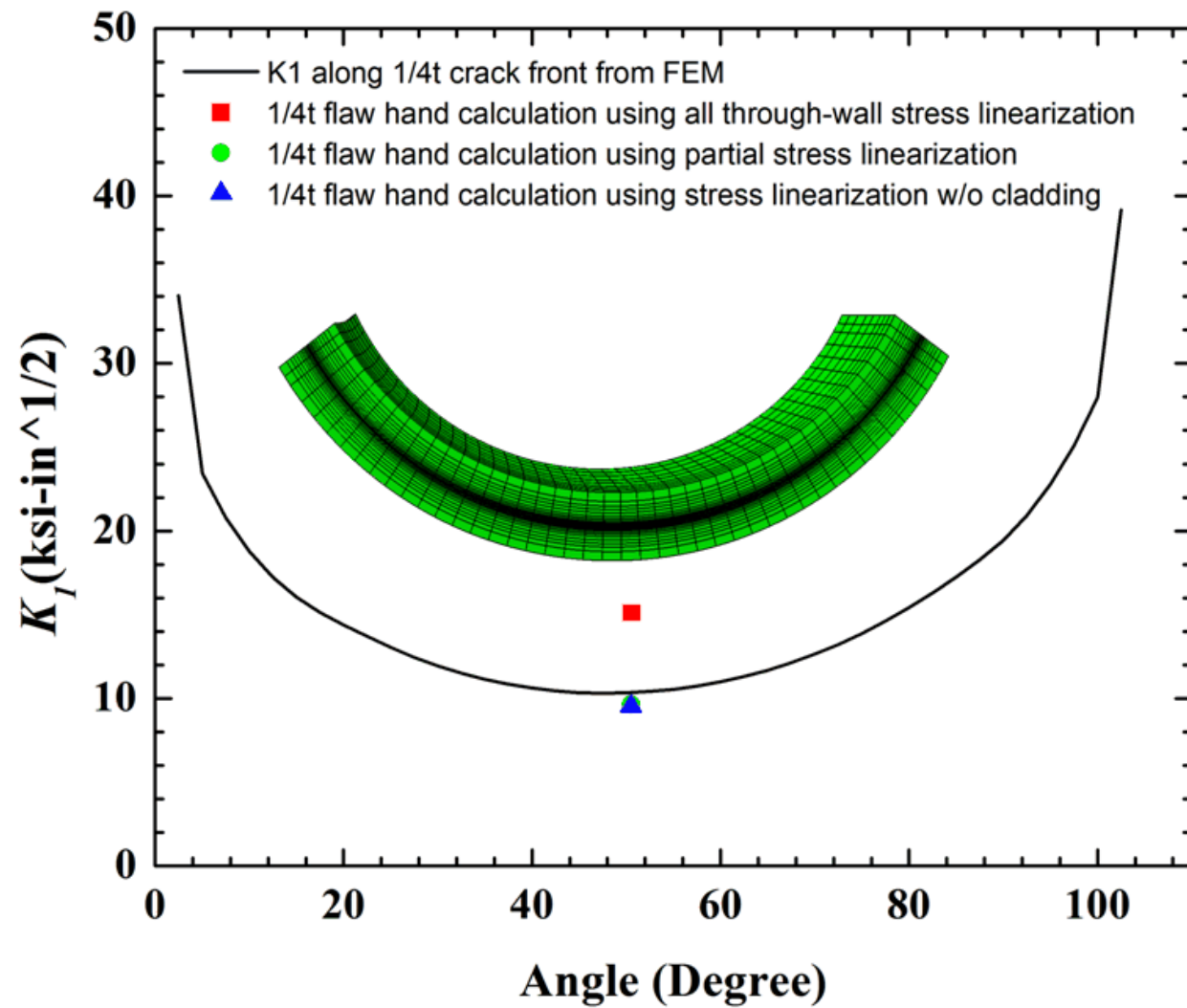


Figure 32. Stress Intensity Factor (K_I) Along the Crack Front Under Thermal Loading for the BWR RO Nozzle

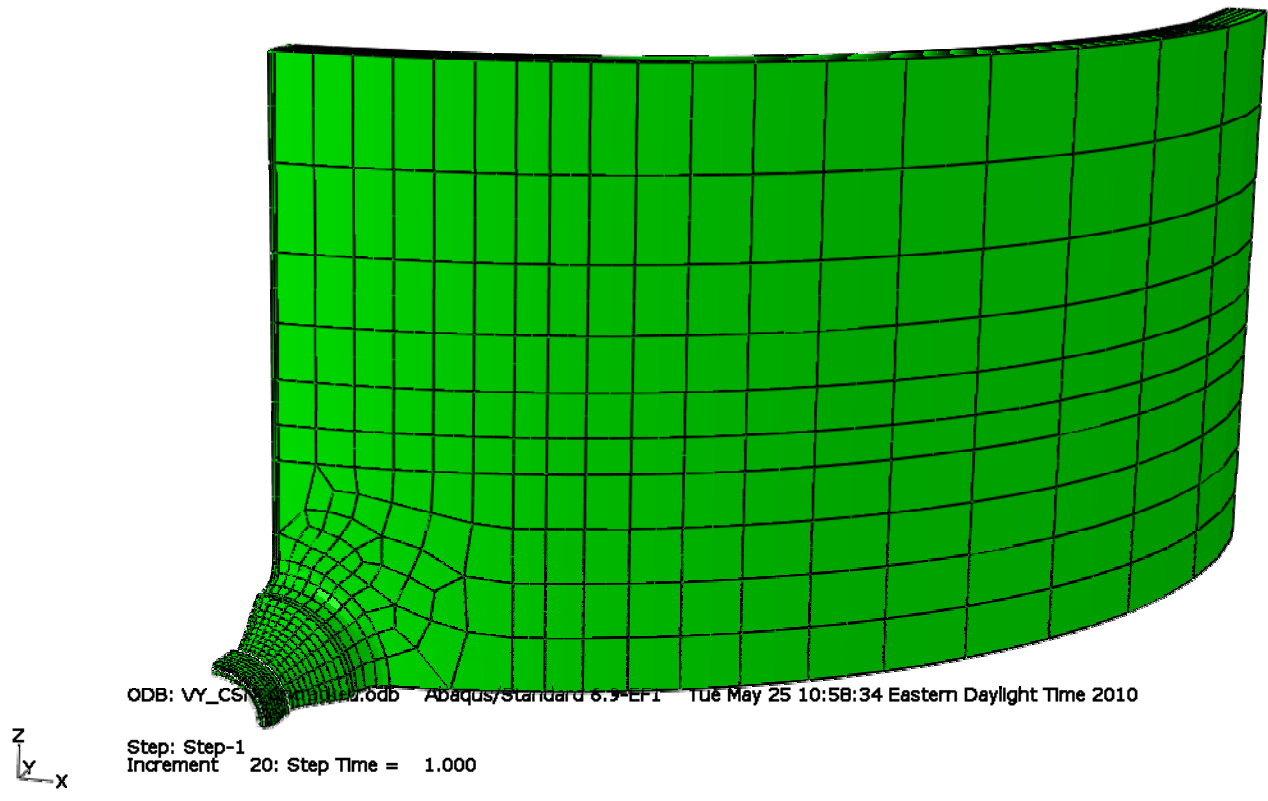


Figure 34. 3-D FEM for the Uncracked BWR CS Nozzle

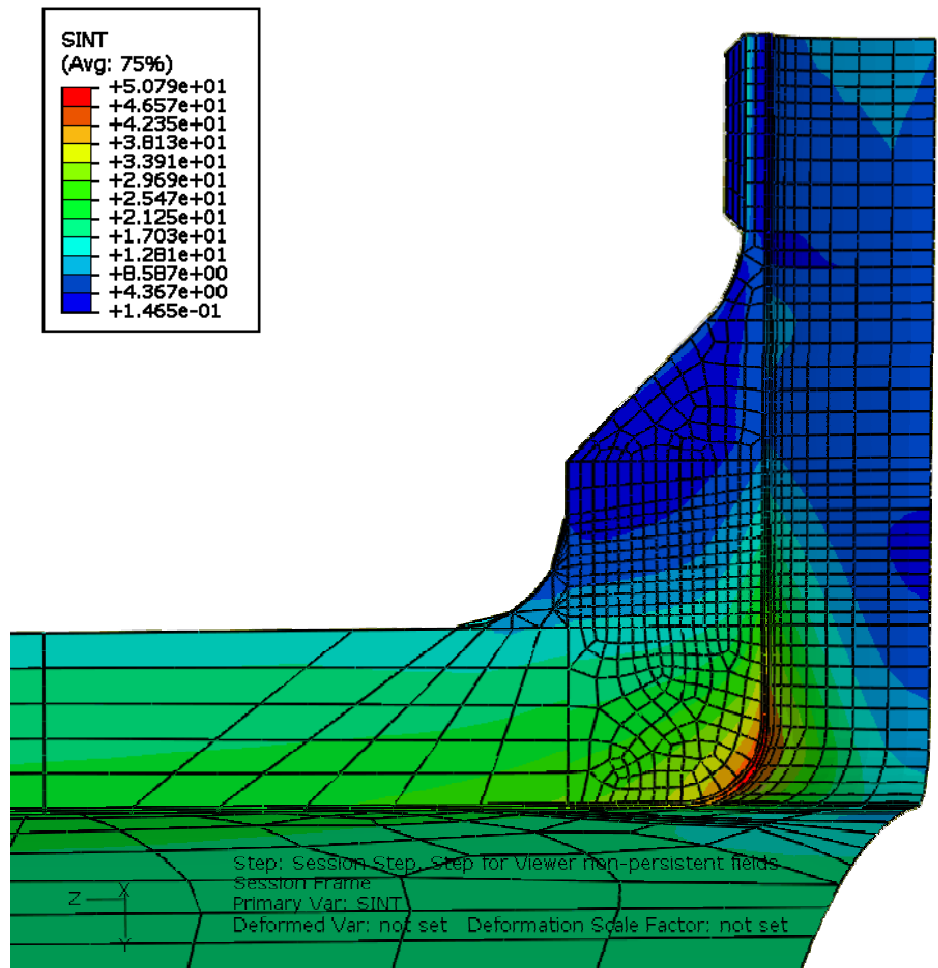


Figure 35. Stress Intensity (SINT) for the BWR CS Nozzle Subjected to 1,000 psi Internal Pressure

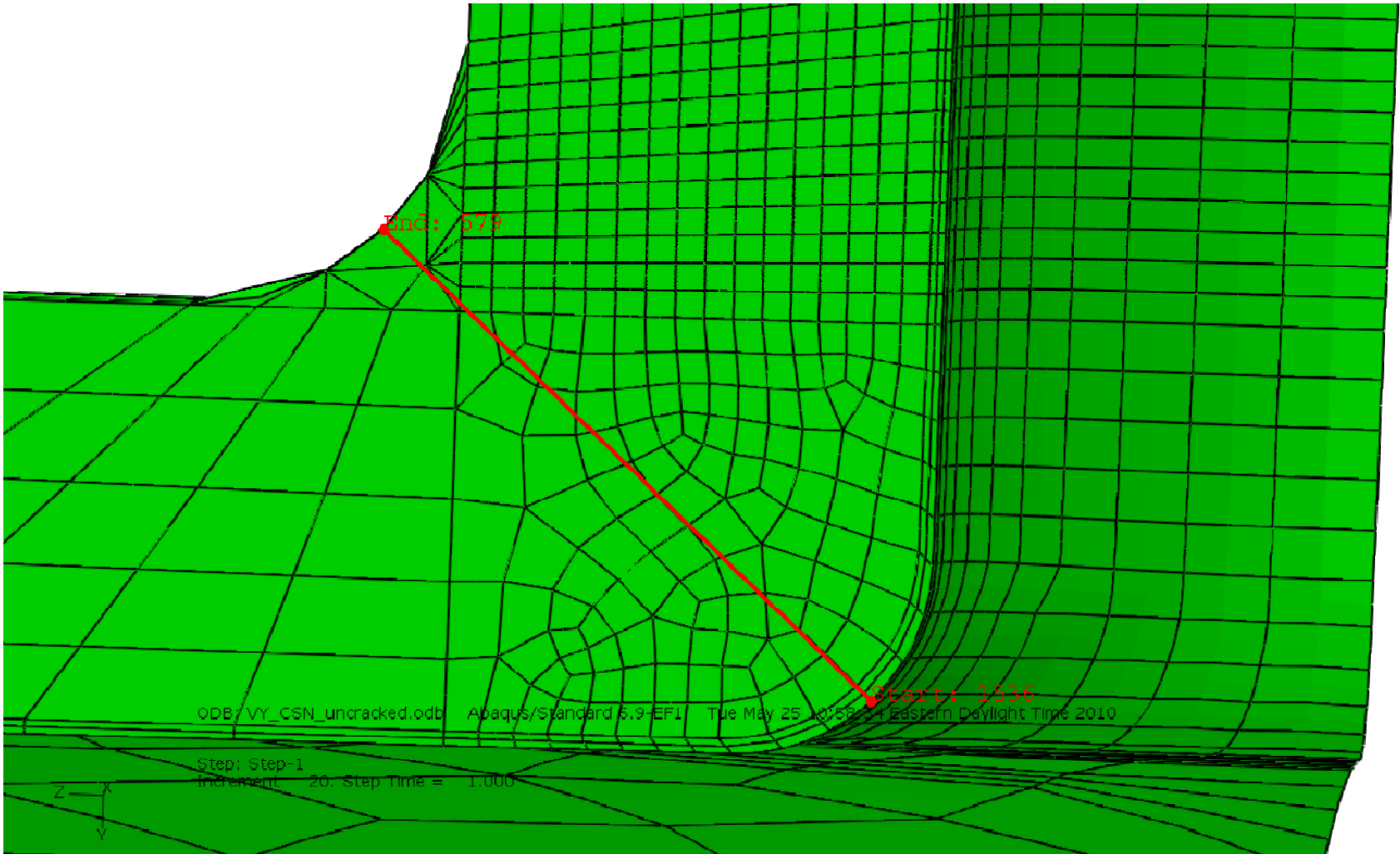


Figure 36. Hoop Stress Extraction Path Selected for the BWR CS Nozzle

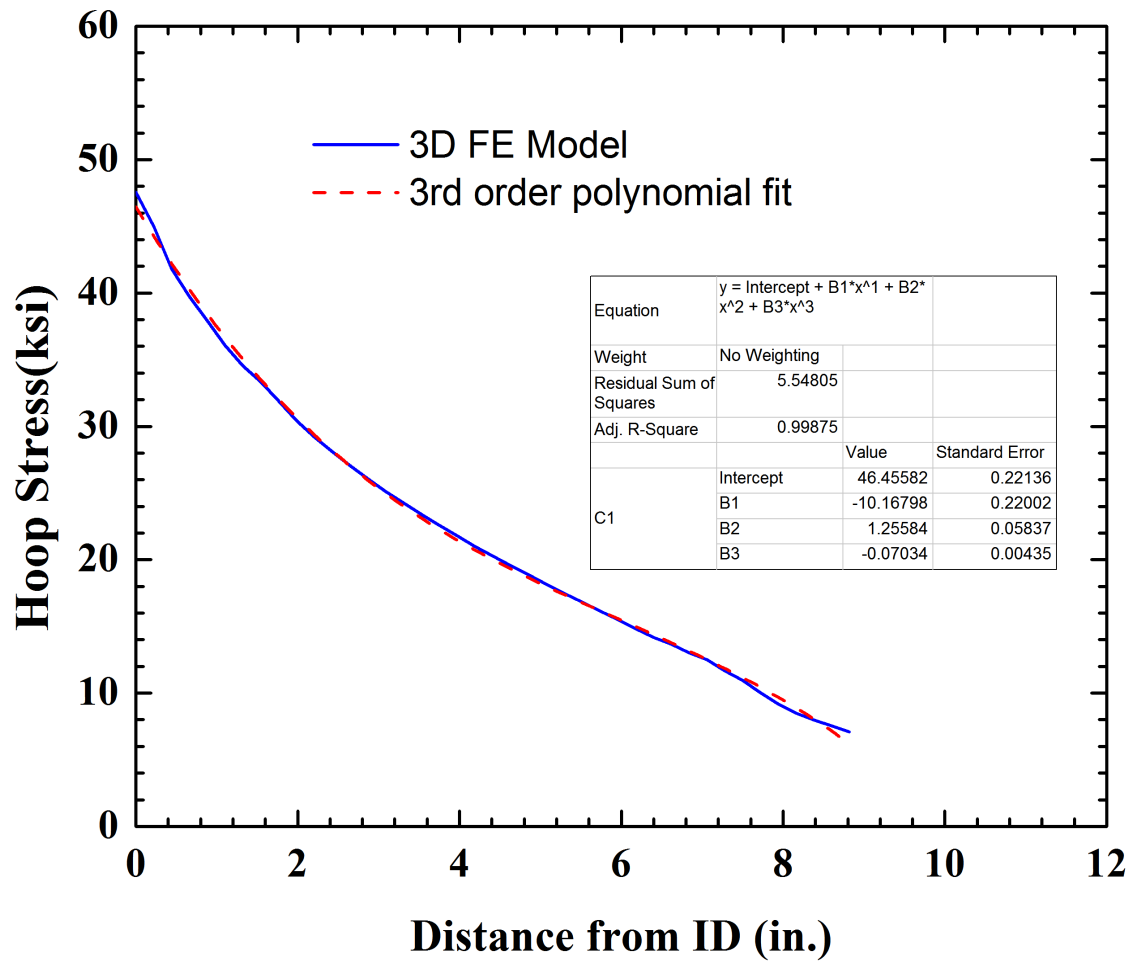


Figure 37. Hoop Stress Along the Selected Stress Path for the BWR CS Nozzle Under 1,000 psi Internal Pressure

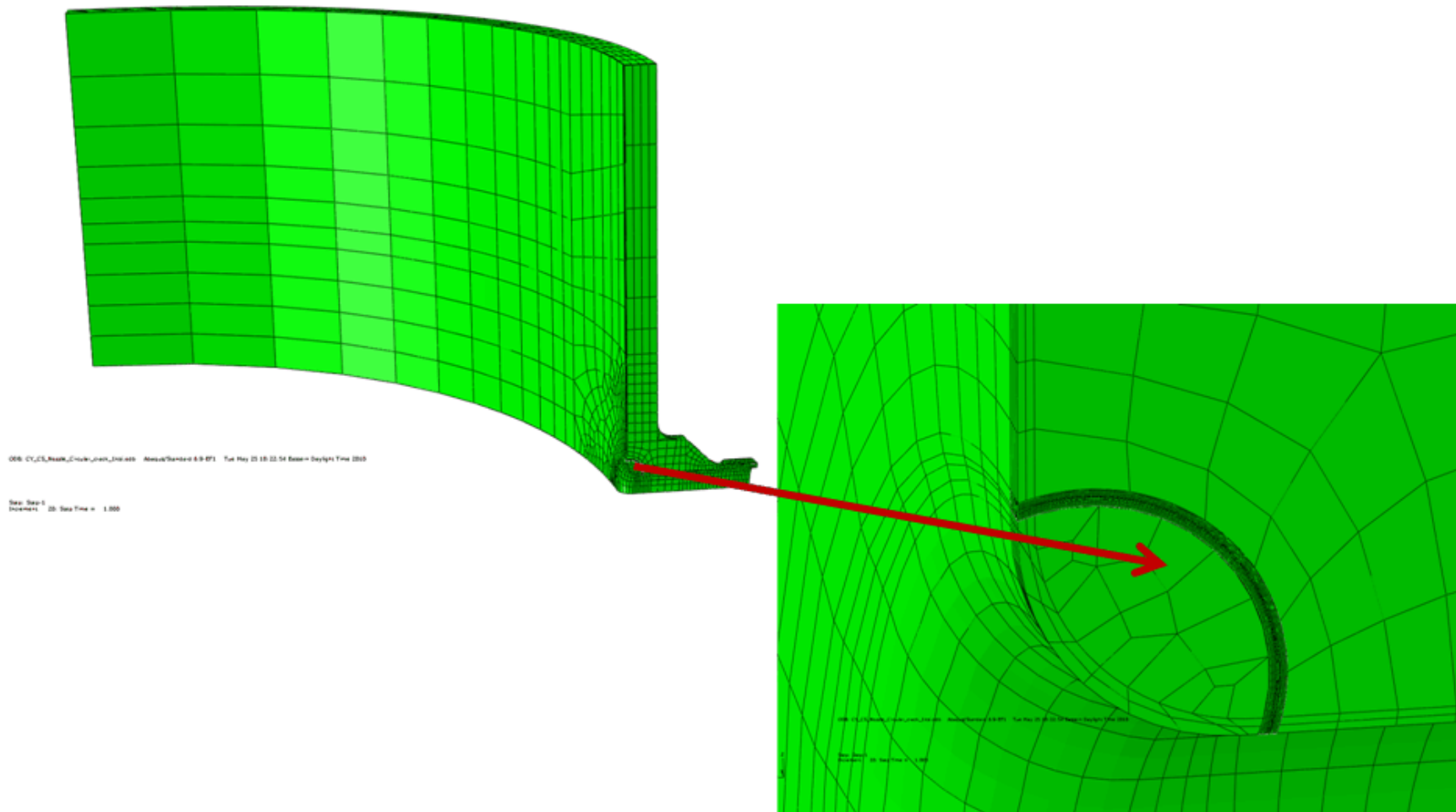


Figure 38. 3-D FEM for the BWR CS Nozzle with a Postulated $\frac{1}{4}t$ Circular Corner Crack

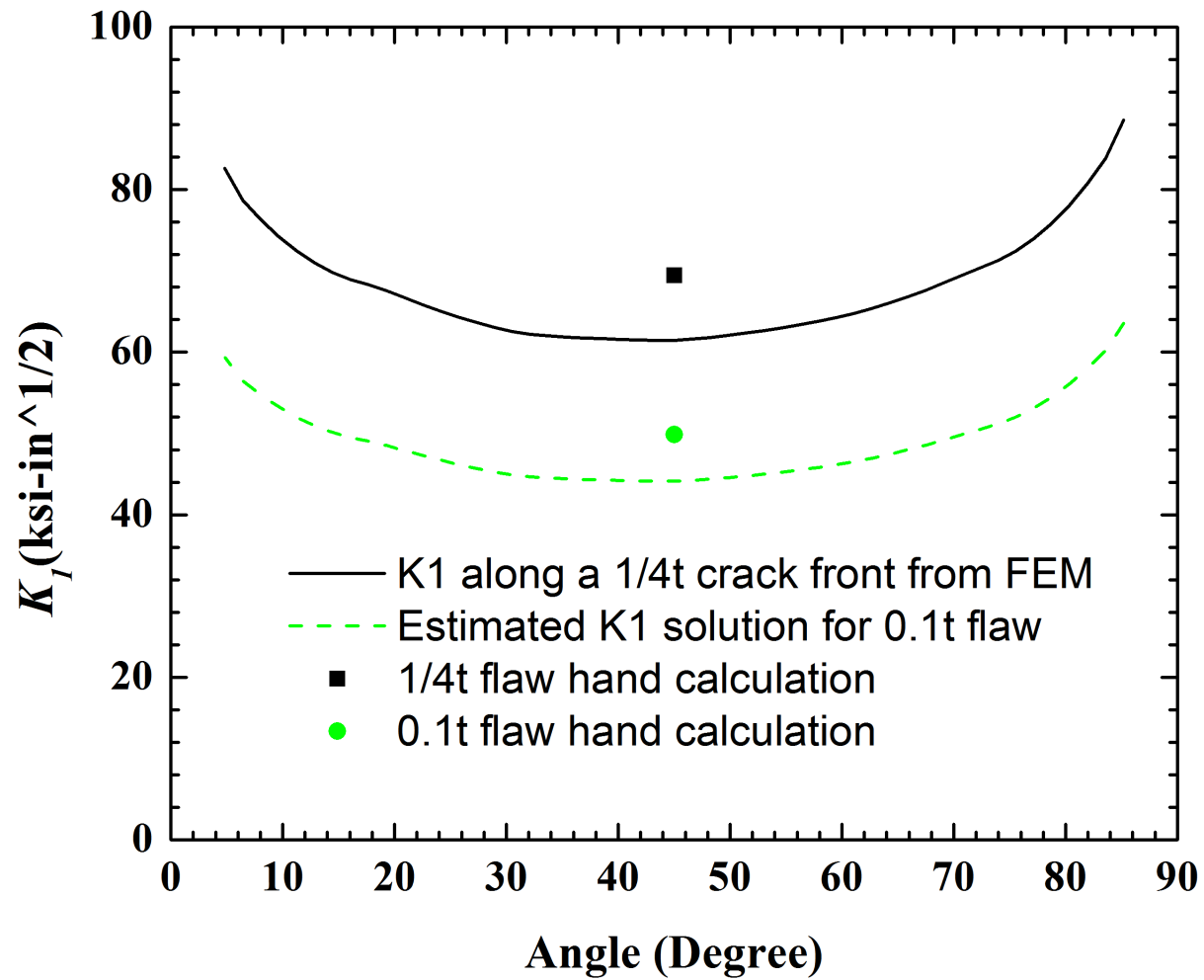


Figure 39. Stress Intensity Factor (K_I) Along the Crack Front for 1,000 psig Pressure Loading for the BWR CS Nozzle

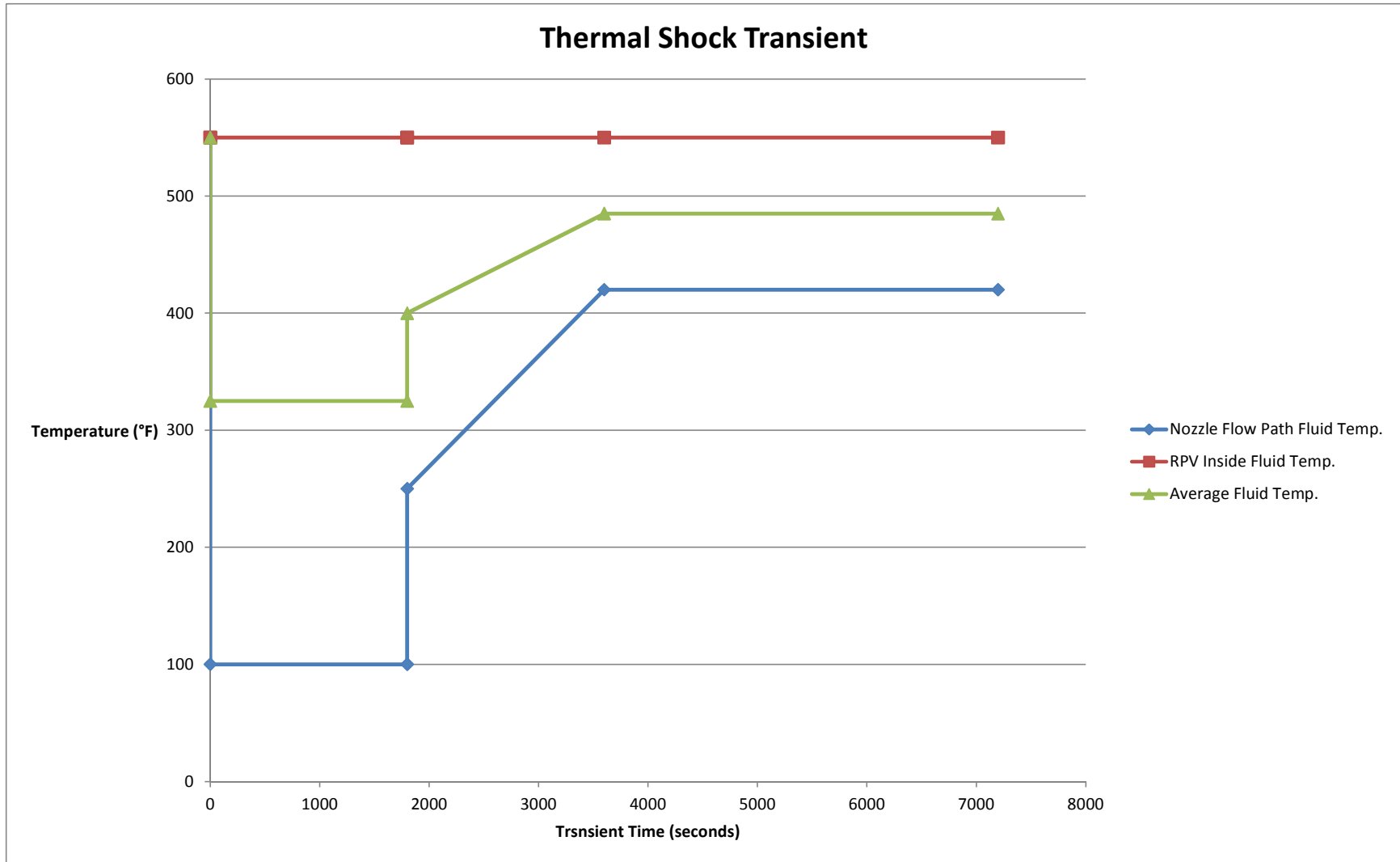


Figure 40. BWR Thermal Shock Transient Applicable to BWR Feedwater Nozzles

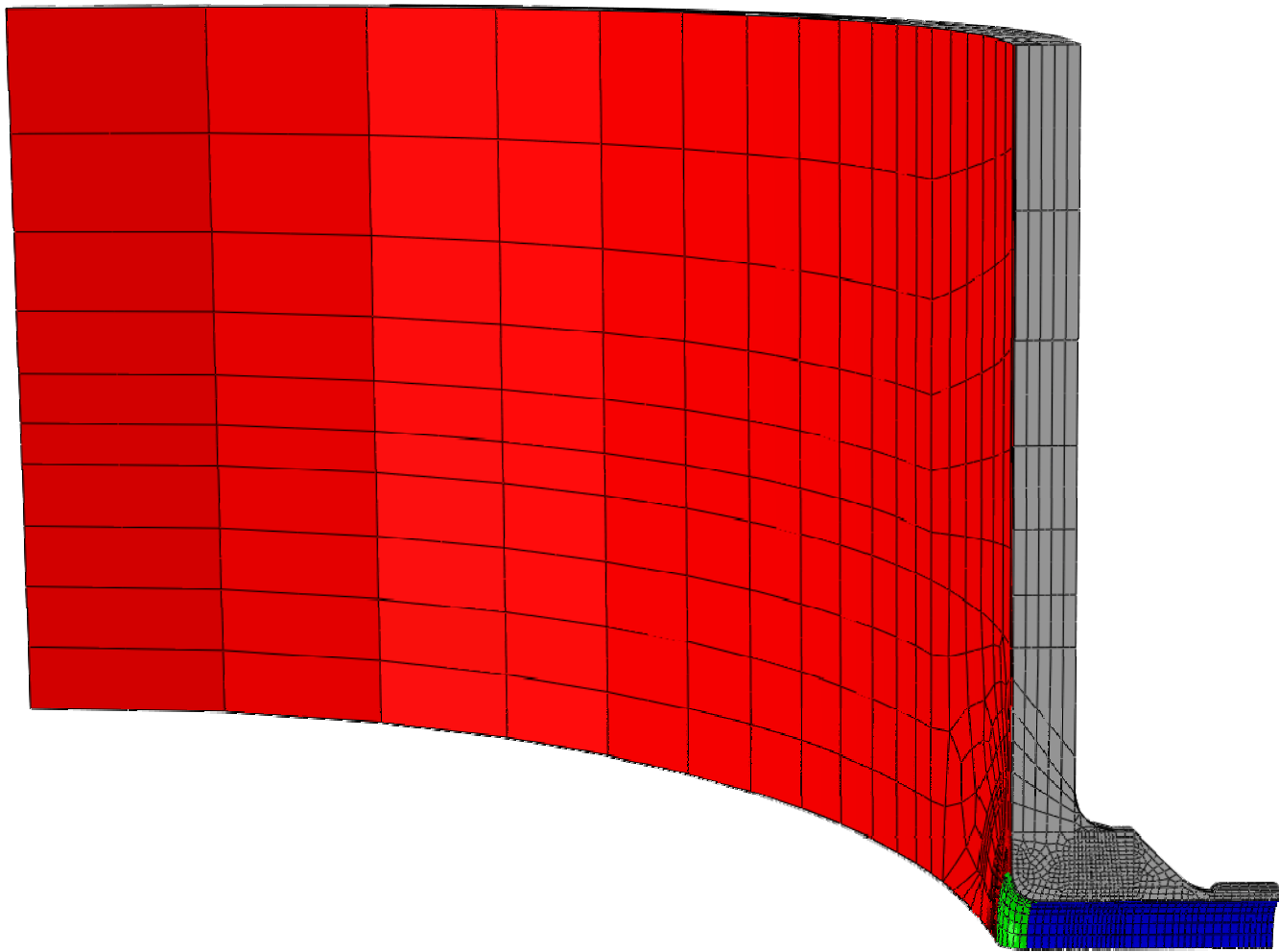


Figure 41. BWR Thermal Shock Transient Applied to Three Regions of the Uncracked 3-D BWR CS Nozzle FEM

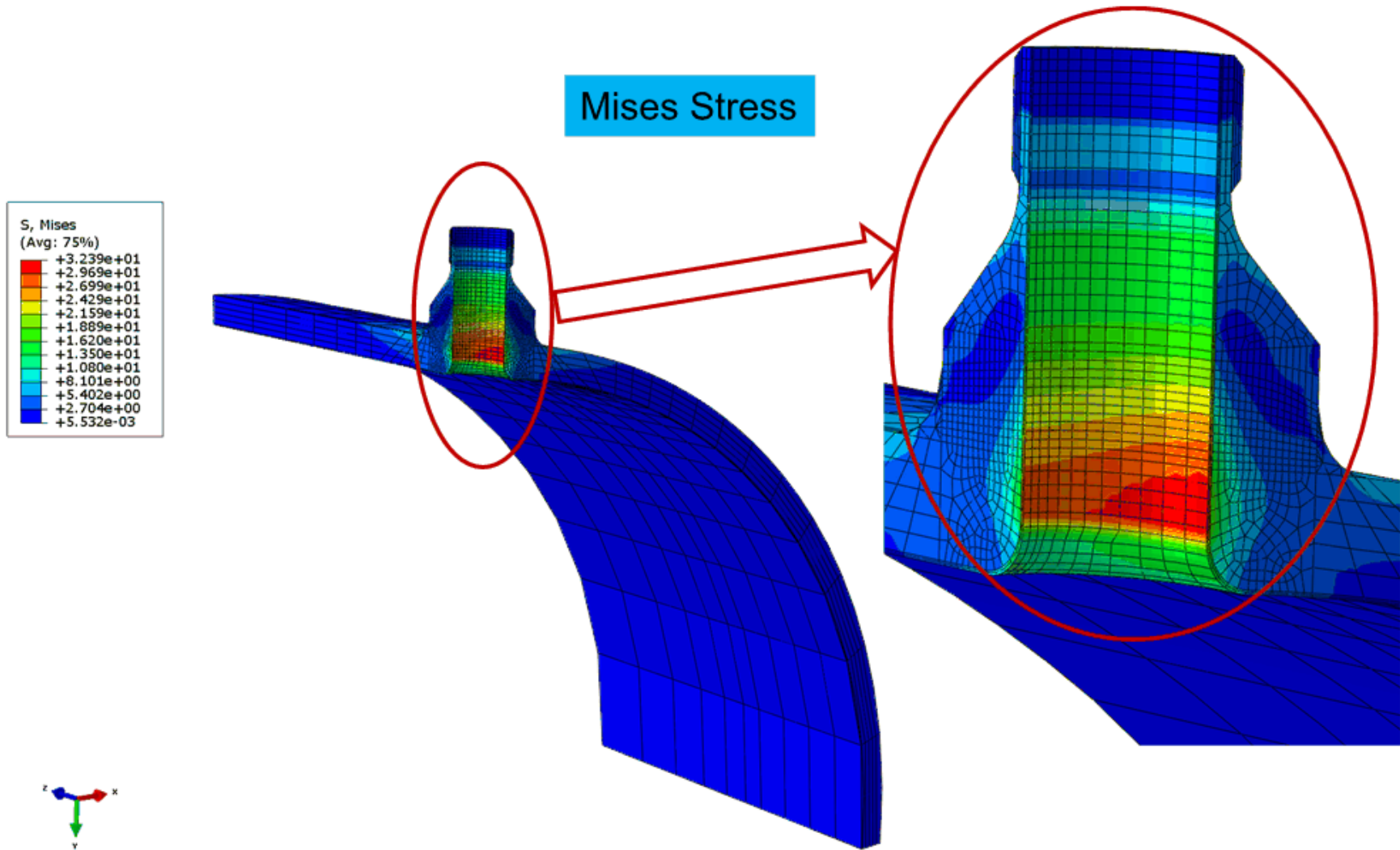


Figure 42. Mises Stress for the Uncracked BWR CS Nozzle 3-D FEM Subjected to a BWR Thermal Shock Transient

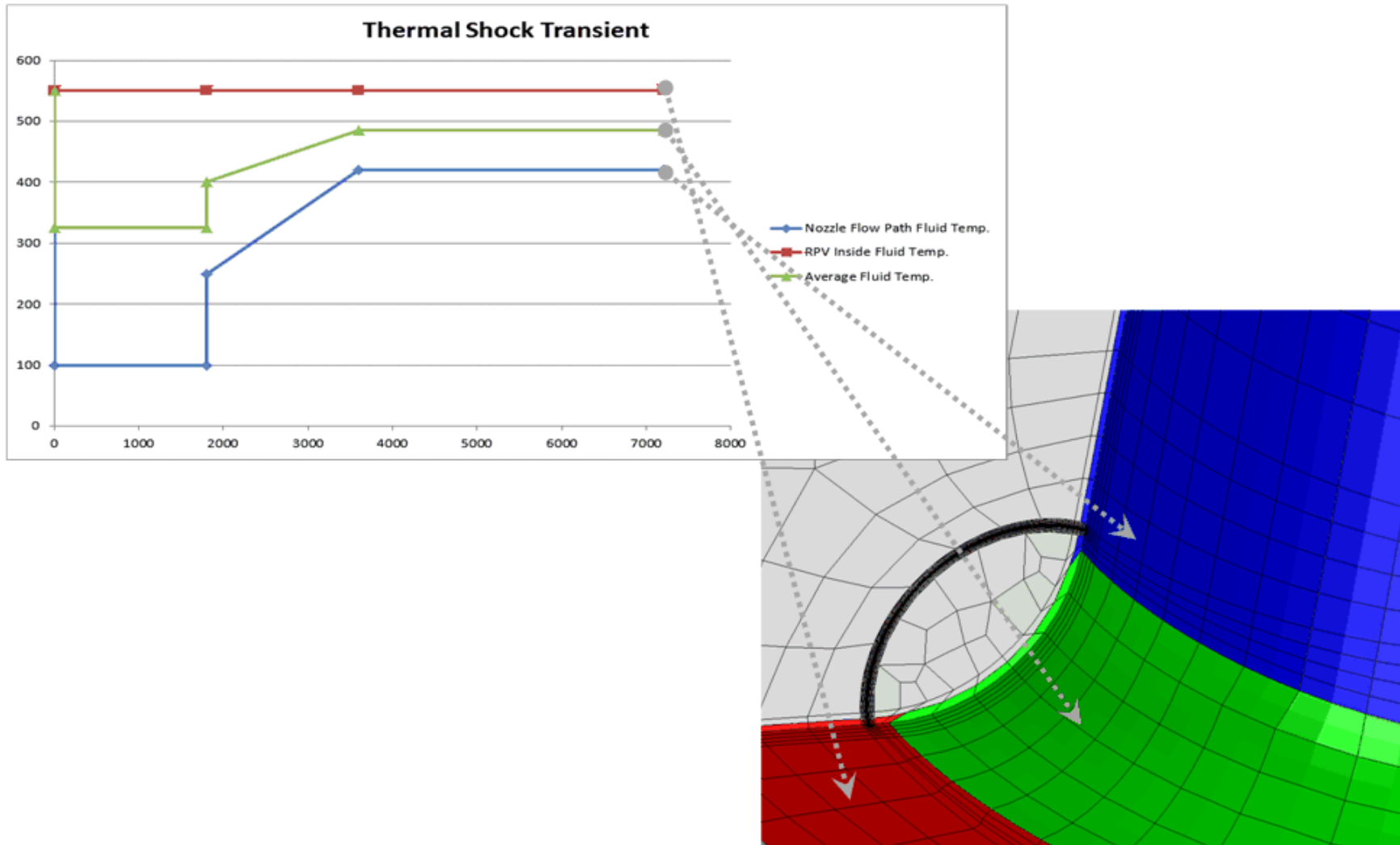


Figure 43. BWR Thermal Shock Transient Applied to Three Regions of the BWR CS Nozzle 3-D FEM with a 1/4t Flaw

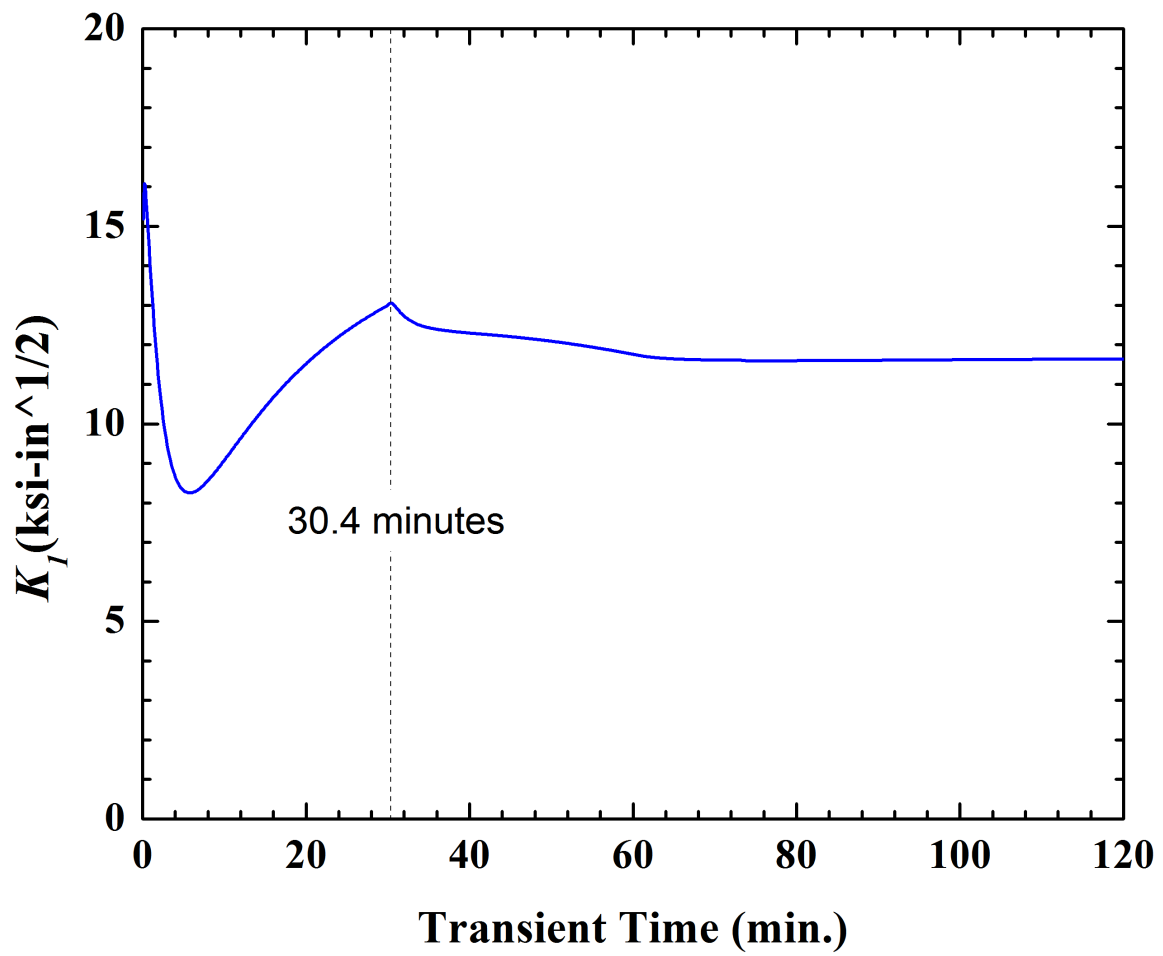


Figure 44. K_I near the $1/4t$ Location (Deepest Point) as a Function of Transient Time for the BWR Thermal Shock Transient

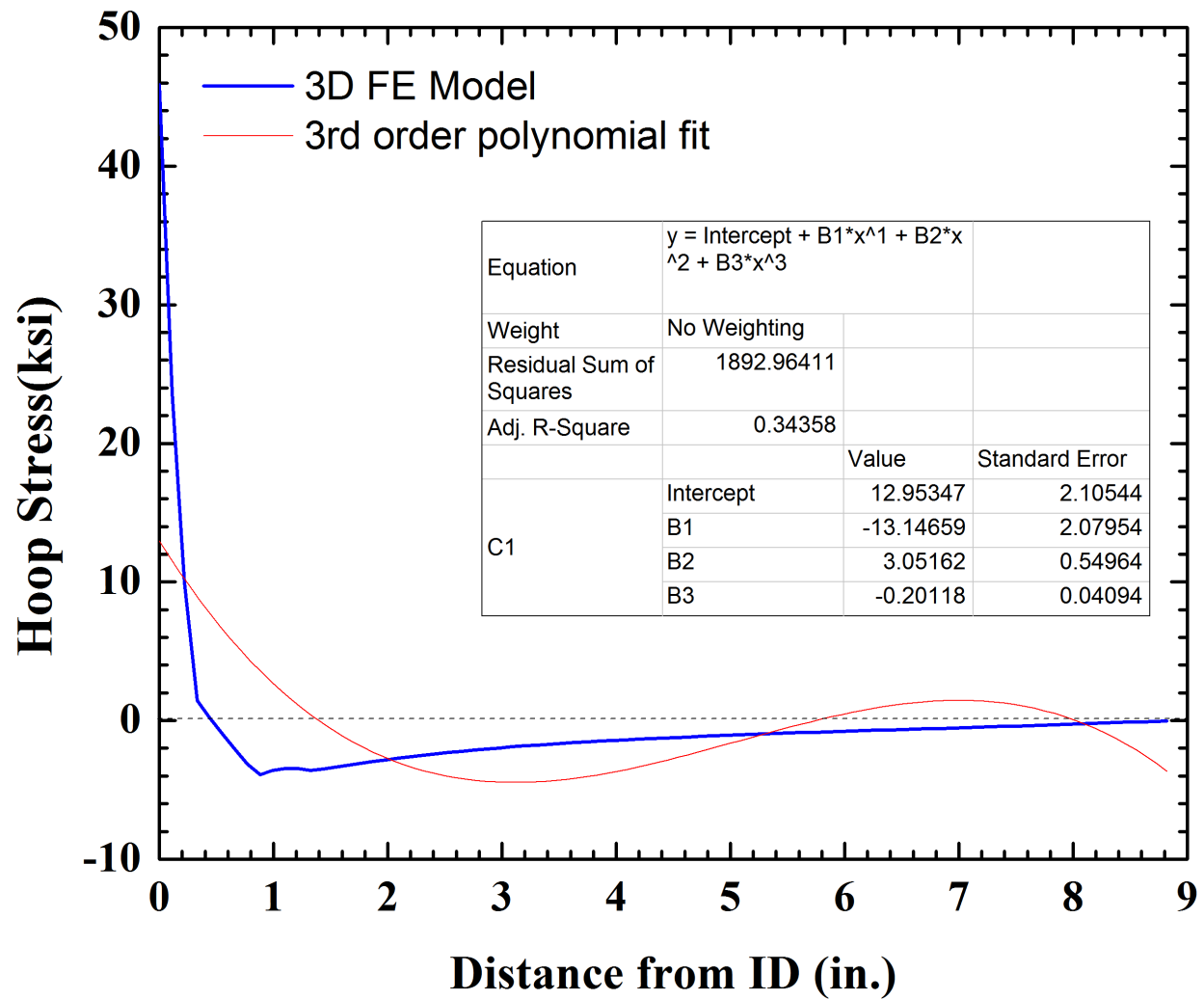


Figure 45. Hoop Stress Along the Selected Stress Path for the BWR CS Nozzle for a BWR Thermal Shock Transient at 0.1 Minute

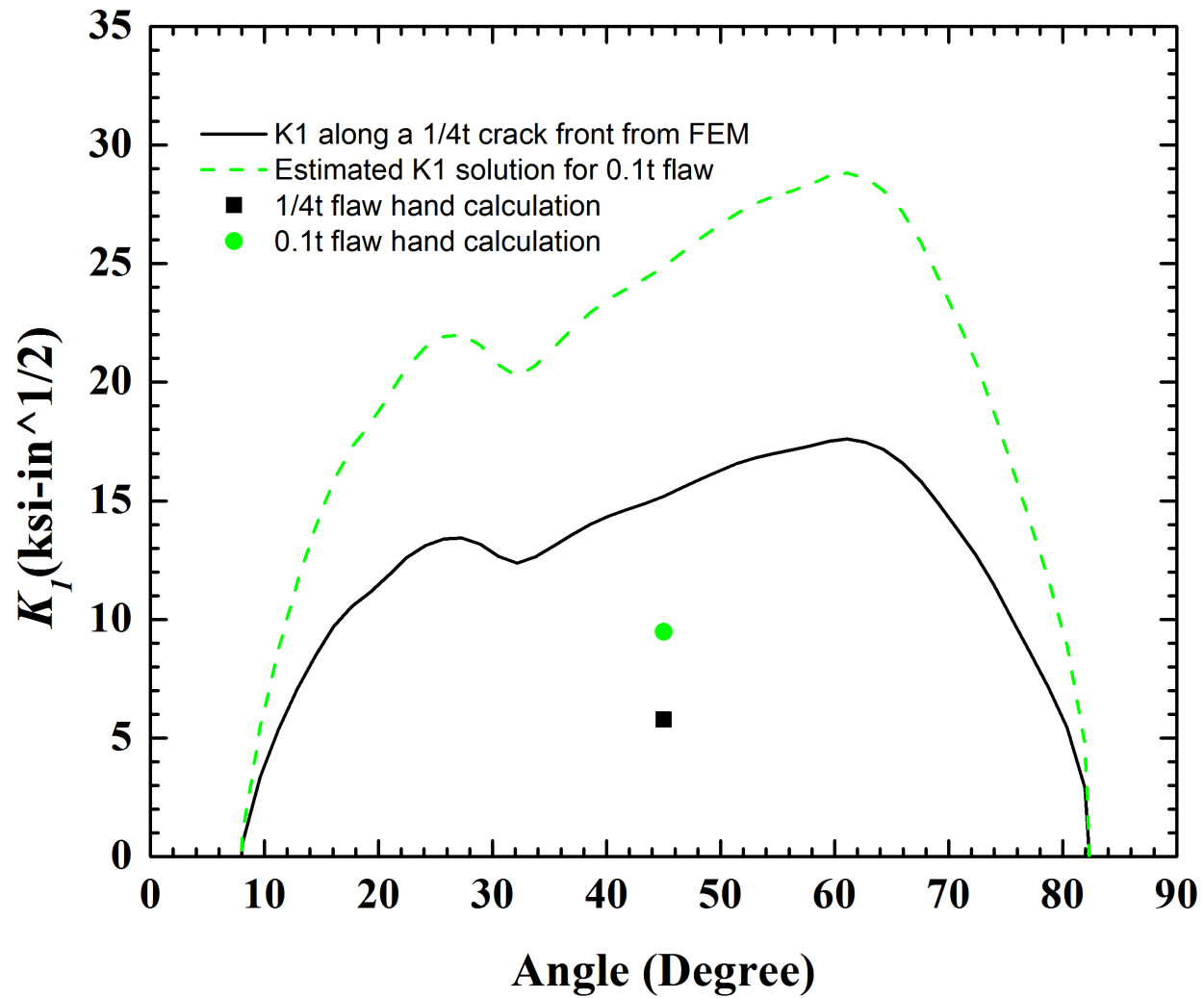


Figure 46. Stress Intensity Factor (K_I) Along the Crack Front of the BWR CS Nozzle for BWR Thermal Shock Loading at 0.1 Minute

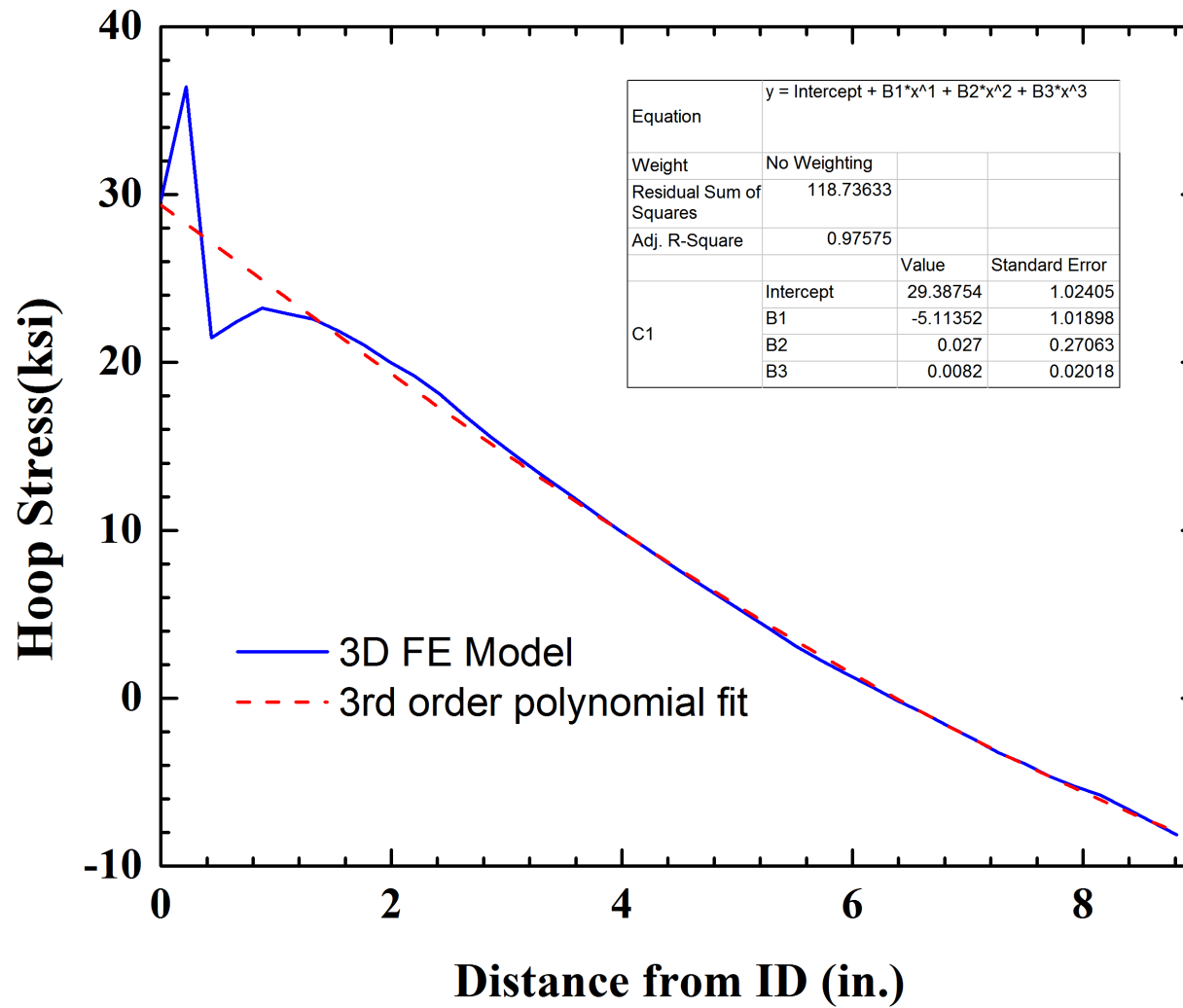


Figure 47. Hoop Stress Along the Selected Stress Path for the BWR CS Nozzle for a BWR Thermal Shock Transient at 30.4 Minutes

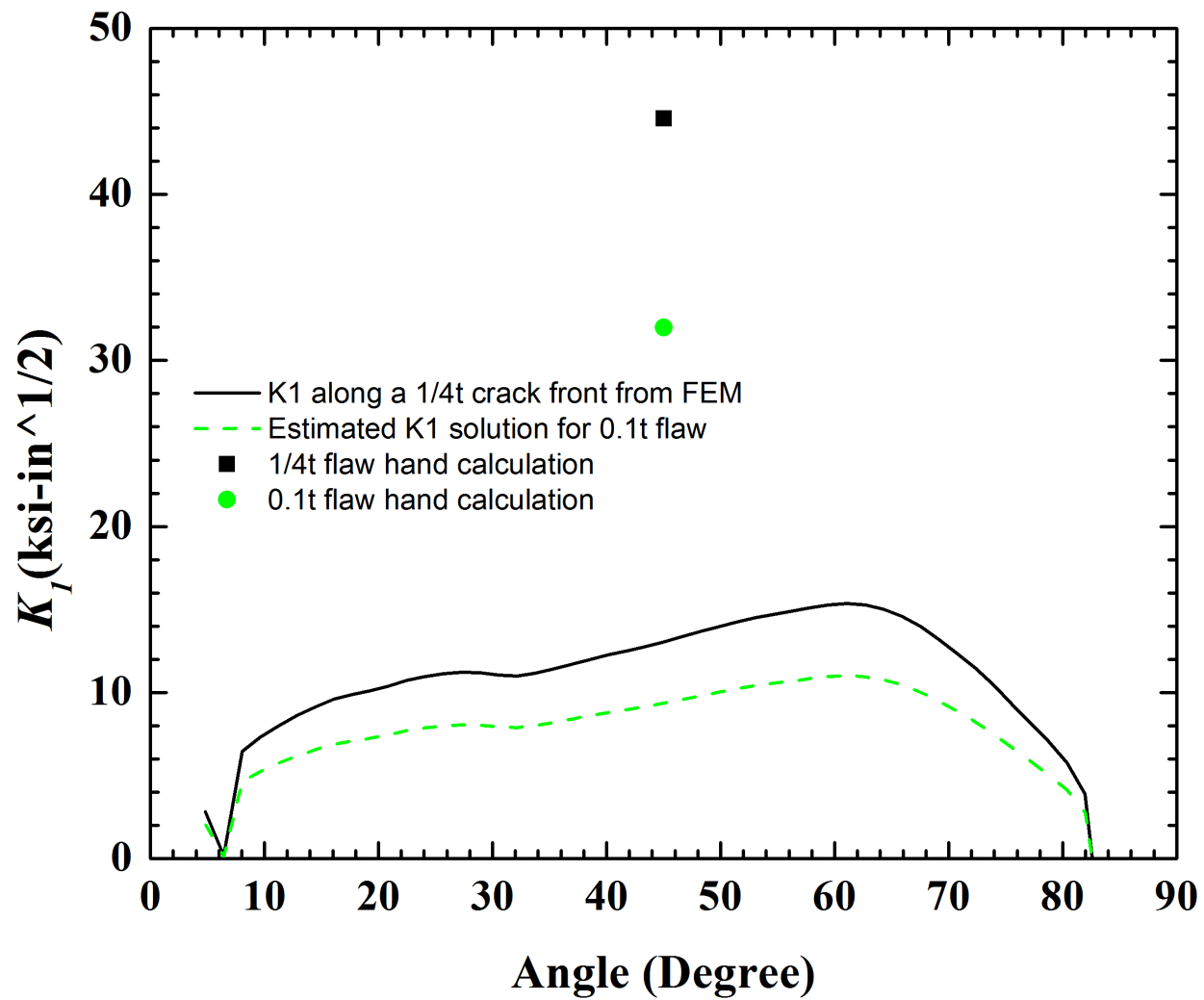


Figure 48. Stress Intensity Factor (K_I) Along the Crack Front of the BWR CS Nozzle for BWR Thermal Shock Loading at 30.4 Minutes

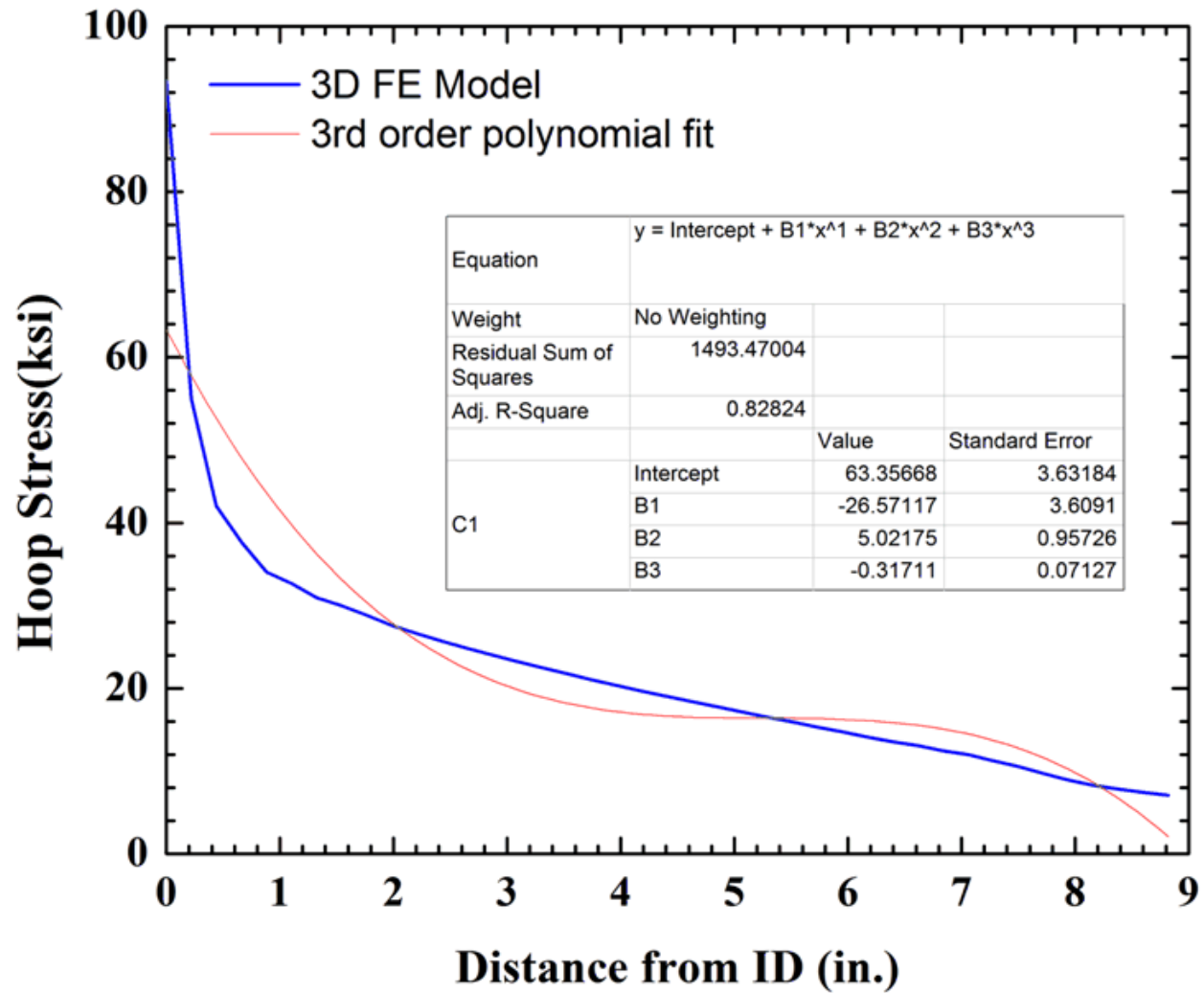


Figure 49. Hoop Stress Along the Selected Stress Path for the BWR CS Nozzle for a Pressurized BWR Thermal Shock Transient at 0.1 Minute

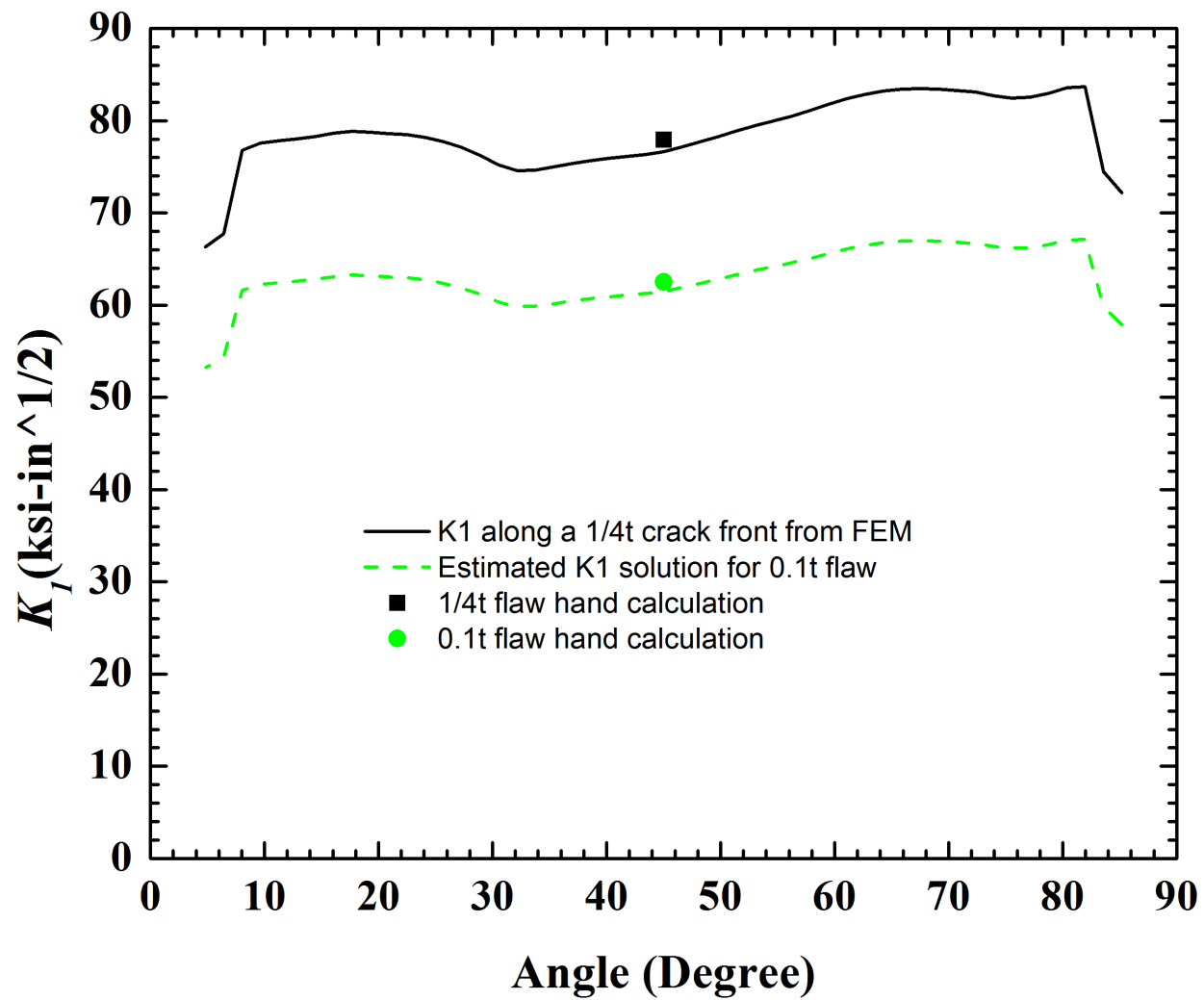


Figure 50. Stress Intensity Factor (K_I) Along the Crack Front of the BWR CS Nozzle for Pressurized BWR Thermal Shock Loading at 0.1 Minute

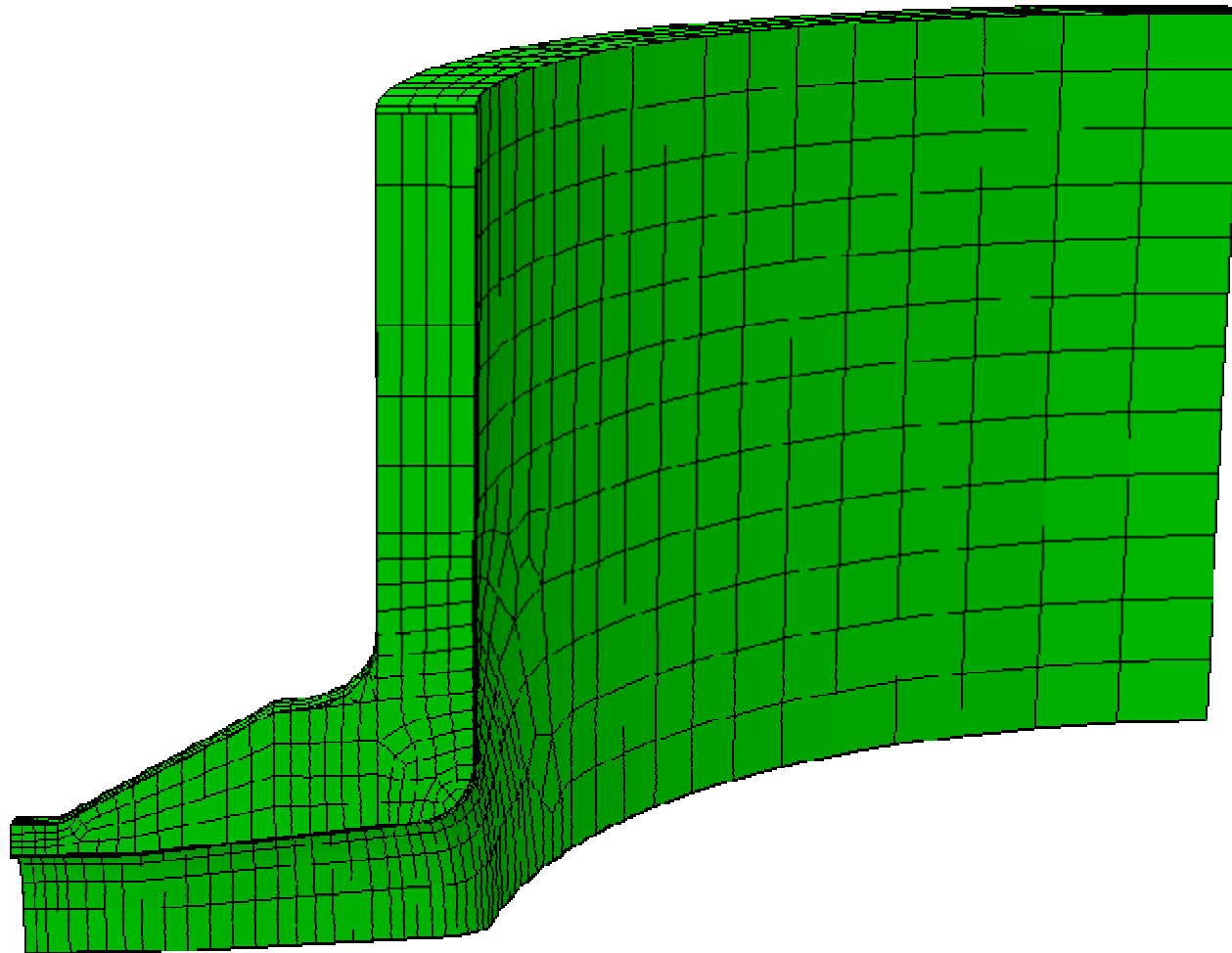


Figure 52. 3-D FEM for the Uncracked PWR Inlet Nozzle

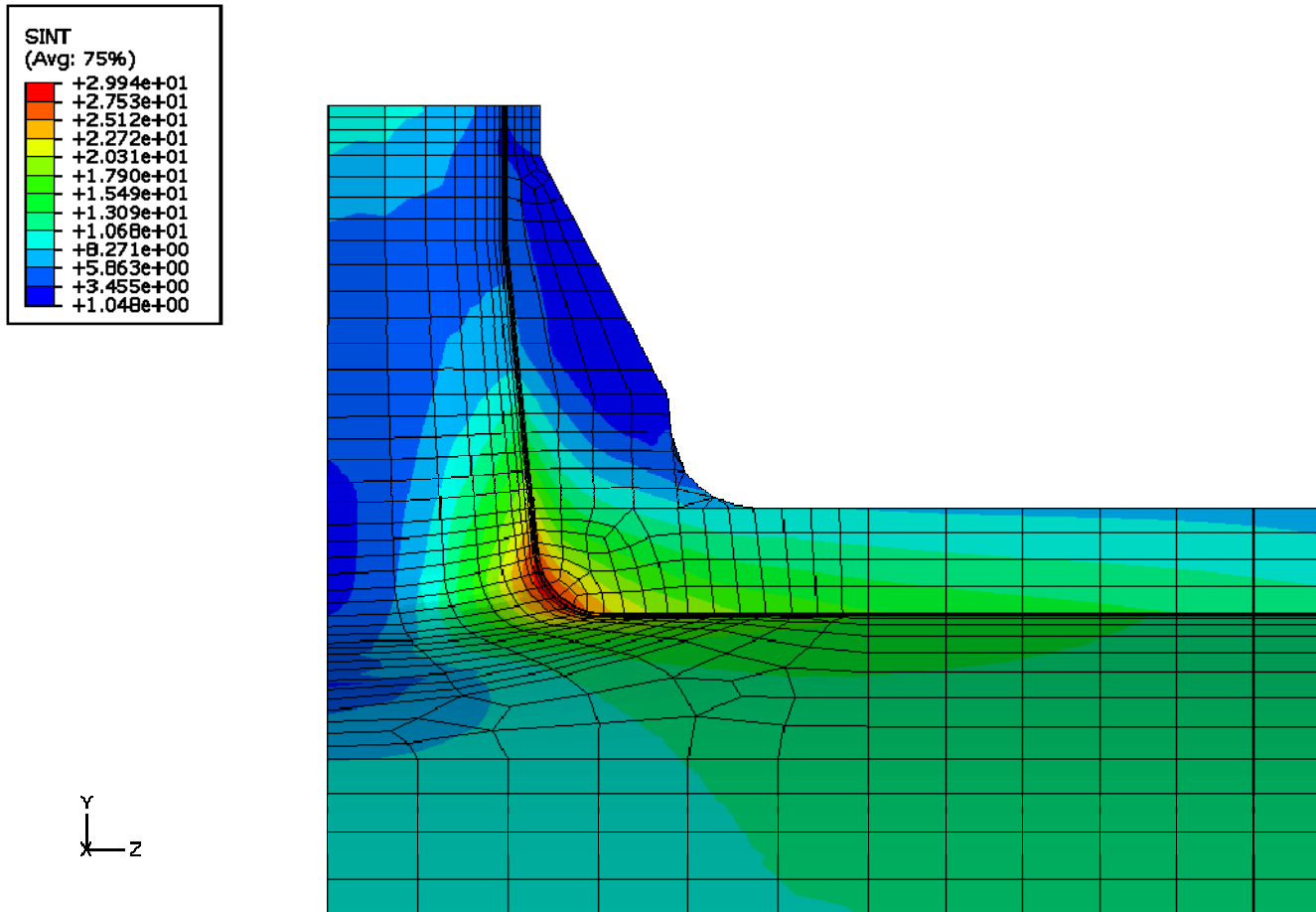


Figure 53. Stress Intensity (SINT) for the PWR Inlet Nozzle Subjected to 1,000 psi Internal Pressure

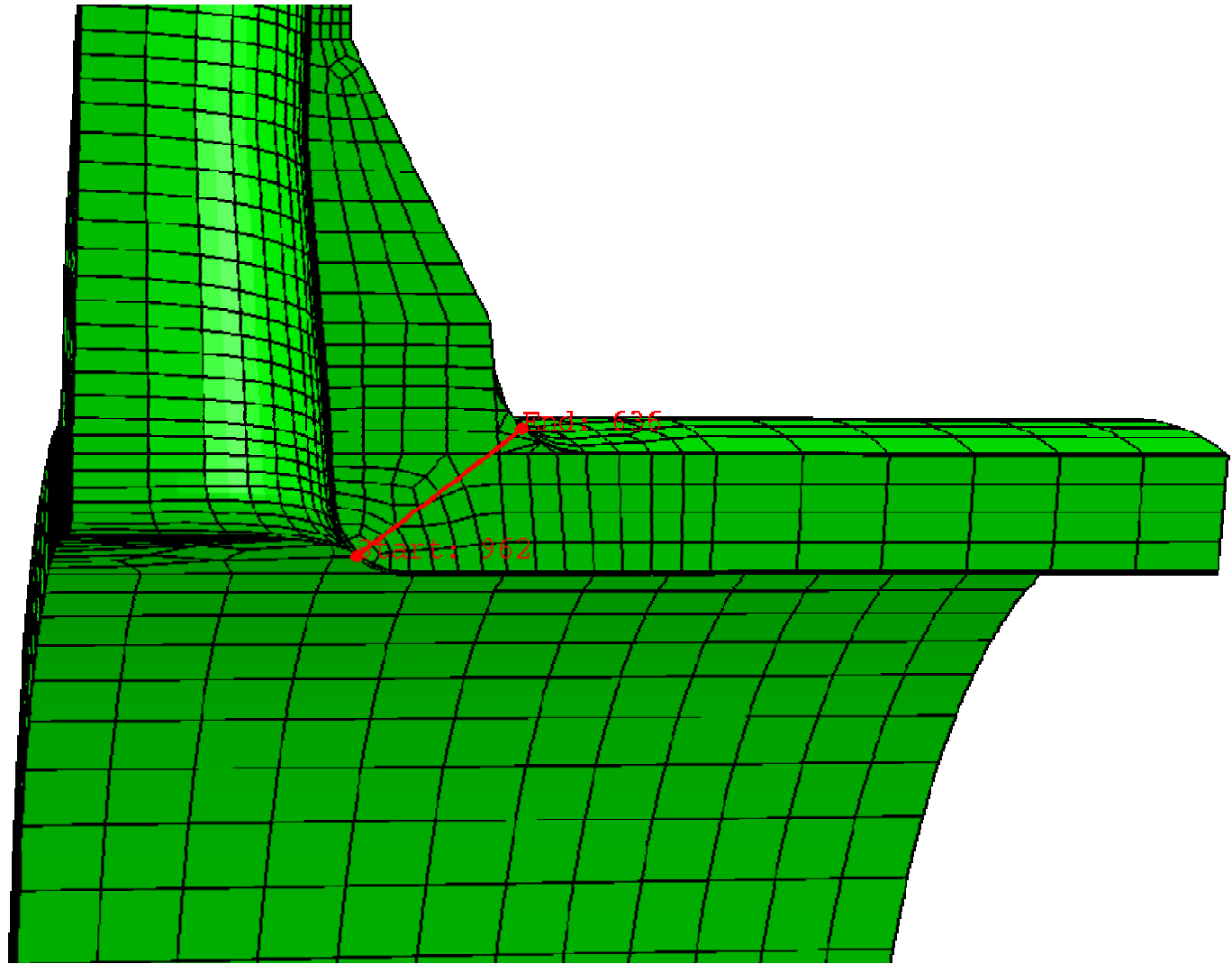


Figure 54. Hoop Stress Extraction Path Selected for the PWR Inlet Nozzle

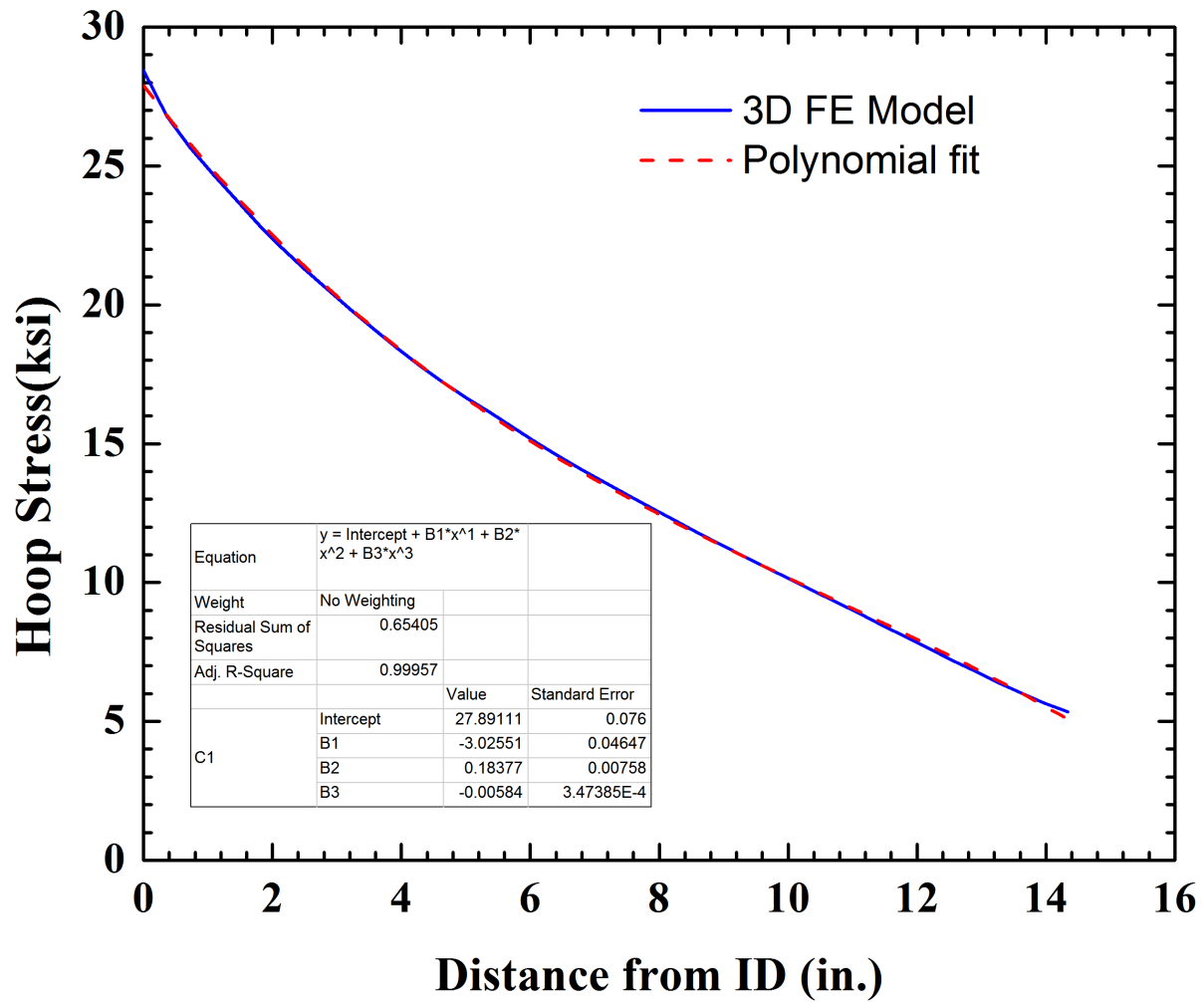


Figure 55. Hoop Stress Along the Nozzle Corner Stress Path for the PWR Inlet Nozzle for 1,000 psi Internal Pressure

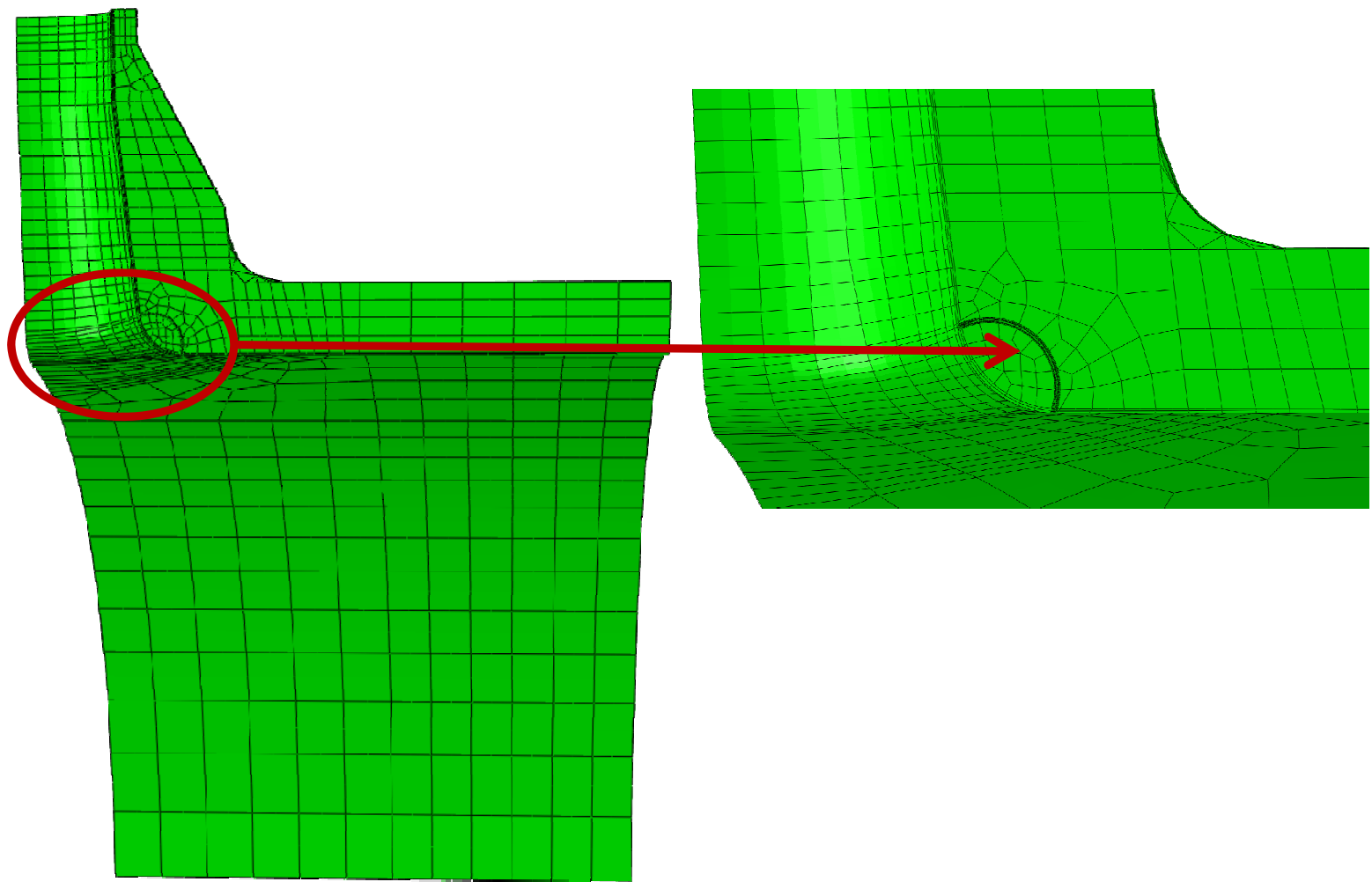


Figure 56. 3-D FEM for the PWR Inlet Nozzle with a Postulated $\frac{1}{4}$ t Circular Corner Crack

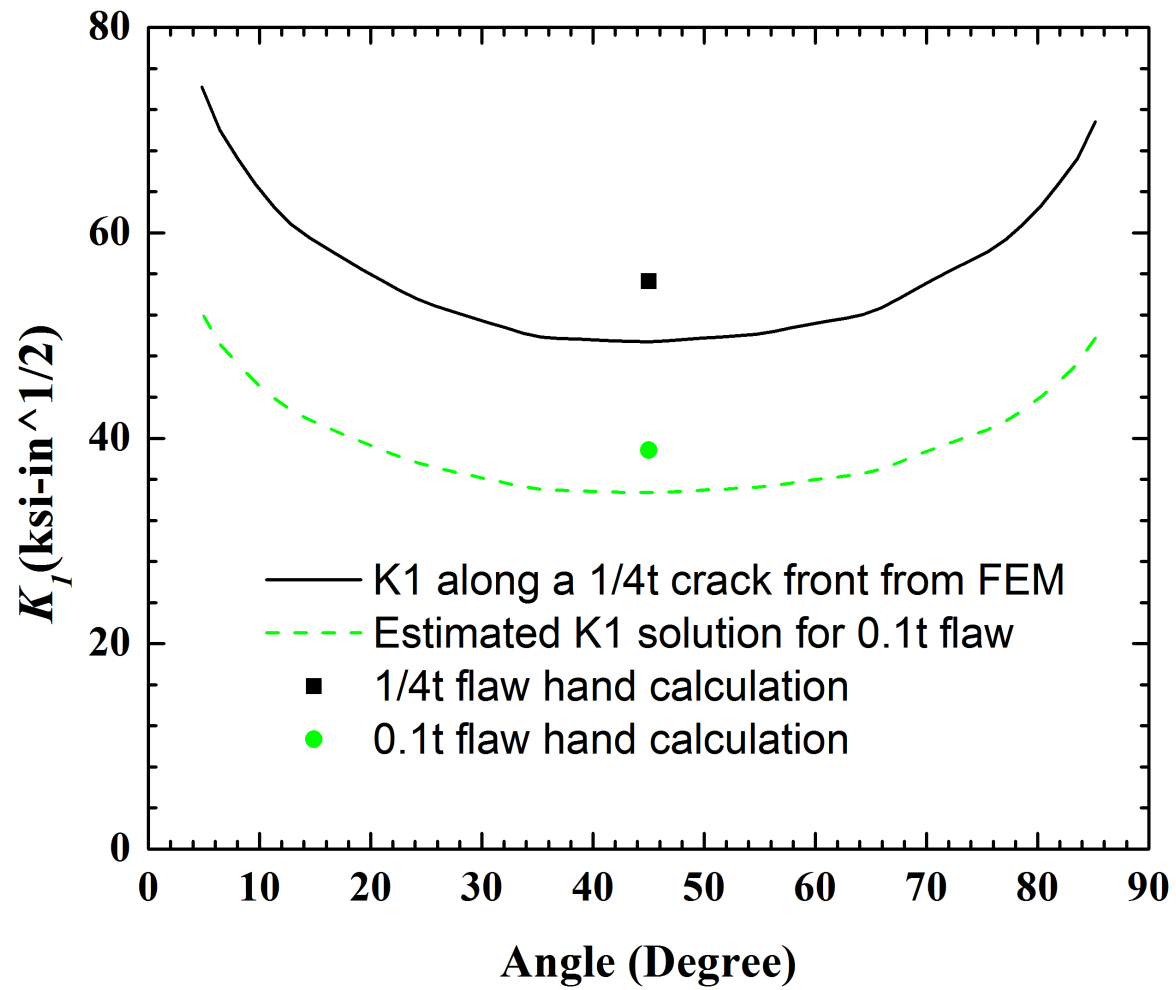


Figure 57. Stress Intensity Factor (K_I) Along the Crack Front for 1,000 psig Pressure Loading for the PWR Inlet Nozzle

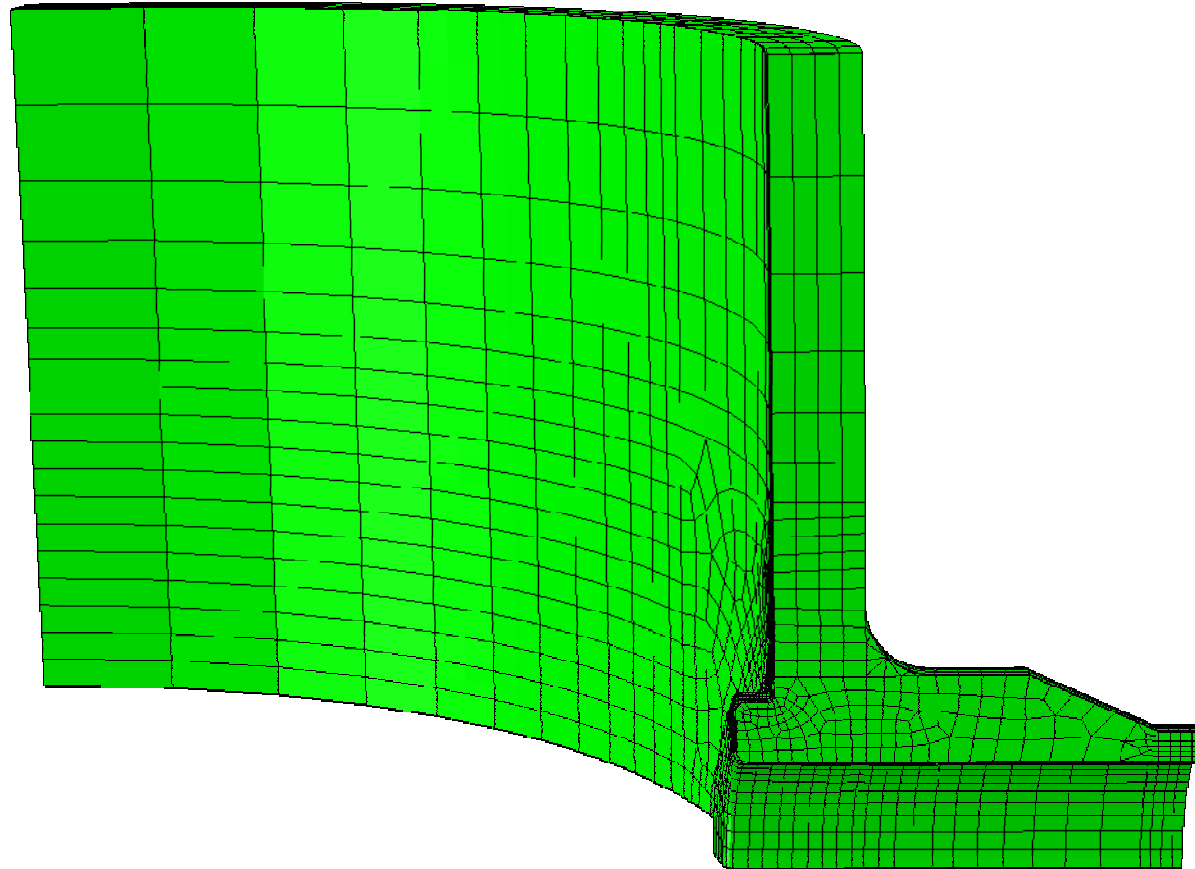


Figure 59. 3-D FEM for the Uncracked PWR Outlet Nozzle

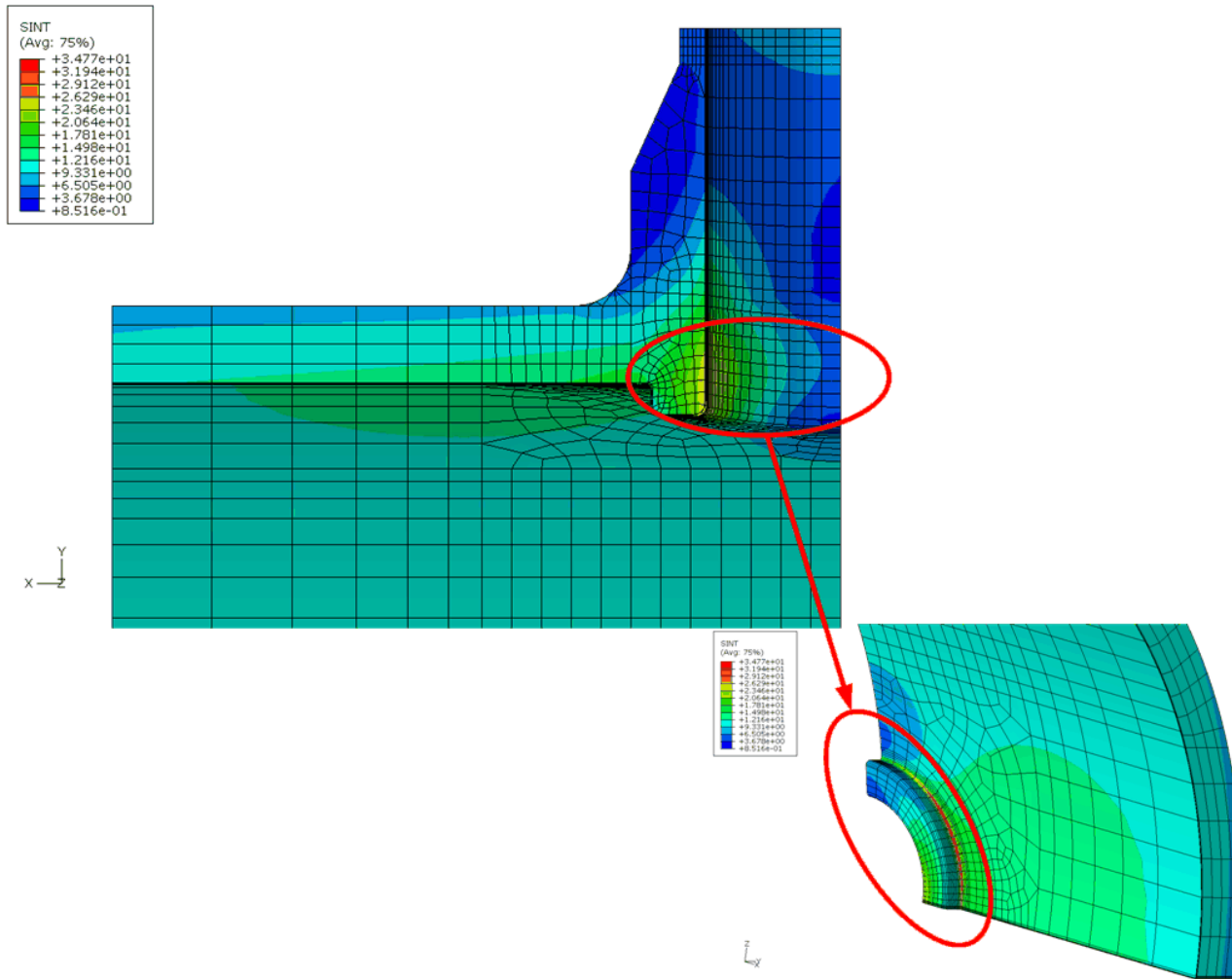


Figure 60. Stress Intensity (SINT) for the PWR Outlet Nozzle Subjected to 1,000 psi Internal Pressure

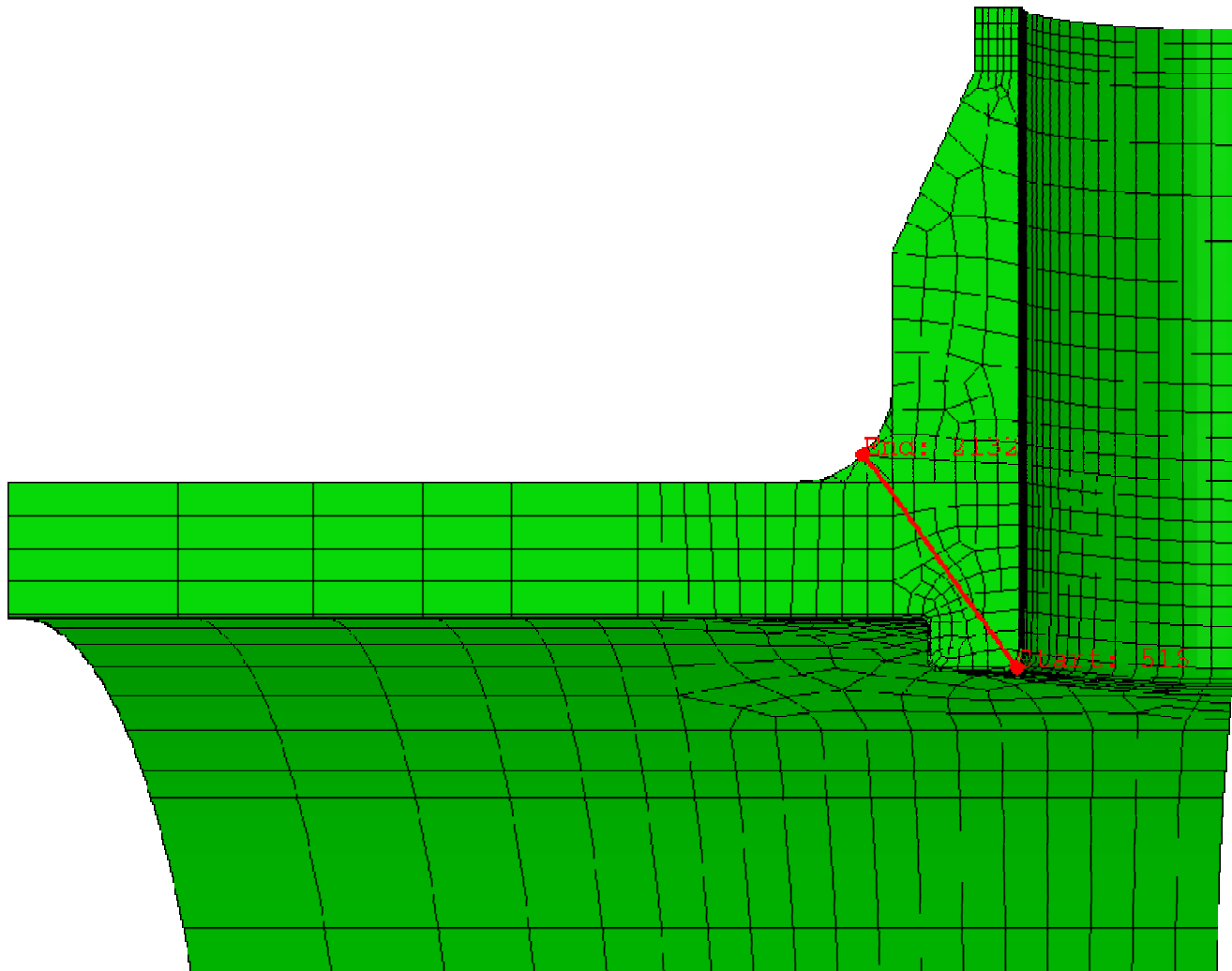


Figure 61. Hoop Stress Extraction Path for the PWR Outlet Nozzle

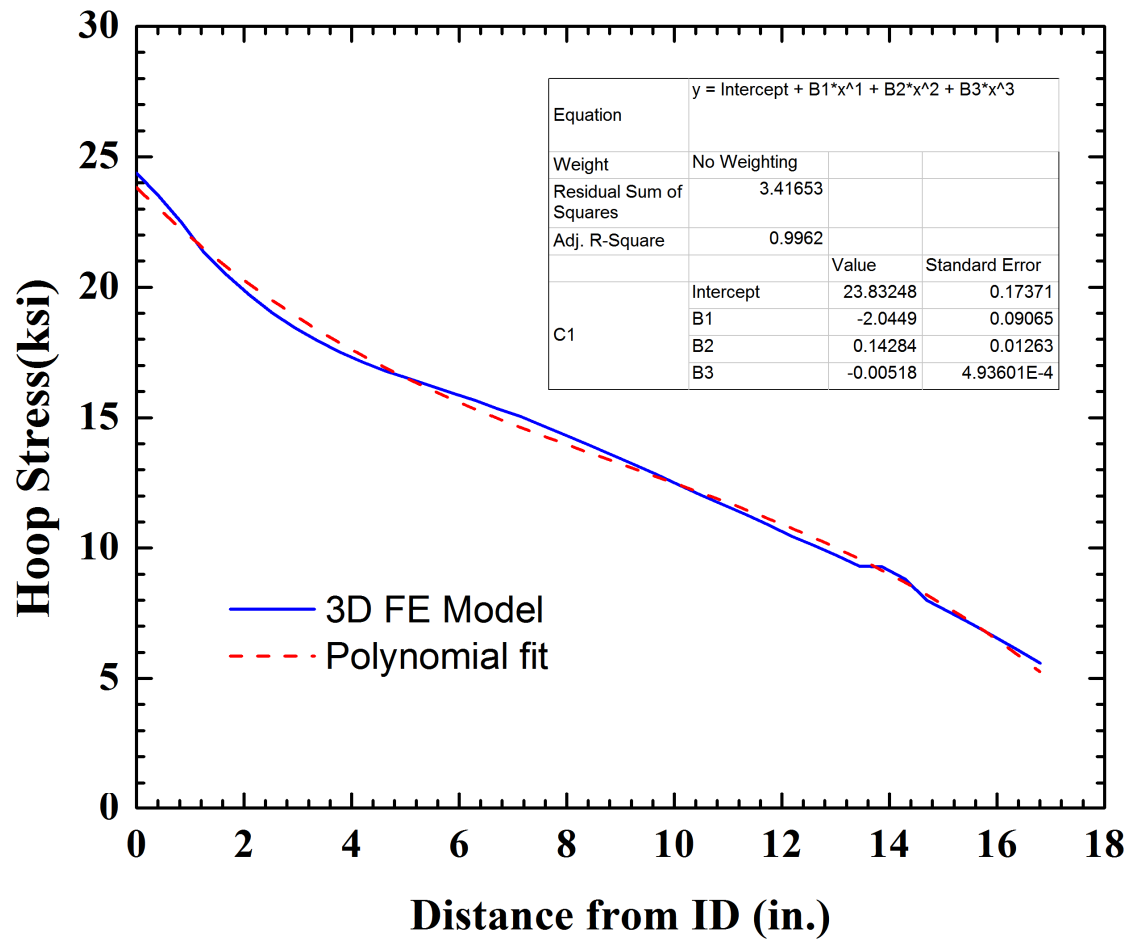


Figure 62. Hoop Stress Along the PWR Outlet Nozzle Corner Path for 1,000 psi Internal Pressure

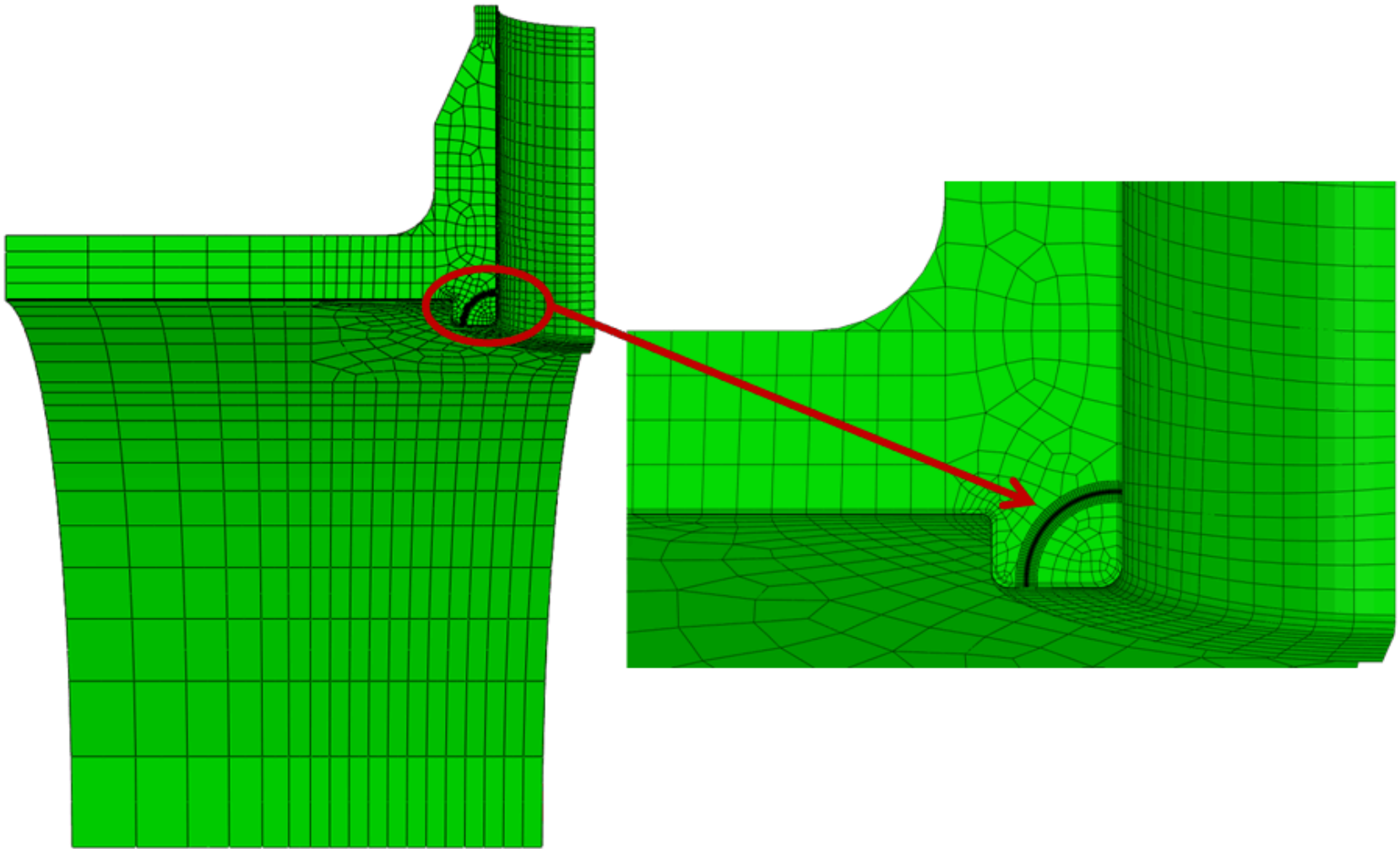


Figure 63. 3-D FEM for the PWR Outlet Nozzle with a Postulated $\frac{1}{4}t$ Circular Corner Crack

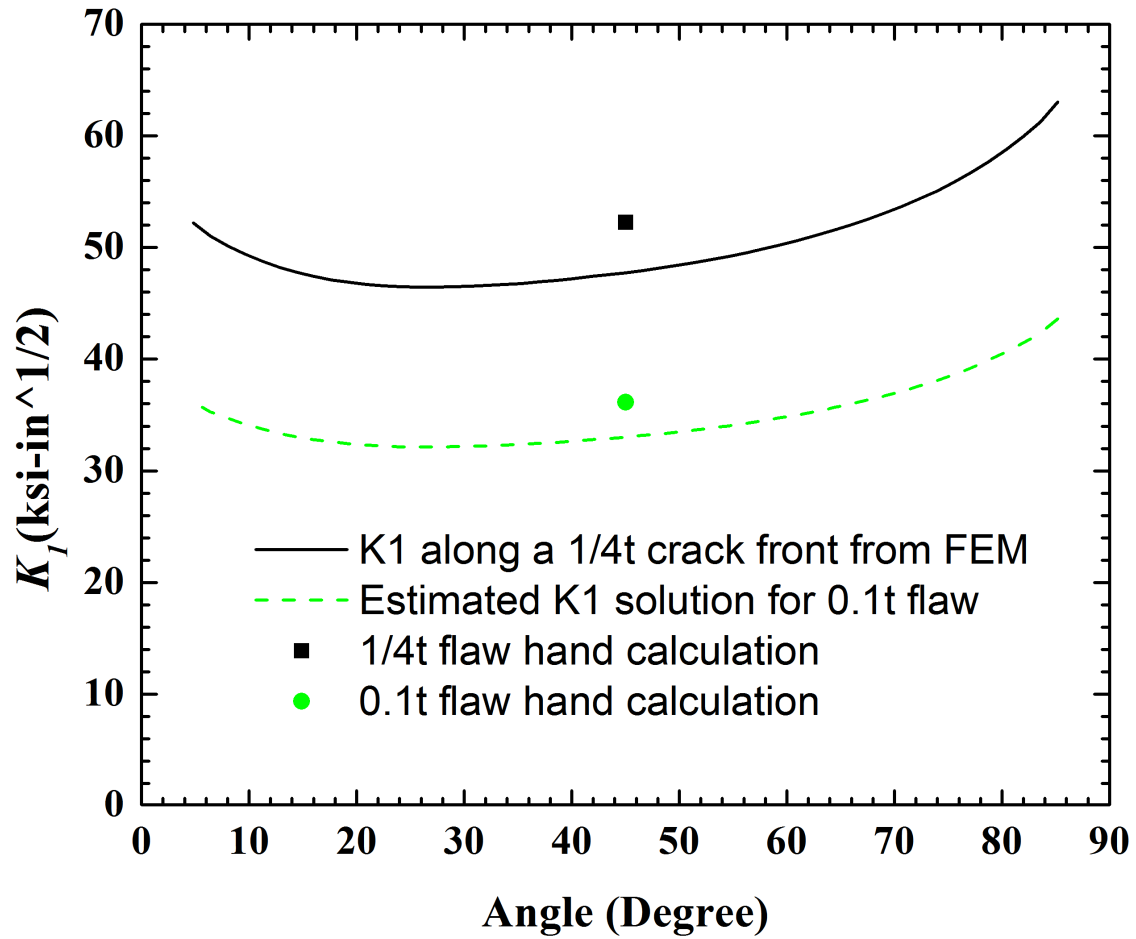


Figure 64. Stress Intensity Factor (K_I) Along the Crack Front for 1,000 psig Pressure Loading for the PWR Outlet Nozzle

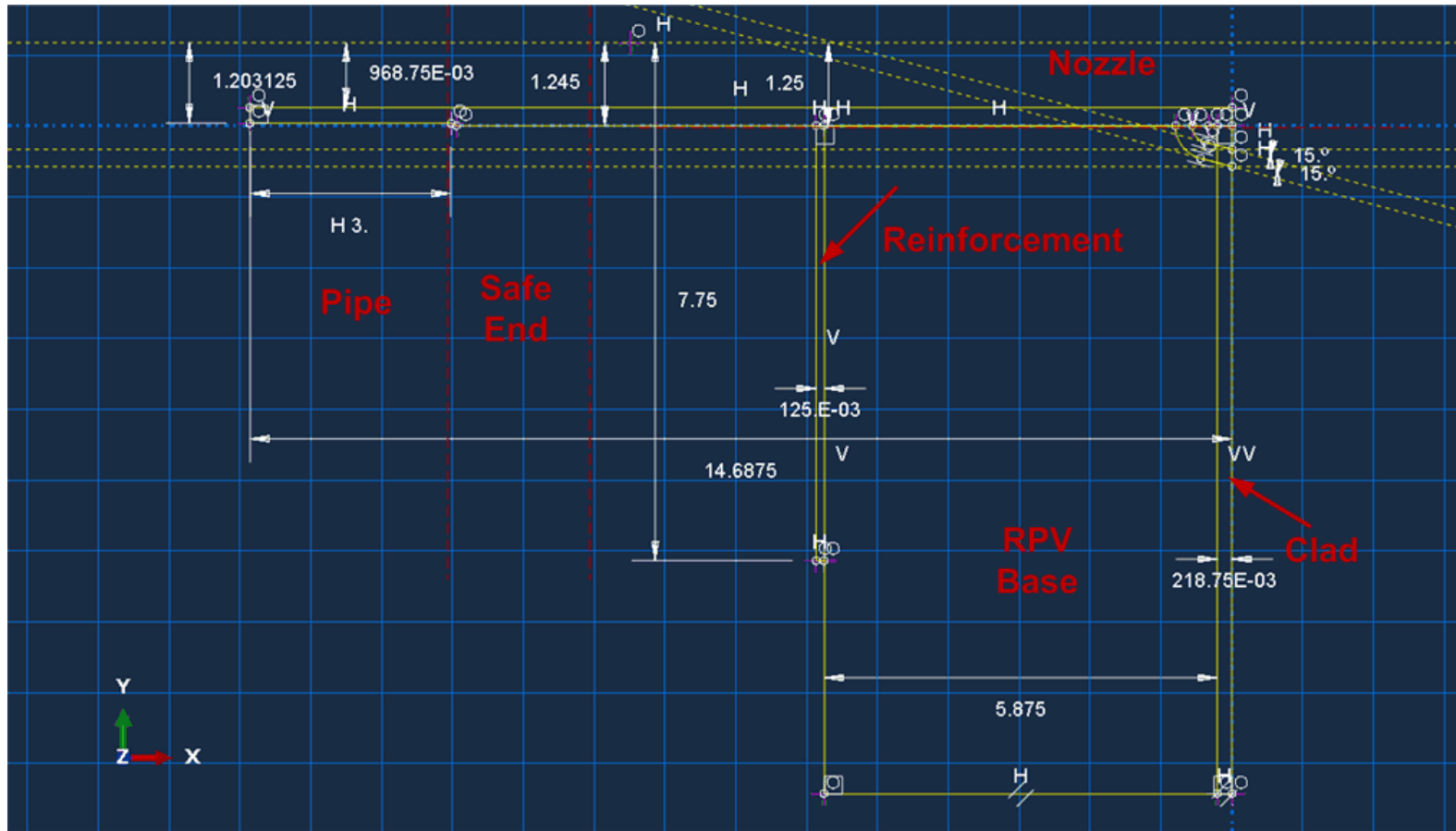


Figure 65. Geometry for the BWR Instrument Nozzle (from Reference [14])

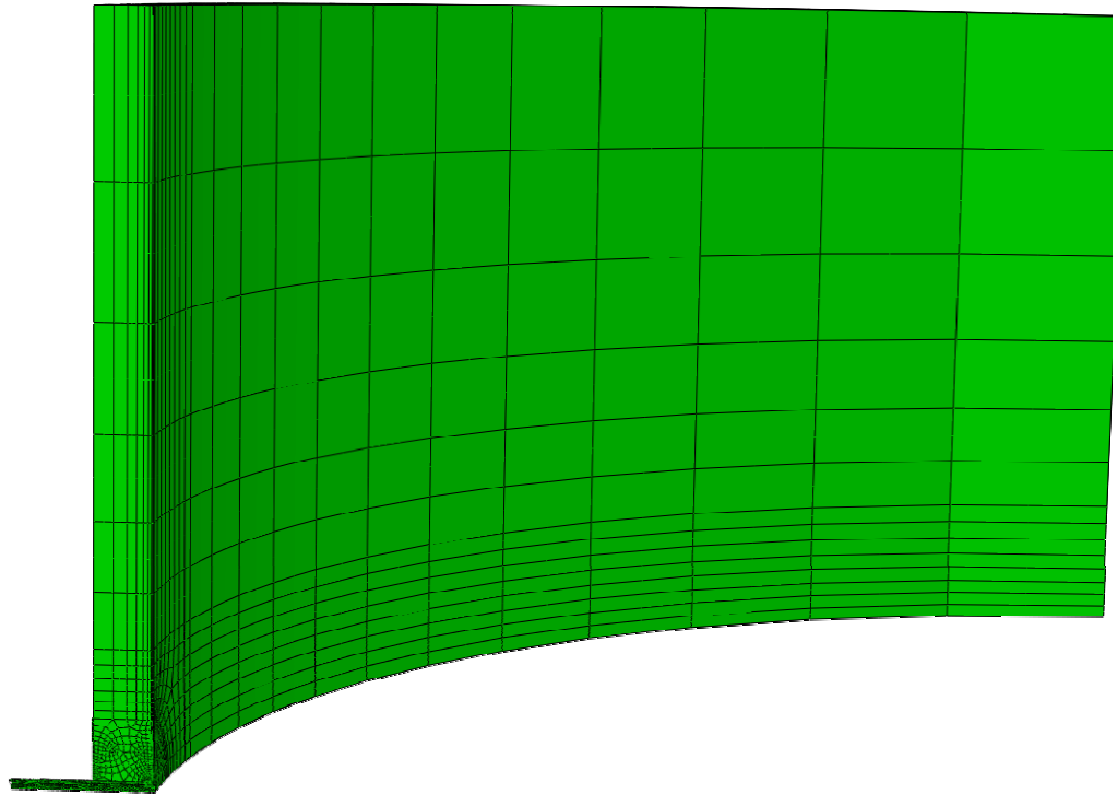


Figure 66. 3-D FEM for the Uncracked BWR Instrument Nozzle

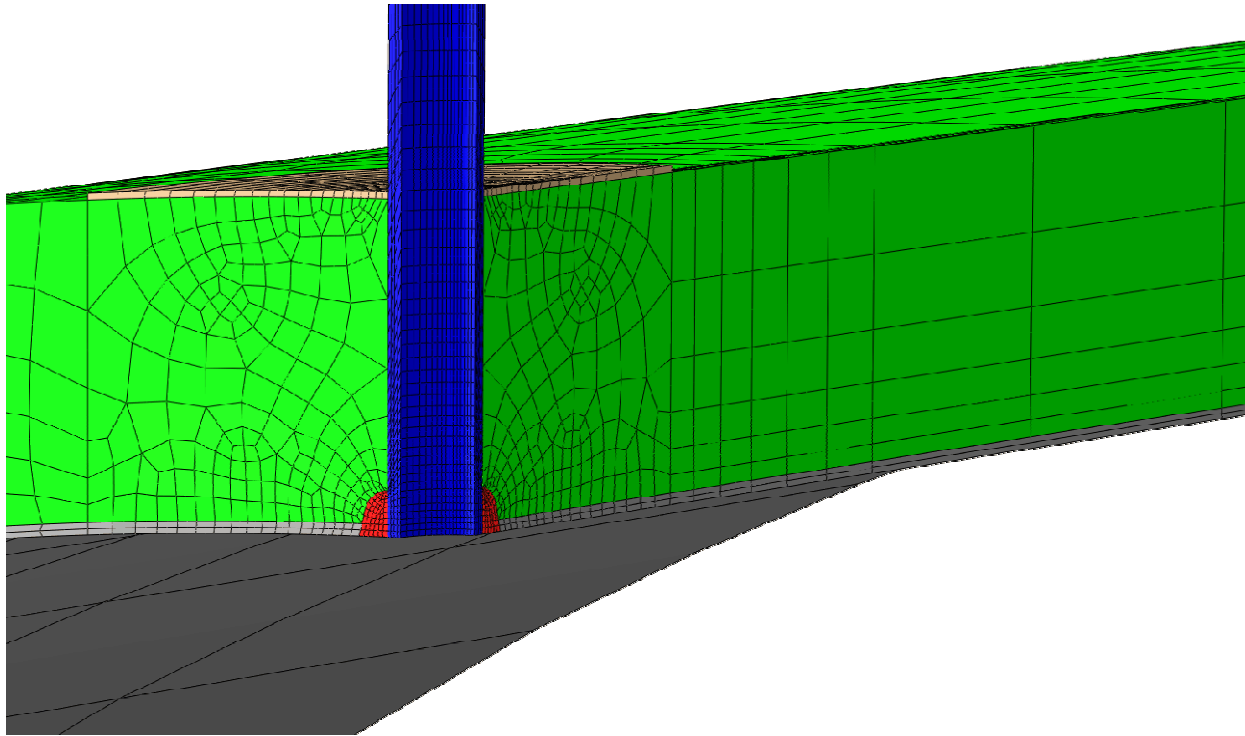


Figure 67. Close-up View of 3-D FEM for the Uncracked BWR Instrument Nozzle

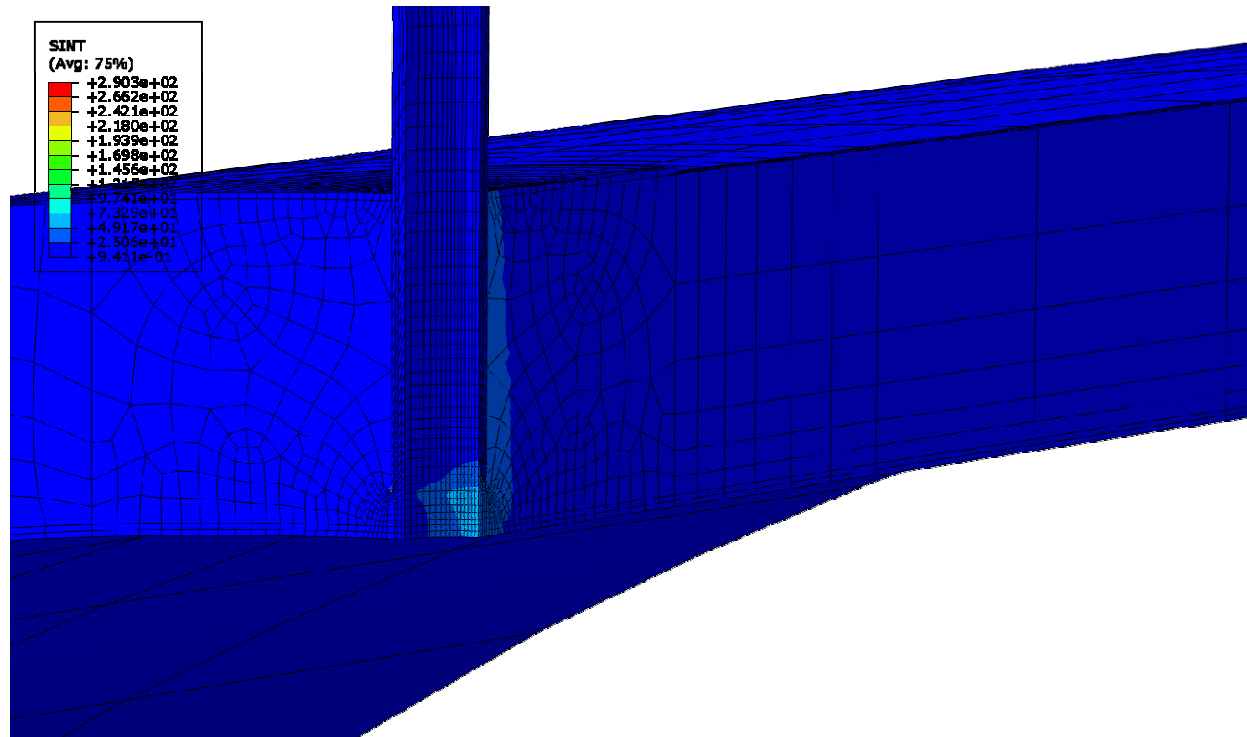


Figure 68. Stress Intensity (SINT) for the BWR Instrument Nozzle Subjected to 1,000 psi Internal Pressure

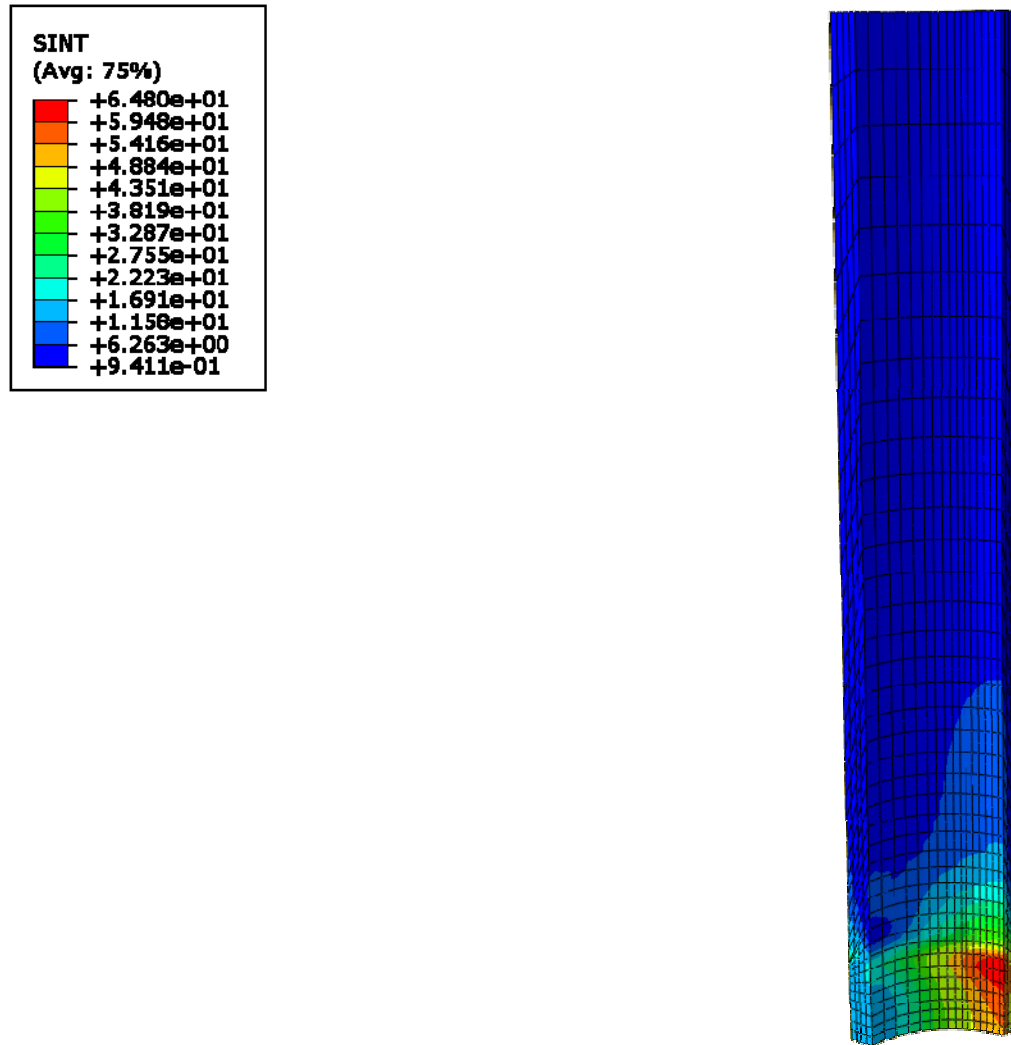


Figure 69. Stress Intensity (SINT) for the BWR Instrument Nozzle (Nozzle Insert Portion Only)

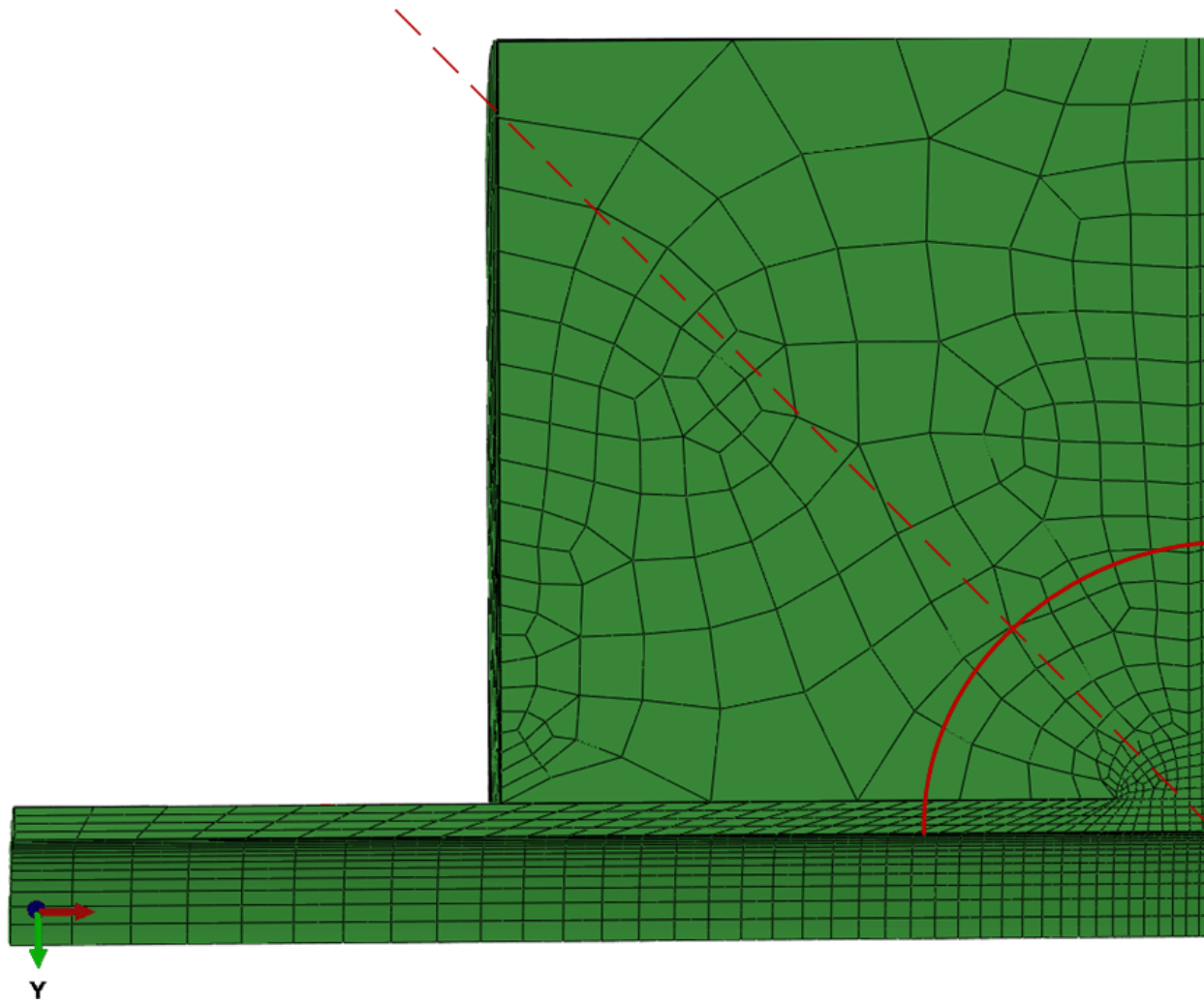


Figure 70. Hoop Stress Extraction Path and 1/4t Crack Definition for the BWR Instrument Nozzle

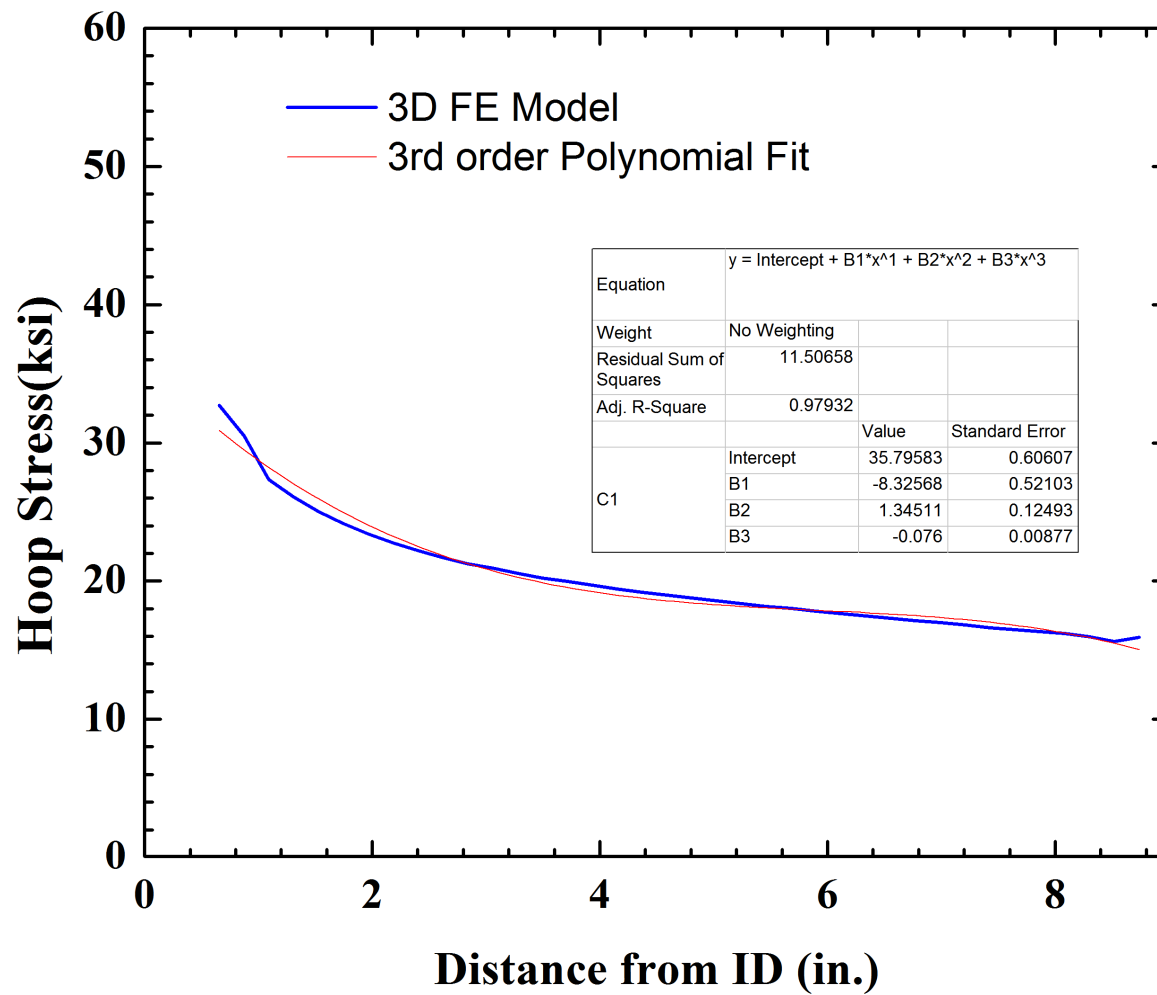


Figure 71. Hoop Stress Along the BWR Instrument Nozzle Corner Path for 1,000 psi Internal Pressure Loading

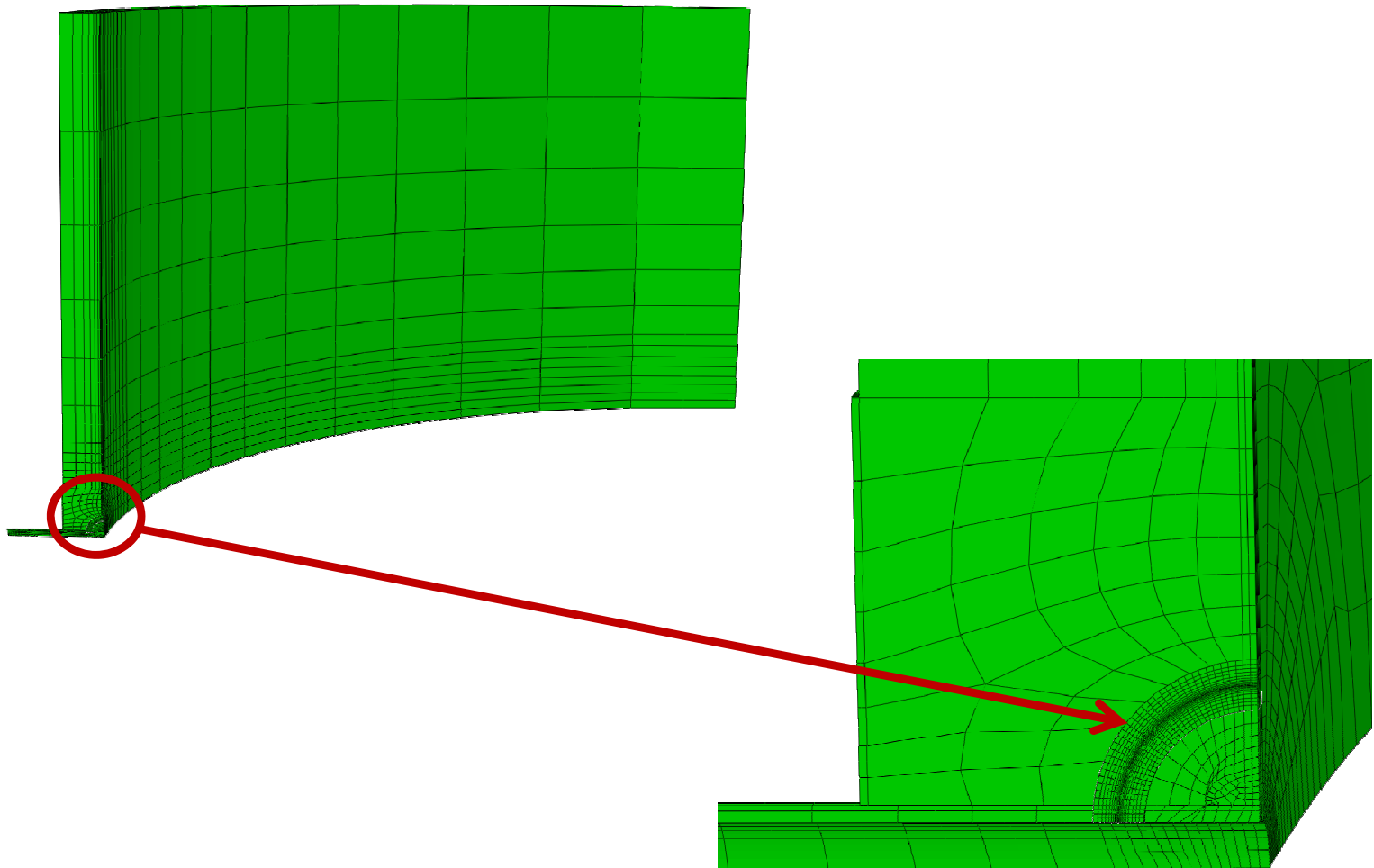


Figure 72. 3-D FEM for the BWR Instrument Nozzle with a Postulated $\frac{1}{4}t$ Circular Corner Crack

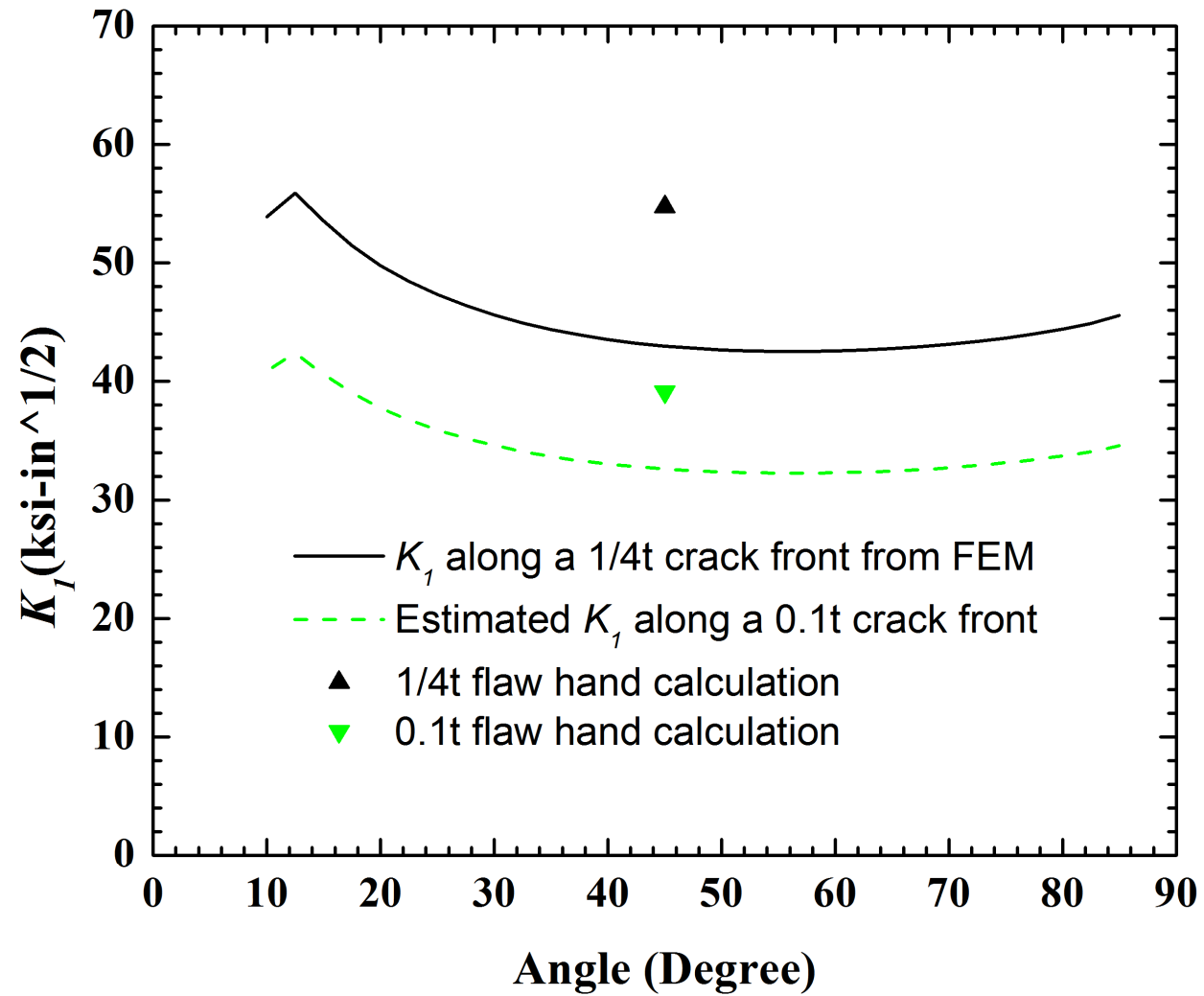


Figure 73. Stress Intensity Factor (K_I) Along the Crack Front Under 1,000 psig Pressure Loading for the BWR Instrument Nozzle

9. References

1. ASME Boiler & Pressure Vessel Code, Section XI, Nonmandatory Appendix G, “Fracture Toughness Criteria for Protection Against Failure,” 2008 Addenda.
2. WRC Bulletin 175, “PVRC Recommendations on Toughness Requirements for Ferritic Materials,” Welding Research Council, New York, August 1972.
3. H. S. Mehta, T. J. Griesbach, and G. L. Stevens, “Suggested Improvement to Appendix G of ASME Section XI Code,” Proceedings of 2008 ASME Pressure Vessels and Piping Conference, PVP2008-61624, July 27-31, 2008, Chicago, IL, USA.
4. Code of Federal Regulations, Title 10, Energy, Part 50, “Domestic Licensing of Production and Utilization Facilities,” Appendix G, “Fracture Toughness Requirements.”
5. S. A. Delvin and P. C. Riccardella, “Fracture Mechanics Analysis of JAERI Model Pressure Vessel Test,” ASME Paper No. 78-PVP-91, Proceedings of the 1978 ASME Pressure Vessels and Piping Conference, June 25-30, 1978, Montreal, Quebec, Canada.
6. Vermont Yankee Confirmatory Environmentally Assisted Fatigue (CUF_{en}) Analyses of Reactor Pressure Vessel Core Spray and Recirculation Outlet Nozzles, NRC ADAMS Accession No. ML090840422.
7. M. C. Walter and D. V. Sommerville, “Nozzle Blend Radius Peak Stress Correction Factors for 2-D Axisymmetric Finite Element Models,” Proceedings of 2010 ASME Pressure Vessels and Piping Conference, PVP2010-25104, July 18-22, 2010, Bellevue, WA, USA.
8. ABAQUS Finite Element Software, Version 6.9, Dassault Systems Simulia Corp., 2009.
9. ANSYS, Release 8.1 (w/Service Pack 1), ANSYS, Inc., June 2004.
10. ASME Boiler & Pressure Vessel Code, Section III, Rules for Construction of Nuclear Facility Components, Division 1 - Subsection NB, “Class 1 Components,” 2008 Addenda.
11. ASME Boiler & Pressure Vessel Code, Section II, Materials, Part D, “Properties (Customary),” 1998 Edition, with Addenda through year 2000.
12. Structural Integrity Associates Calculation No. VY-16Q-308, Revision 0, “Core Spray Nozzle Finite Element Model,” 7/19/2007, NRC ADAMS Accession No. ML082490570.

13. PVRUF Combustion Engineering Drawings (NRC ADAMS Accession No. ML102730694), including:

- a. CE Drawing No. 12573-171-004, Revision 0, "General Arrangement, Elevation."
- b. CE Drawing No. 12573-121-001, Revision 0, "Upper Vessel Assembly."
- c. CE Drawing No. 12573-121-002, Revision 0, "Upper Vessel Machining."
- d. CE Drawing No. 12573-121-003, Revision 0, "Upper Vessel Machining."
- e. CE Drawing No. 12573-128-001, Revision 0, "Inlet Nozzle."
- f. CE Drawing No. 12573-128-002, Revision 0, "Inlet Nozzle Cladding and Machining."
- g. CE Drawing No. 12573-128-003, Revision 0, "Outlet Nozzle."
- h. CE Drawing No. 12573-128-004, Revision 0, "Outlet Nozzle Cladding and Machining."
- i. CE Drawing No. C-STD11-131-031-0, Revision 01, "Nozzle Safe Ends."

14. Attachment 10 to JAFP-08-0067, Structural Integrity Associates Calculation No. 0800846.301, Revision 0, "2" Instrument Nozzle Stress Analysis," 7/16/2008, NRC ADAMS Accession No. ML082100460.

This page is intentionally left blank.

NRC FORM 335 (2-89) NRCM 1102, 3201,3202	U.S. NUCLEAR REGULATORY COMMISSION BIBLIOGRAPHIC DATA SHEET <i>(See instructions on the reverse)</i>	1. REPORT NUMBER (Assigned by NRC, Add Vol., Supp., Rev., and Addendum Numbers, if anv. 1) ORNL/TM-2010/246			
2. TITLE AND SUBTITLE Stress and Fracture Mechanics Analyses of Boiling Water Reactor and Pressurized Water Reactor Pressure Vessel Nozzles – Revision 1	3. DATE REPORT PUBLISHED <table border="1" style="width: 100%; border-collapse: collapse;"> <tr> <td style="width: 50%;">MONTH</td> <td style="width: 50%;">YEAR</td> </tr> <tr> <td style="text-align: center;">June</td> <td style="text-align: center;">2012</td> </tr> </table>	MONTH	YEAR	June	2012
	MONTH	YEAR			
	June	2012			
4. FIN OR GRANT NUMBER N6438					
5. AUTHOR(S) S. Yin, B. R. Bass, and G. L. Stevens	6. TYPE OF REPORT Final, technical				
	7. PERIOD COVERED <i>(Inclusive Dates)</i>				
8. PERFORMING ORGANIZATION - NAME AND ADDRESS <i>(If NRC, provide Division, Office or Region, U.S. Nuclear Regulatory Commission, and mailing address; if contractor, provide name and mailing address.)</i> Probabilistic Pressure Boundary Integrity Safety Assessment (PISA) Program Oak Ridge National Laboratory P. O. Box 2008, Mail Stop 6085 Oak Ridge, TN 37831-6085					
9. SPONSORING ORGANIZATION - NAME AND ADDRESS <i>(If NRC, type "Same as above"; if contractor, provide NRC Division, Office or Region, U.S. Nuclear Regulatory Commission, and mailing address.)</i> Division of Engineering Office of Nuclear Regulatory Research U. S. Nuclear Regulatory Commission Washington, DC 2055-0001					
10. SUPPLEMENTARY NOTES					
11. ABSTRACT <i>(200 words or less)</i> This report describes stress and fracture mechanics analyses performed to assess boiling water reactor (BWR) and pressurized water reactor (PWR) nozzles located in the reactor pressure vessel (RPV) adjacent to the core beltline region. Various RPV nozzle geometries were identified by the NRC staff for evaluation. The purpose of the analyses performed on five nozzle configurations was as follows: <ul style="list-style-type: none"> • To model and understand differences in pressure and thermal stress results using a two-dimensional (2-D) axisymmetric finite element model (FEM) vs. a three-dimensional (3-D) FEM for all nozzle types. In particular, the ovalization (stress concentration) effect of two intersecting cylinders was investigated; • To verify the accuracy of linear elastic fracture mechanics (LEFM) closed-form solutions for stress intensity factor for a postulated nozzle corner crack for both thermal and pressure loading for all nozzle configurations; • To assess the significance of attached piping loads on the stresses in the nozzle corner region; • To assess the significance of applying pressure on the crack face with respect to the stress intensity factor for a postulated nozzle corner crack. This work was performed to support potential revision and refinement of Title 10 to the U.S. Code of Federal Regulations (CFR), Part 50, Appendix G, "Fracture Toughness Requirements."					
12. KEY WORDS/DESCRIPTORS <i>(List words or phrases that will assist researchers in locating the report.)</i> reactor pressure vessel nozzles, fracture mechanics, Stress Intensity Factor, Magnification Factor Method	13. AVAILABILITY STATEMENT unlimited				
	14. SECURITY CLASSIFICATION <i>(This Page)</i> unclassified				
	<i>(This Report)</i> unclassified				
	15. NUMBER OF PAGES				
16. PRICE					